Nanolithography on Mercury Telluride

Dissertation

zur Erlangung
des naturwissenschaftlichen Doktorgrades
der Julius-Maximilians-Universität Würzburg

vorgelegt von
Mathias Josef Mühlbauer
aus Deggendorf

Würzburg, 2015

Eingereicht am: ____________________
bei der Fakultät für Physik und Astronomie

1. Gutachter: Prof. Dr. Hartmut Buhmann
2. Gutachter: Prof. Dr. Matthias Bode
3. Gutachter: ____________________
der Dissertation

Vorsitzende(r): ____________________

1. Prüfer: Prof. Dr. Hartmut Buhmann
2. Prüfer: Prof. Dr. Matthias Bode
3. Prüfer: ____________________
im Promotionskolloquium

Tag des Promotionskolloquiums: ____________________

Doktorurkunde ausgehändigt am: ____________________

Contents

1. Introduction **1**

2. A new class of materials: Topological insulators **3**

2.1. Introduction . . . 3
2.2. Classification of topological insulators . . . 3
2.3. HgTe/HgCdTe quantum wells: A 2D-topological insulator . . . 5
2.4. Remarkable experiments on HgTe QWs . . . 9
2.5. Summary . . . 16

3. Quantum point contacts in HgTe/HgCdTe heterostructures **17**

3.1. Motivation . . . 17
3.2. QPCs in a nutshell . . . 18
3.2.1. Conductance quantization . . . 19
3.2.2. Electron beam collimation . . . 23
3.3. Realization of QPCs in HgTe quantum well structures . . . 27
3.3.1. Concept . . . 27
3.3.2. Conductance measurements . . . 30
3.3.3. Collimation measurements . . . 35
3.4. Spin polarizer . . . 44

4. Lithographical developments **59**

4.1. Ohmic contacts, bonding and miniaturization . . . 59
4.2. Reduction of sidewalls and fencing for HgTe heterostructures . . . 78
4.2.1. Sidewalls . . . 78
4.2.2. Critical dimensions and fencing . . . 81
4.2.3. Hardmask lithography . . . 85
4.2.4. Combining hardmasks and wet etching . . . 94

4.3. Low energy e-beam lithography 96
4.4. Airbridges 100

5. Weak antilocalization 111
5.1. Introduction 111
5.2. Experiment 114
5.3. Model 120
5.4. Discussion 122

6. Summary 125

7. Zusammenfassung 127

A. List of substrates 129

B. Acronyms 131

C. Publications 133

Bibliography 149

1. Introduction

More than 65 years have passed since the realization of the first germanium based semiconductor point contact transistor by William Shockley, John Bardeen and Walter Brattain [1]. This invention and the potential behind it sparked a gigantic research effort in solid state electronics and was eventually awarded with the Nobel Prize in 1956. Two years earlier the first silicon based transistors had become available through major technical advances by Gordon K. Teal at the research labs at Texas Instruments Inc. [2], long before the scientific community was even expecting their first realization [3]. The birth of the "Silicon Age". As applications for transistors were gaining more and more complexity and the limits of circuit construction were reached, this lead to the development of the integrated circuit (IC) in 1958 by Jack Kilby, another invention awarded with the Nobel Prize in the year 2000.
Since then lithography has been helping to make ICs smaller, faster, more reliable and not to forget affordable. A state of the art 15-core Xeon® processor from Intel crams a breathtaking 4.31 billion transistors on a chip area approximately the square of an inch [4]. For many years continuous improvements in lithography, circuit design and process innovations have improved the cost per function of ICs by 30% per year [5]. The impact of the advances in IC production on our daily life is ubiquitous, not only because personal computers, smart-phones and tablets have become our daily companions. Lithography is no longer confined to the production of ICs but has lead to the development of completely new research fields and industrial branches like micro-electromechanical systems (MEMS). These devices are used e.g. in sensors and actuators that can be found in automobiles, printers or clinical equipment [6], just to name a few applications. Classical lithography techniques are extended to completely new materials, requiring the development of entirely new fabrication processes to succeed.
While the evolution of lithography and continuous miniaturization helped to keep Moores law alive, the silicon era will come eventually to an end and new material com-

binations with entirely new concepts will come to its inheritance. Alternative transistor proposals have been around for more then two decades. A prominent example is the spin transistor (Spin-FET), as described by Supriyo Datta and Biswajit Das in 1990 [7]. Instead of charge this concept utilizes the electron spin for information processing. The spin manipulation is realized through the gate control of the Rashba spin-orbit (SO) interaction. However, a fundamental requirement for a successful realization of such a device is the formation of spin-polarized currents. A promising material combination for these experiments are HgTe quantum well (QW) structures. These QWs exhibit a strong controllable Rashba SO interaction [8] and quantum point contacts (QPCs) could be utilized to inject and detect spin polarized electrons.
HgTe heterostructures belong to a new class of materials called "topological insulators" (TIs) that have attracted a tremendous interest in the condensed matter physics community over the past few years. These materials exhibit time reversal symmetry protected surface states that originate from their special band structure and have their spin locked to their momentum [9]. Not only are these materials relevant for spintronic applications but they also offer the possibility to observe, create and manipulate Majorana bound states if combined with a s-wave superconductor [10]. Majorana fermions are quasi particles which could play a vital role for the realization of quantum computing, as they could be used to form stable quantum-bits [11]. Many of the proposed experiments rely on the interface quality between TIs and e.g. superconductors, require precision nano-structures and the exact control of the bulk carrier density. In order to create working prototype devices it is therefore essential to have a detailed understanding of how lithography affects the material properties and to adapt and develop the patterning techniques. Undoubtedly lithography will play an important role to pave the way from fascinating experiments on TIs to their possible applications in the future.
This work gives a brief overview on TI classification and HgTe QW structures as an example for a 2D-TI in Chapter 2. Chapter 3 is focused on QPCs and spin-optic experiments in HgTe high mobility two-dimensional electron gases (2DEG). Developments in nano-lithography on HgTe are presented in Chapter 4. In Chapter 5 we show measurements of the one dimensional weak antilocalization in HgTe nanowires, which also originates from the unique bandstructure of HgTe/HgCdTe heterostructures.

2. A new class of materials: Topological insulators

2.1. Introduction

Soon after the first predictions in 2005 by Kane and Mele [12] for graphene, followed 2006 by Bernevig *et al.* [13] for HgTe quantum wells (QW), measurements conducted by König *et al.* in 2007 [14] were able to prove the existence of the quantum spin Hall (QSH) insulator in HgTe/HgCdTe heterostructures.
The QSH effect is time reversal invariant and therefore stable against local perturbations. Unlike in a normal insulator, this effect allows transport of charge and spin in gapless states at the physical edge of the sample, while the bulk material exhibits an electronic band gap and therefore stays insulating. The formation of these states is possible due to a combination of time reversal symmetry and spin orbit interactions [9]. This new class of materials is referred to as "topological insulators" (TI) [15]. This work will focus on HgTe/HgCdTe QW systems as two-dimensional (2D) TI[1].

2.2. Classification of topological insulators

From a theoretic point of view, electronic states can be classified according to their topological invariants, as first demonstrated for the quantum Hall effect (QHE) by Thouless, Kohmoto, Nightingale and den Nijs (TKNN) [16]. The TKNN integer n gives the quantized Hall conductivity for each band $\sigma_{xy} = ne^2/h$ [17]. 2D-TIs are characterized by the $\mathbb{Z}_2$ topological number ν, which is the analogue to the Chern number, where ν is either 0 or 1, corresponding to normal or topological insulators [17, 18]. One mathematical formalism extracts this number from the bulk Bloch wavefunctions, as

[1] HgTe exhibits the behavior of a three-dimensional (3D) TI if grown with a certain strain [19]

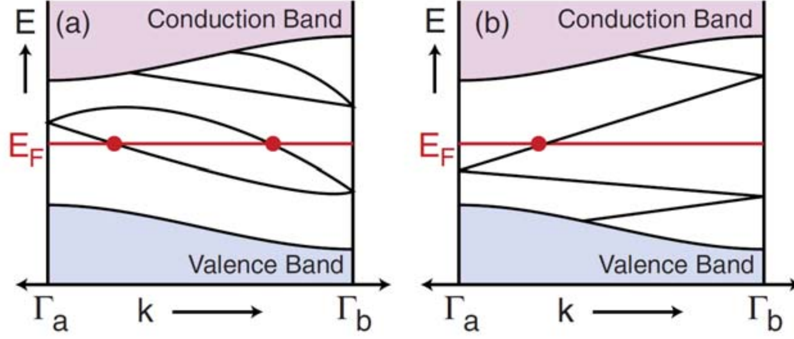

Figure 2.1.: *Examples for electronic band structures for a trivial insulator a) with an even number of band crossings with the Fermi energy E_{F} and a topological insulator b) with an odd number of crossings. Picture adapted from Ref. [9].*

shown in Ref. [17]. In real materials the wavefunctions do not necessarily need to be of the Bloch form to keep the differentiation [18] and various other possible definitions exist [9]. Since the Hall conductivity violates time reversal symmetry, the TKNN invariant has to become zero in a time reversal invariant system. However, each spin has an independent TKNN integer $n_\uparrow$, $n_\downarrow$. While the sum $n_\uparrow + n_\downarrow = 0$, the difference $n_\uparrow - n_\downarrow$ defines a quantized spin hall conductivity [17]. This is valid as long as the perpendicular component of the spin S_Z is conserved. While small perturbations can destroy the quantization of the spin Hall conductance, the topological order is preserved because the Kramers theorem prevents time reversal invariant disturbances from opening a gap at the edge states [12]. As a fundamental consequence of this classification, there have to be gapless conducting states at interfaces where this topological invariant changes. This becomes more clear when taking a closer look at the band structure of a normal and a topological insulator. Figure 2.1 shows a schematic of two different electronic band structures in the Brillouin zone $0 < k_x < \pi/\mathrm{a}$ of a 2D insulator along the edge. Colored parts indicate the bulk contributions from valence- and conduction band. In the gapped region additional states can be bound to the edges, depending on the details in the Hamiltonian, shown in Fig. 2.1 as black lines. If such states are present, the Kramers theorem requires them to be twofold degenerate at the time reversal invariant points at k = 0 and k = $\pm\pi/\mathrm{a}$, labeled as Γ_a and Γ_b. Between those points, spin-orbit interaction can lift this degeneracy. Depending on the position of the Fermi energy E_{F}, there can be multiple crossings, resulting in either an odd or even number. If the electronic states connect pairwise, as shown in Fig. 2.1 a), it is possible to get regions

without states in the gap, leading to a normal insulator, classified as $\nu = 0$. In the band connection scheme, shown in Fig. 2.1 b) however, this is not possible, leading to a topological insulator classified as $\nu = 1$. No adiabatic transformation is able to destroy these states. Every band intersecting E_F at a certain k_x has a Kramers partner at the opposite momentum $-k_x$. Therefore, we can relate the number of Kramers pairs N_K of intersecting edge modes to the change of the $\mathbb{Z}_2$ invariant across the interface, or shaped into an equation

$$N_K = \Delta\nu \bmod 2. \tag{2.1}$$

This topic is reviewed in detail by Hasan *et al.* [9].

2.3. HgTe/HgCdTe quantum wells: A 2D-topological insulator

A topological comparable band structure as the one shown in Fig. 2.1 b) is evolving at the edges of HgTe QWs. Fu and Kane showed that for inversion symmetric systems the $\mathbb{Z}_2$ invariant can be extracted from the eigenvalues ± 1 of the parity operator [20]. Despite a small bulk inversion asymmetry in HgTe because of its crystalline zincblende structure [21], this still is applicable for this 2D system [20]. Due to the change of the parity of the valence band in HgTe, the combination with CdTe or e.g. $Hg_{0.32}Cd_{0.68}Te$ can lead to a TI under certain circumstances. Based on general symmetry considerations and $\mathbf{k}\cdot\mathbf{p}$ theory, Bernevig *et al.* [13] were able to show, that the electronic states of HgTe QWs near the Γ-point can be described by the relativistic Dirac equation in 2+1 dimensions. For the critical well thickness $d = d_c$ the sign of the mass term in the Dirac equation changes, thus giving two distinct $\mathbb{Z}_2$ topological numbers for either side [13]. Focusing on the interplay between the Γ_6 and Γ_8 bands, and taking symmetry considerations into account, it is possible to write an effective Hamiltonian like in the Bernevig Hughes Zhang (BHZ) model

$$H_\mathrm{eff}(k_x, k_y) = \begin{pmatrix} H(k) & 0 \\ 0 & H^*(-k) \end{pmatrix}, \qquad H(k) = \varepsilon(k) + d_i(k)\sigma_i \tag{2.2}$$

where σ_i are the Pauli matrices [13]. The functions $\varepsilon(k)$ and $d_i(k)$ include various expansion parameters that are dependent on the heterostructure, as explained in detail

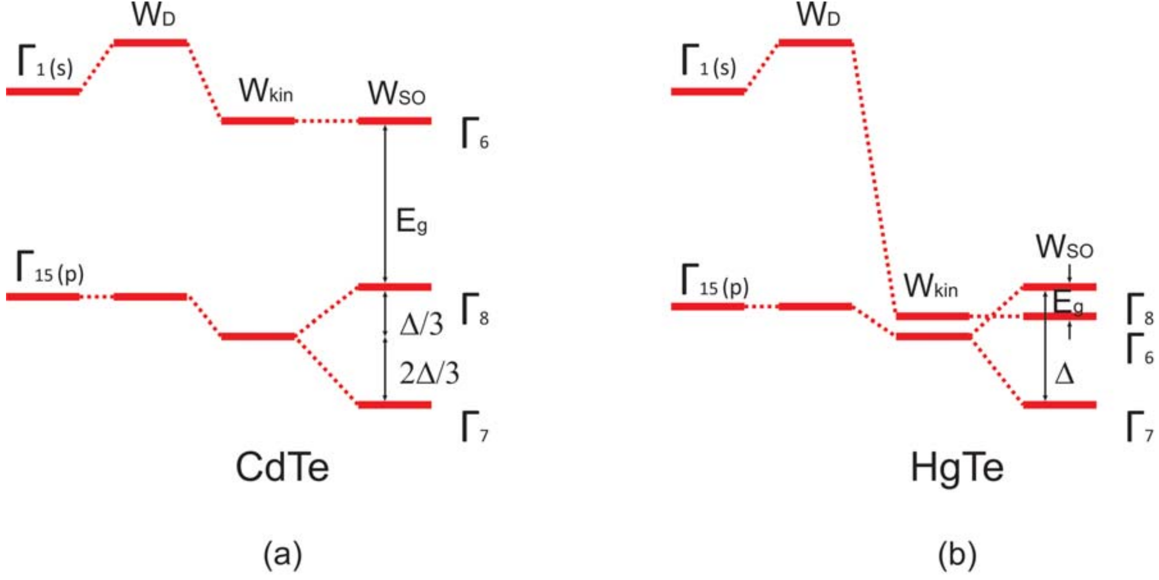

Figure 2.2.: *Illustration of the relativistic corrections of the Hamiltonian for CdTe (a) and HgTe (b). Adapted from Ref. [24].*

in Ref. [13]. Also included is the mass or gap parameter M, defined as the energy difference between the lowest electron-like subband E1 and the highest hole-like subband H1. The change in sign of this parameter at the transition and the form of the effective Hamiltonian is already sufficient to conclude the existence of QSH edge channels [13]. A descriptive picture that illustrates the change in topology between the quantum well and the confining barriers is obtained by looking at the band extrema close to Γ for CdTe and HgTe as shown in Fig. 2.2. This figure illustrates, how the different first order relativistic corrections affect the energetic position of the bands and the band gap E_{g}. The complete bandstructure can be obtained using $\mathbf{k}\cdot\mathbf{p}$ perturbation theory as illustrated in Ref. [22] by solving the Schrödinger equation

$$\left[\frac{p^2}{2m_0} + V + \frac{\hbar^2 k^2}{2m_0} + \frac{\hbar}{m_0}\boldsymbol{k}\cdot\boldsymbol{\pi} + \frac{\hbar}{4{m_0}^2c^2}\Delta V \times \boldsymbol{p}\cdot\boldsymbol{\sigma}\right] u_{n\boldsymbol{k}}(\boldsymbol{r}) = E u_{n\boldsymbol{k}}(\boldsymbol{r}) \tag{2.3}$$

with

$$\boldsymbol{\pi} = \boldsymbol{p} + \frac{\hbar}{4m_0c^2}\boldsymbol{\sigma} \times \nabla V \tag{2.4}$$

and the periodic part $u_{n\boldsymbol{k}}(\boldsymbol{r})$ of the wave function $\Psi_{n\boldsymbol{k}} = e^{i\boldsymbol{kr}}u_{n\boldsymbol{k}}(\boldsymbol{r})$ [22]. W_{D} in Fig. 2.2 denotes the Darwin term and accounts for a small zitterbewegung of the electron

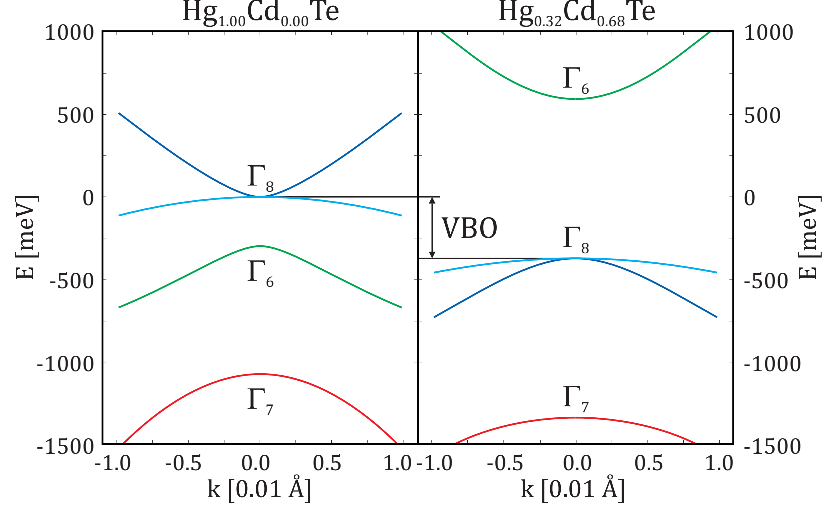

Figure 2.3.: *Bandstructures around $k = 0$ for HgTe and $Hg_{0.32}Cd_{0.68}Te$ calculated using the $\mathbf{k} \cdot \mathbf{p}$ method. Equal bands are coded in the same color. VBO indicates the valence band offset, CBO the conduction band offset. Adapted from Ref. [22].*

around the nucleus, thus lifting the s-states in energy and correcting the potential energy. This, however, only affects s-like bands since there the electron has a finite probability of presence. W_{kin} accounts for the relativistic correction of the kinetic energy. Although negligible for lighter atoms, this term has significant effect on CdTe and even more on HgTe. Together with the final spin-orbit correction W_{SO}, which lifts the $\vec{j}$-degeneracy of the p-states, this leads to an inversion of Γ_8 and Γ_6. Figure 2.3 shows the bandstructures of HgTe and $Hg_{0.32}Cd_{0.68}Te$. The calculations were performed using the $\mathbf{k} \cdot \mathbf{p}$ method in the 8×8 Kane model [22]. This model is especially suitable

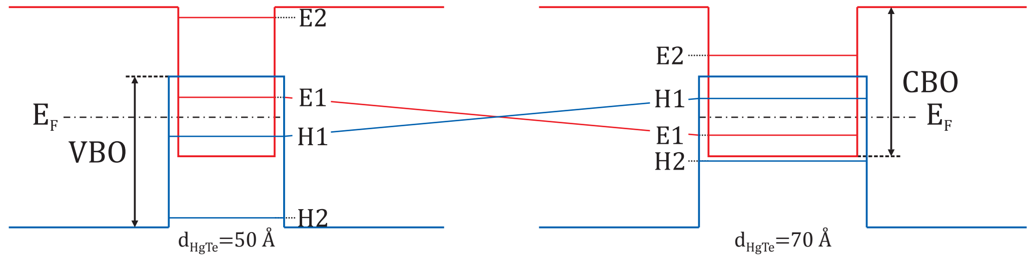

Figure 2.4.: *Illustration for the subband ordering in type-III HgTe/$Hg_{0.32}Cd_{0.68}Te$ heterostructures for a QW below and above the critical thickness d_c. Wider wells result in a descent of electron-subbands E1/E2 and a simultaneous rise of the hole-subbands H1/H2. For better visualization the Γ_8 well is displayed slightly wider than the Γ_6.*

for narrow gap semiconductors with a band gap close to $k = 0$, where an accurate treatment of the interactions between valence and conduction band is necessary [23]. It takes into account the coupling of Γ_6 to Γ_7 and Γ_8. For $Hg_{0.32}Cd_{0.68}Te$ the Γ_8 band is degenerate and splits into one light-hole band with strong dispersion and a heavy-hole band with weak dispersion. The band gap E_g is defined as Γ_6 - Γ_8 and is approximately 1 eV for $Hg_{0.32}Cd_{0.68}Te$. Note that the band gap of $Hg_{1-x}Cd_xTe$ can be adjusted in a wide range by changing the parameter x during growth, leading e.g. to a zero gap ($E_g \approx 0$ eV) material for $x \approx 0.17$ [24–26]. Because of the band inversion, however, the Γ_8 light-hole band in HgTe now shows electron like dispersion and becomes the conduction band, while the Γ_8 heavy-hole band remains the valence band. The Γ_6 band, now shifted below the Γ_8, also exhibits hole like dispersion. Following the initial definition, this leads to a band gap of approximately -0.3 eV. Bulk HgTe is

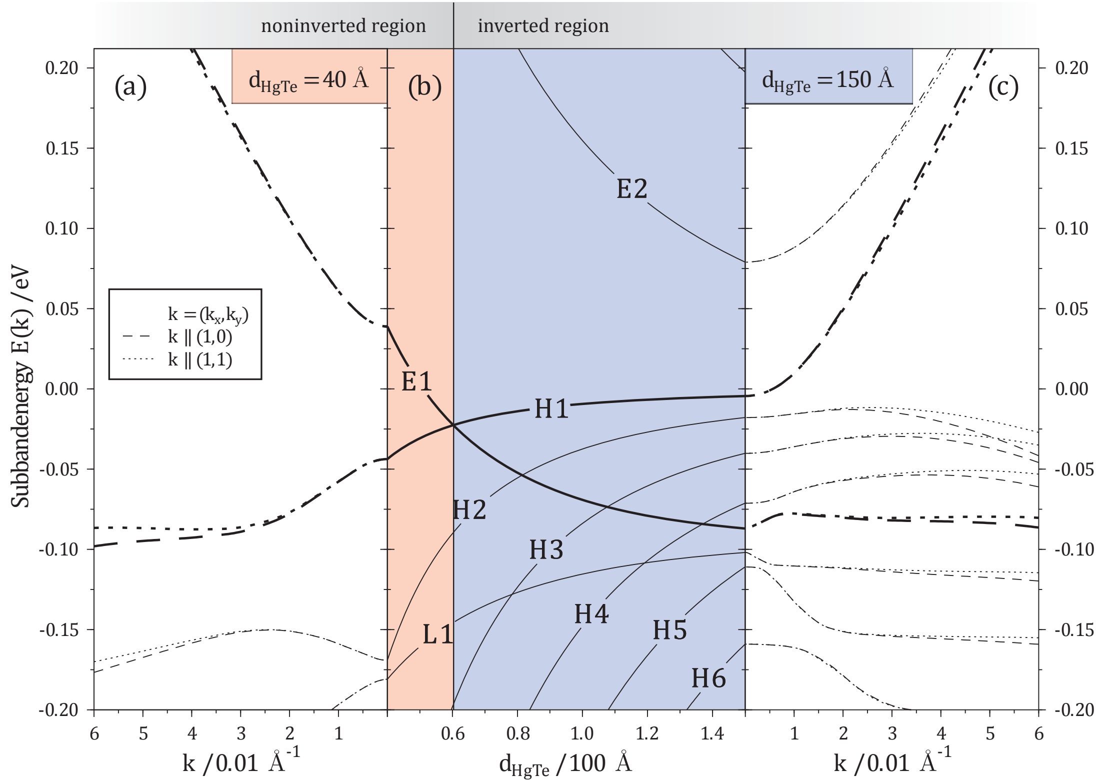

Figure 2.5.: *a) Subband dispersion for a 4 nm QW. b) Subband ordering of electron (E1/E2) and light hole/heavy hole bands (L1/H1-H6) as a function of QW thickness. The critical thickness d_c at* 6.3 nm *separates the non-inverted (red) from the inverted region (blue). c) Subband dispersion for a* 15 nm *QW. Adapted from Ref. [22].*

a semimetal, where a gap of several meV in the degenerate Γ_8 band can be opened by strained growth, thus making it a 3D TI [19]. If we combine both materials and confine a layer of HgTe between two barriers of $Hg_{0.32}Cd_{0.68}Te$, we are able to realize a type-III quantum well as shown in Fig. 2.4. Depending on the thickness of the HgTe layer it is possible, due to the confinement, to realize samples with a positive band gap (non-inverted) as well as samples with an inverted band structure. Figure 2.5 b) shows the subband ordering as a function of well thickness, calculated for a CdZnTe (001) substrate. Figure 2.5 a) shows the dispersion relation for a 40 Å well, Figure 2.5 c) the dispersion for a 150 Å well. This calculation as well as the analogue for CdZnTe (112) are explained in Ref. [22]. The critical thickness d_c where the band gap reaches zero and thus separates the inverted from the non-inverted regime is approximately 63 Å. This critical thickness was confirmed in various measurements [14, 27]. The experiments of Büttner *et al.* [27] not only confirm convincingly this critical thickness, but also demonstrate the Dirac like behavior at this point.

2.4. Remarkable experiments on HgTe QWs

Knowing the characteristics of the band structure of HgTe/HgCdTe heterostructures the potential of this system becomes obvious. It allows to study the behavior of a normal semiconductor and a topological insulator in the same material. To convincingly demonstrate this fact König *et al.* [14] fabricated and measured samples, with well widths varying from 55 Å to 73 Å to study both regimes. Some of their results are shown in Fig. 2.6. The measurement shows the longitudinal resistance of Hall bar structures with various dimensions for non-inverted (I) and inverted QWs (II-IV) as a function of gate voltage on a logarithmic scale. The carrier density can be controlled in a wide range, thus allowing the transition between n-conduction and p-conduction. Note that the conductance G for sample I is almost dropping to zero as the Fermi energy is tuned into the gap, while for the other samples a finite conductance remains. In fact the conductance for shorter samples of 1 µm and 0.5 µm (III and IV) is close to the quantized value of $2e^2/h$, as expected for edge channel transport. This is furthermore supported as this value is not depending on the device width [14]. For longer samples (II) a deviation from the quantized value is observed, but the resistance is still at least two orders of magnitude lower than in the non inverted case. A look at the schematic sketch in Fig. 2.7 explains the positioning of the conducting edge channels. This picture

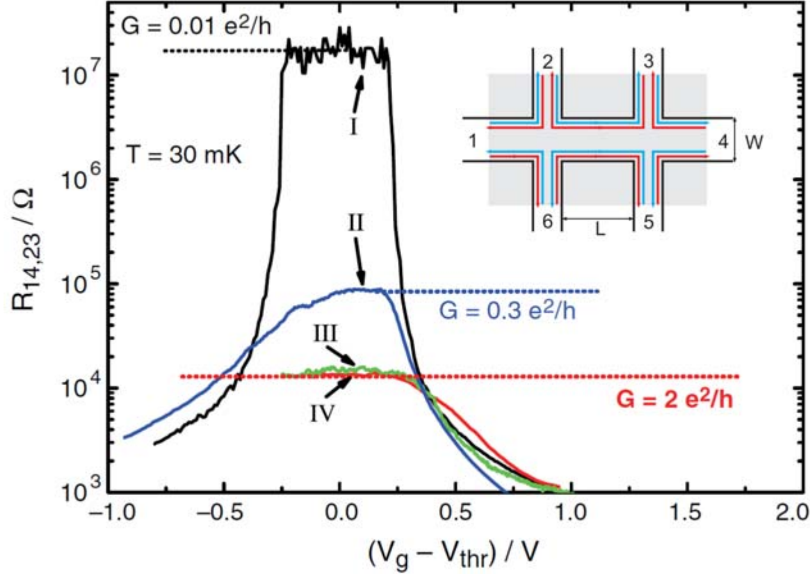

__Figure 2.6.:__ Longitudinal resistance of Hall bar structures as a function of gate voltage for non-inverted (I) and inverted QWs (II-IV). The inset shows a sketch of the six-terminal sample geometry [14].

is the analogue to the QHE picture described in Ref. [28]. The lowest states are shown for valence and conduction band. Because of the boundary conditions and the different Dirac mass, electron-like bands bend upwards while the hole-like bands bend down. For the inverted QWs this leads to a crossing of the bands. If the Fermi level E_{F} is as indicated, the only occupiable states are at the sample edge, while the bulk stays insulating. Unlike in the QHE, these channels are helical and not chiral, carrying opposite spin forming a Kramers doublet counter-propagating at the edge [29, 30]. In case of a band ordering as shown in Fig. 2.7 b) the observed conductance is stable as long as E_{F} lies in the nominally insulating region. For non-inverted samples, as shown in Fig. 2.7 a), there is a real band gap and the conductance drops to zero. The observed conductance, however, does not necessarily have to be $2e^2/h$. Indeed this depends on the number of contacts to the QSH area and the measurement configuration. The experiments of Roth *et al.* in 2008 focusing on non-local transport measurements were able to show that the quantization does not come from ballistic transport but has its origin in real edge channel transport [31]. For that purpose they used six-terminal samples with an additional topgate, allowing to tune all terminals into the QSH regime and to probe various contact configurations. Parts of these measurements are shown in Fig. 2.8. The observed resistance values in the nominal insulating zone agree with the

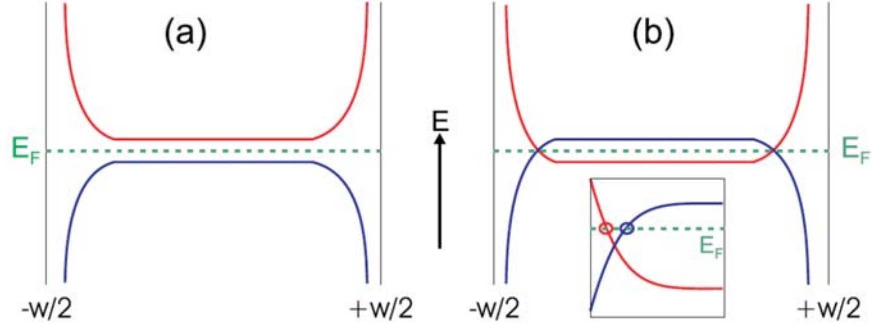

Figure 2.7.: *Sketch for the lowest states in valence- (blue) and conduction band (red) for a normal a) and an inverted bandstructure b) for a sample with width w. Because of the boundary conditions this leads to a crossing at the sample edge only for inverted structures (inset), forming the QSH channels [123]*

predicted values that can be calculated from the Landau-Büttiker formalism [28, 32]. There, the current voltage relationship may be written as

$$I_{\mathrm{i}} = \frac{e^2}{h}\left[(N_i + R_i)V_i - \sum_{j\neq i} T_{ij}V_j\right], \tag{2.5}$$

where I_{i} is the current from the ith electrode and $V_i = \mu_i/e$ the voltage at the ith electrode. T_{ji} denotes the transmission probability from the jth terminal to the ith and R_i takes back-scattering into account. For our time reversal invariant system, T_{ij} is equal to T_{ji}. Unlike in a normal two-dimensional sample where the transmission matrix and the number of modes N_i are depending on the device width and are non-universal, in case of edge channel transport it can be well defined.
If we think of one chiral channel as in the $\nu = 1$ QH state, the transmission matrix elements from i^{th} to $(i+1)^{th}$ electrode are given as $T(QH)_{i+1,i} = 1$ for $i = 1,...,N$ while the other matrix elements vanish. The transmission between neighboring terminals is considered to be perfect on one side, since the edge states are protected from back-scattering. Taking the Hall bar structure from Fig. 2.6 as an example, this leads to a four terminal resistance $R_{14,23} = 0$ and a two terminal resistance $R_{14,14} = h/e^2$. In case of the helical QSH edge states, channels with opposite spin are counter-propagating on the same edge, but unlike in the QH the current is injected in two channels on opposite sample edges. Therfore the QSH states can be viewed as a copy of two time reversal connected QH states. The difference for both systems is

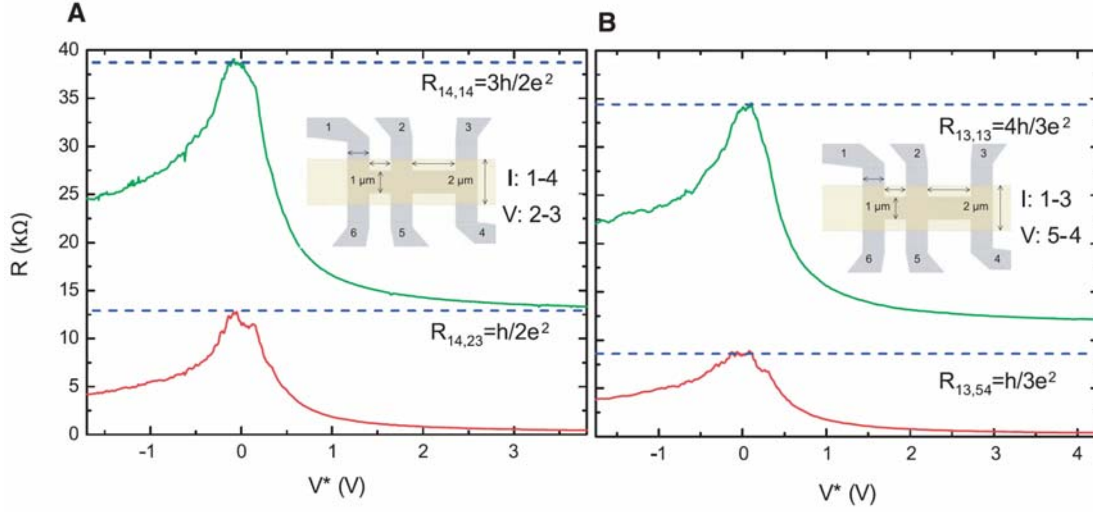

Figure 2.8.: *Two- and four-terminal measurements on a six-terminal device as a function of gate voltage for various contact configurations. Dotted lines indicate the expected values as calculated from the Landauer-Büttiker formalism [31].*

illustrated schematically in Fig. 2.9. The transmission between neighboring partners in the QSH regime is again considered perfect, because of time reversal protection. Therefore $T(QSH) = T(QH) + T^{\dagger}(QH)$ and the transmission matrix is given by $T(QSH)_{i+1,i} = T(QSH)_{i,i+1} = 1$. In the same measurement configuration as given above, we observe now a four terminal resistance of $R_{14,23} = h/2e^2$ and a two terminal resistance of $R_{14,23} = 3h/2e^2$, as is shown in Fig. 2.8 and explained in detail in Ref. [31]. The remaining four terminal longitudinal resistance can be explained by the interaction of the channels with the electronic reservoirs in the voltage leads, where time reversal symmetry is effectively broken by the macroscopic irreversibility once the phase coherence is destroyed. The current flow between the contacts, however, can be considered dissipationless. Although protected by time reversal symmetry, metallic defects, either introduced during MBE growth or because of inhomogeneous gate action at interface traps, can also lead to dephasing and can therefore act like an additional ohmic contact. A voltage probe maintaining zero charge current provides momentum relaxation. The spin current into the contacts, however, is non zero. Only half of the carriers can propagate and continue their way. The half that flipped spin has to stay in the contact because the potential at the original contact prevents them from flowing back. The observed resistance values can always be reduced to integer fractions of h/e^2.

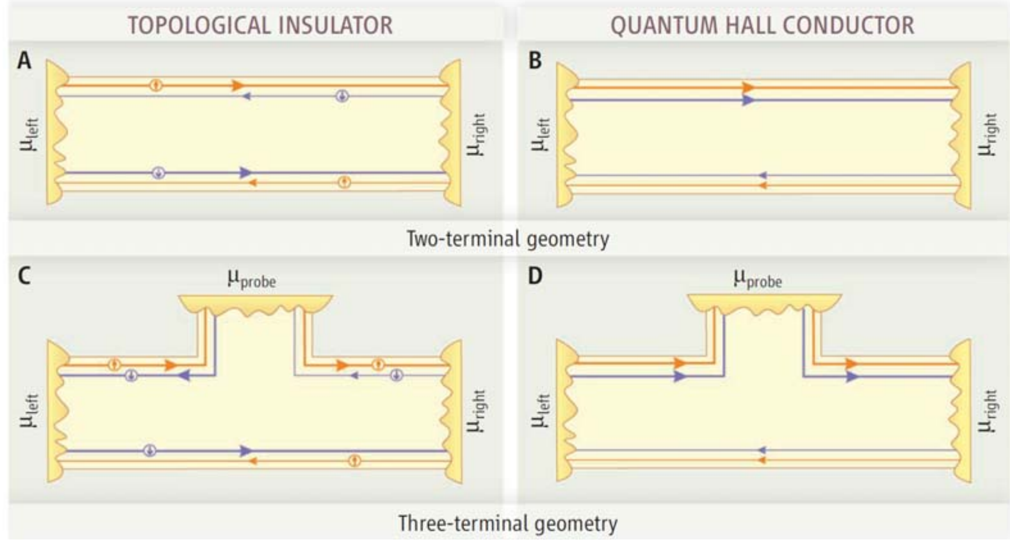

Figure 2.9.: *Illustration of the difference between QH and QSH edge channel transport for two and three terminals. In both cases μ_{left} is the higher chemical potential and drives the current to the right. The line thickness corresponds to the occupancy of the states. In the QH conductor the current flows on one side (B), while in the TI the transport is equal on both sides (A). Adding an extra terminal μ_{probe} in the QH state changes nothing (D), in the TI however (C), conductance is cut by half a conductance quantum, because of the current flowing back. Adapted from Ref. [33].*

Figure 2.9 shows a comparison of the edge channel transport of a TI and a QH conductor. Figure 2.9 c) shows a net spin up current into the probe contact in case of the TI. This simultaneously induces a spin current between source and drain [33]. Using structures in the shape of an H, by combining two of the three-terminal devices from Fig. 2.9, and having separately controllable gates for each branch, Brüne *et al.* [35] in 2012 were able to confirm the spin polarization of the edge channels. Conceptually it is difficult to observe spins directly in transport measurements, since these are always based on probing currents and voltages. However, the HgTe/HgCdTe system exhibits the Spin Hall effect (SHE) [34, 35]. This is due to the large spin orbit coupling that is present in HgTe/HgCdTe inverted QWs [8, 53]. In the SHE, a charge current induces a spin current and vice versa, consequently called inverse Spin Hall effect (SHE^{-1}). The complementary measurement configurations are shown in Fig. 2.10. If a charge current is injected into the metallic area (marked in green) the intrinsic SHE will lead to a separation of opposite spins to opposite edges of this branch, leading to different chemical potentials of different spin states. At the interconnection of the two branches,

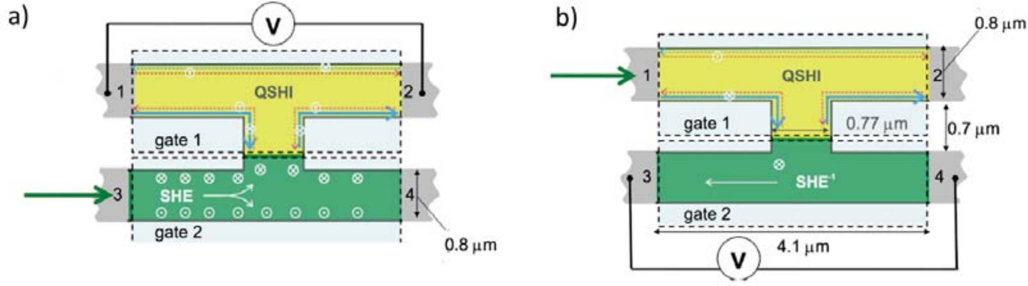

Figure 2.10.: *Schematic of two complementary measurements for probing the spin polarization of the QSH edge states.* ***a)*** *Current is injected into the metallic branch (green). Because of the intrinsic SHE, different spins accumulate at opposite sample edges. At the interconnection, the spins are only allowed to populate the matching channel, leading to a detectable voltage at contacts 1 and 2.* ***b)*** *Current is injected into the QSH branch. Different spins propagate at opposite sample edges, thus injecting a spin current into the metallic region. This again leads to a detectable voltage because of the inverse SHE [35].*

the spin current is able to enter the QSH region (marked in yellow) where only the edge channels are available for transport. In case of spin polarization of the edge channels, the spins are only able to enter the matching channel, thus being selectively directed to one side of the upper branch. This leads to a voltage that can be measured between contacts 1 and 2. For unpolarized channels the expected voltage is zero. The second measurement configuration reverses injector and detector branch. In that case a current is injected into the QSH branch. For spin polarized channels, carriers with opposite spin will travel at opposite edges. At the connection between the QSH and the metallic branch a net spin current is injected into the metallic area because of the different spin state occupancy. This leads to the inverse spin Hall effect where a voltage is induced between contacts 3 and 4. Further investigations of different injector and detector configurations qualitatively and quantitatively confirm the spin polarization of the states [35]. Recent experiments done by Nowack *et al.* [36] make it possible to image the current transport at the sample edges. This was done by probing the magnetic field, that is generated by this current, using a superconducting quantum interference device (SQUID). The measurement setup is illustrated in Fig. 2.11 a). Figure 2.11 b) shows the transport configuration of the Hall bar sample, while the acquired two terminal resistance as a function of gate voltage is given in Fig. 2.11 c). Figure 2.11 also shows the difference between the two transport regimes on inverted QW samples. If the transport is dominated by bulk conduction, there is a smooth crossing of the magnetic

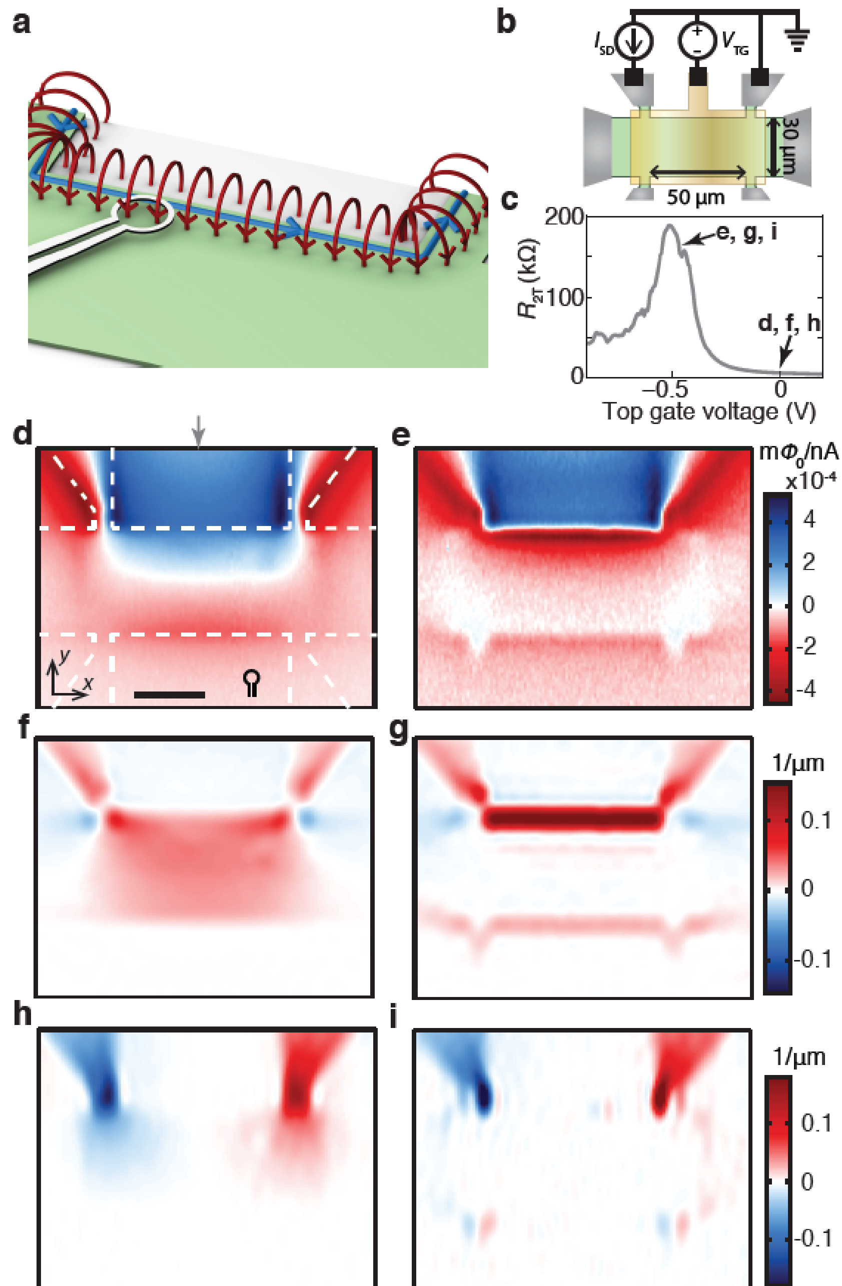

Figure 2.11.: ***a)*** *Illustration of the measurement. The current (blue) induces a magnetic field (red) that can be picked up with the SQUID.* ***b)*** *Transport configuration of the Hall bar.* ***c)*** *Two-terminal resistance versus gate voltage.* ***d, e)*** *Flux images at gate voltages as indicated in c). In d) white dashed lines indicate the Hall bar mesa, the black stripe indicates a scale of 20 µm.* ***f, g)*** *X-component,* ***h, i)*** *y-component of the current density, obtained from the current inversion of the flux images from d) and e). From Ref. [36].*

profile through zero across the Hall bar, corresponding to homogeneous transport in the whole sample area as shown in Fig. 2.11 d). However, in Fig. 2.11 e) the transport is dominated by the edge channels, visible from the two steep crossings through zero at the top and bottom edge. The current density in Fig. 2.11 f) - i) was visualized using Biot-Savarts law, which links the current density to the magnetic profile [36]. This indicates that the current has to flow mainly at the sample edges. Another technique for visualizing the edge channel transport is the scanning gate method described in Ref. [38]. Advances in HgTe lithography [37] provided the basis for the experiments by König *et al.* [38], allowing to study spatially resolved the scattering in the QSH states.

2.5. Summary

All presented studies result from a growing interest in TIs over the last few years, because of their unique electronic transport behavior and associated possible future applications. The spin polarization and the robustness of these states might provide an interesting possibility to achieve the formation of spin polarized currents and the opportunity to control them electrically, which could yield completely new spintronic based devices. Since the edge states can be used to direct electron beams between different terminals analog to directed photons in optics, they are very interesting for quantum information and quantum processing. The first steps into this direction require the realization of fundamental devices such as e.g. quantum point contacts (QPCs) [33]. To pave the way for applications it is also reasonable to study the robustness of the QSH states against various influences. Although there are many predictions for novel TI materials, only few are currently accessible in transport measurements. This work consequently focuses on the fabrication of micro- and nano-devices in these material systems. Their special electronic properties and material sensitivity makes sample preparation a challenging task and demands the development of new fabrication processes. Refining the lithography for these material systems provides the key to new exciting experiments that will lead to new insights.

3. Quantum point contacts in HgTe/HgCdTe heterostructures

3.1. Motivation

Quantum point contacts have become fundamental structures for transport measurements in semiconductor systems and are meanwhile well understood. The possibility to study quasi one dimensional transport has lead to the discovery of many new phenomena in the past, that have not been anticipated by theory before [39]. Therefore it is not surprising, that there are various proposals to implement these one dimensional constrictions in topological insulator materials, to build new devices and probe the nature of the helical edge channels [40–48]. Especially since the transport in these channels happens dissipationless, it occurs to be interesting for spintronics [49]. HgTe/HgCdTe heterostructures provide a promising environment for the realization of spin processing devices [50]. This is not only due to the spin polarized QSH edge channels, but also because of the considerable large Rashba type [51] spin orbit interaction (SOI) strength that can be achieved in these heterostructures [8, 52, 53]. In addition this SOI can be controlled via external gates [8]. This combination could allow for electron optic experiments as already proposed by Khodas *et al.* in 2004 [89]. Other proposals suggest QPCs as connectors between the edge states with different spins, to achieve a controlled charge and spin switching [50, 54–56]. Usually these states are well separated at opposite sample edges and scattering is forbidden. However, in such an one dimensional constriction, because of their finite width, these edge channels can overlap and interaction becomes possible again [57].
An all electrical quantum manipulation of the spin degree of freedom of electrons is crucial in the field of spintronics and quantum information processing [58]. The aim is to show alternative ways to realize a spin transistor comparable to the proposal from Datta and Das from 1990 [7]. Despite all theoretical predictions, the experimental

realization and demonstration of a working QPC device in this new class of materials has not yet been reported. In this work we present first results and characterizations of QPCs realized in HgTe/HgCdTe QWs. We also give a detailed insight into the concomitant challenges that have been met and discuss remaining obstacles for further applications and improvement.

3.2. QPCs in a nutshell

One reason QPCs have not yet been established in topological insulators is the lack of high quality material, despite reports for high and ultrahigh carrier mobilities of up to 20×10^3 cm^2/Vs [59–61]. In contrast to these values, HgTe/HgCdTe 2DEGs exhibit mobilities up to 1.2×10^6 cm^2/Vs, two orders of magnitude larger then in other established TI materials [62]. The first controllable point contact structures in a two-dimensional electron system, that clearly showed characteristics of one dimensional ballistic transport, were presented independently by Wees *et al.* and Wharam *et al.* [63, 64] in 1988. This became possible due to major advances in GaAs/Al$_x$Ga$_{1-x}$As 2DEG quality, providing carrier mobilities of 850×10^3 cm^2/Vs. Indications were already observed in lower quality samples (200×10^3 cm^2/Vs) two years earlier by Thornton *et al.* [65].
A quantum point contact is a short constriction with a width in the order of the Fermi wavelength λ_F [39]. Within the two dimensional electron gas, where usually only one subband is populated, this leads to an additional quantization $E_{n,y}$ and the formation of one dimensional subbands where the electrons are free to move along a single direction. This leads to a dispersion relation that can be described as

$$E_n(k_x) = \frac{\hbar^2 {k_x}^2}{2m^*} + E_{n,y}. \tag{3.1}$$

Due to the one dimensional dispersion, edge channels and one dimensional subbands may be viewed as propagating modes in an electron wave-guide [39]. Because of that analogy, the quantum Hall effect and the quantum size effects in narrow constrictions in the ballistic transport regime can be described similarly. The most pronounced resemblance is the quantization of the conductance in multiple integers of $2e^2/h$, although in QPCs this is observed without the presence of a magnetic field.

3.2.1. Conductance quantization

One way to define such a one dimensional channel in a 2DEG, as realized in Refs. [63–65], is by applying a gate voltage to so called split gate electrodes. In case of a smooth potential landscape in the channel, as can be assumed in split gate defined point contacts, the constriction can be described by a saddle potential as suggested in Ref. [66]

$$V(x,y) = V_0 - \frac{1}{2}m{\omega_x}^2x^2 + \frac{1}{2}m{\omega_y}^2y^2. \tag{3.2}$$

There V_0 is the electrostatic potential at the saddle and ω_x and ω_y describe the curvatures. For globally adiabatic transport between two reservoirs, the conductance can be quite accurately calculated by looking at the local scattering at the saddle itself [66–70]. The total energy is given by the potential in Eq. 3.2 plus a kinetic energy term $p^2/2m$. The Hamiltonian can be separated into a transverse wave function with the energies $\hbar\omega_y(n+1/2)$, n = 0,1,2,3... and a wave function for propagation along x in the effective potential [66]

$$V_0 - \frac{1}{2}m{\omega_x}^2x^2 + \hbar\omega_y(n+\frac{1}{2}). \tag{3.3}$$

The effective potential defines the bottom of the nth subband in the saddle point [68]. The energy

$$E_n = V_0 + \hbar\omega_y(n+\frac{1}{2}) \tag{3.4}$$

defines the transport through the constriction. For $E_n < E_\mathrm{F}$ the channels are open for

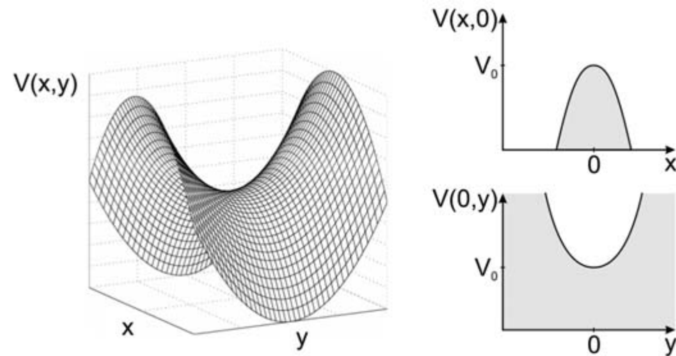

Figure 3.1.: *Illustration of the saddle potential with cross sections in x and y direction. Grey shaded areas indicate potential barriers for electrons.*

transport, while for $E_n > E_\mathrm{F}$ the channels are closed [66]. This can be visualized by looking at a saddle point and its cross sections in x and y direction, as illustrated in Fig. 3.1. Grey shaded areas resemble areas forbidden for transport. Transmission from one reservoir to the other is only possible if the incident channel n and the outgoing channel m are the same, otherwise it will be zero. This can be expressed as shown in Ref. [66] in an equation

$$T_{mn} = \delta_{mn}\frac{1}{1+e^{-\pi\varepsilon_n}}, \tag{3.5}$$

with

$$\varepsilon_n = 2[E - \hbar\omega_y(n+\frac{1}{2}) - V_0]/\hbar\omega_x. \tag{3.6}$$

Figure 3.2 shows a calculation of the total transmission probability of a saddle potential with the ratio $\omega_y/\omega_x = 3$. The successive opening for additional channels leads to a quantization in conductance. The conductance is then given by [65, 66, 71]

$$G = \frac{e^2}{h}T \tag{3.7}$$

with the sum over all transmission probabilities $T = \sum_{mn} T_{mn}$. So for perfect trans-

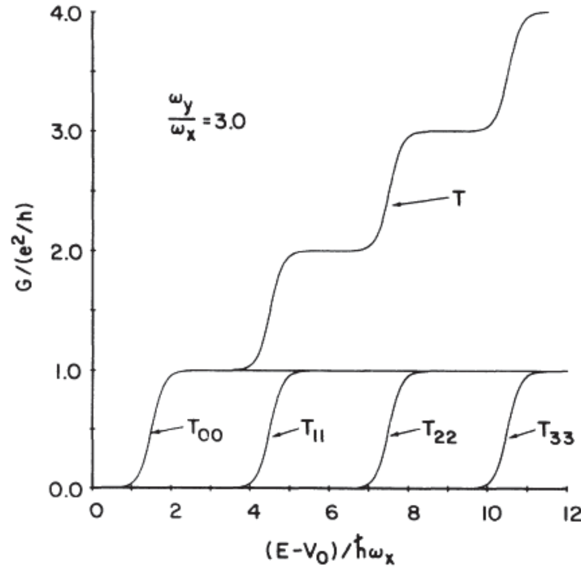

Figure 3.2.: *Calculation of the single channel transmission probability T_{nn} and the total conductance $T = \sum_{nn} T_{nn}$ as a function of $(E - V_0)/\hbar\omega_x$ for a ratio of $\omega_y/\omega_x = 3$, adapted from Ref. [66].*

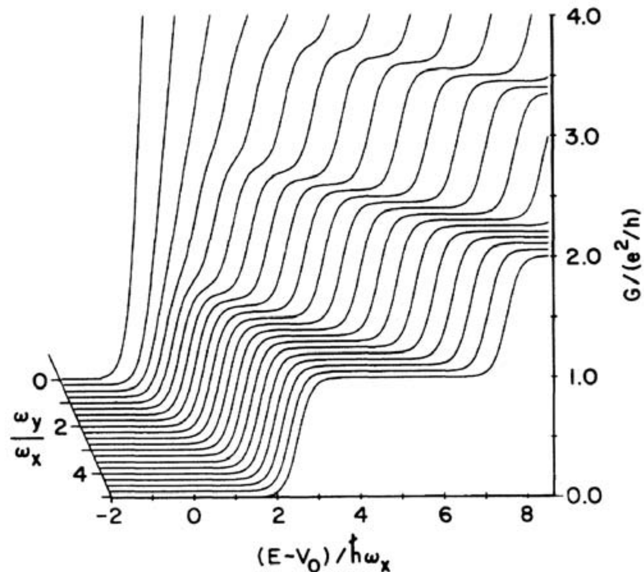

Figure 3.3.: *Conductance of an adiabatic constriction as a function of $(E-V_0)/\hbar\omega_x$ for different ratios of ω_y/ω_x. From Ref. [66].*

mission the total conductance can be written as

$$G = g_s \frac{e^2}{h} N, \tag{3.8}$$

where g_s takes the spin degeneracy into account and N denotes the number of occupied modes. The number of occupied modes can be varied either by changing the constriction width W or by changing the Fermi energy E_F.
A requirement to observe well pronounced steps in the conductance is that $\omega_y \geq \omega_x$ [66]. This dependence is illustrated in Fig. 3.3. The definition for an adiabatic transition can be framed as in Ref. [72, 73] as

$$\frac{dW}{dx} \lesssim \frac{1}{N(x)} \qquad \text{with} \qquad N(x) \approx \frac{k_\mathrm{F} W(x)}{\pi}. \tag{3.9}$$

To get the condition for perfectly quantized steps, a reflectionless transmission between the one-dimensional constriction and the wider regions of the 2DEG has to be satisfied [72, 74]. Reflection within the QPC can have reasons like defects or scattering at the boundaries. But even for a perfectly clean device the transmission also depends on proper mode coupling [75]. While in the wider contact regions $+k$ and $-k$ states have

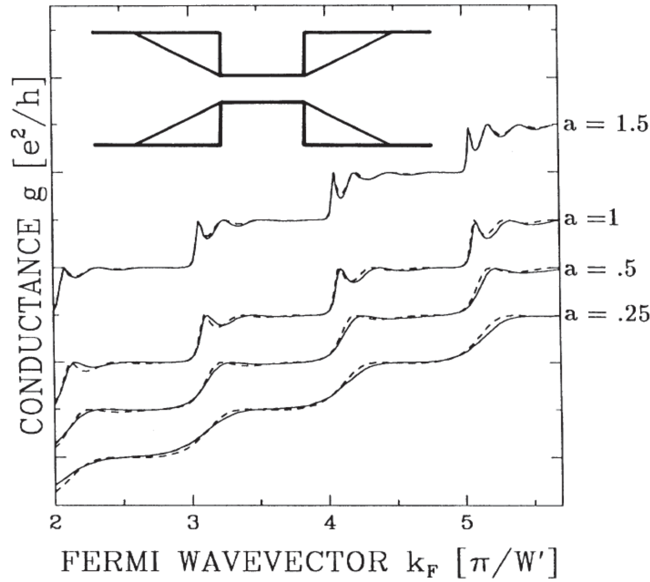

Figure 3.4.: *Calculation of conductance g for different aspect ratios a = L/W for abrupt transitions. Adapted from Ref. [75].*

nearly the same Fermi-level, within the narrow ballistic regions only a few modes are available for transport, resulting in a noticeable difference between the energy levels [74]. Figure 3.4 demonstrates the impact of aspect ratio in an abrupt constriction on the observed conductance plateaus. Even if the low temperature mean free path is much longer in the wider 2DEG regions than the actual constriction lengths, deviations can occur as has been demonstrated by Timp *et al.* [73, 76].
In summary, a reflectionless transport can be realized by forming an adiabatic transition between the two reservoirs, rather then an abrupt QPC [75]. In realistic devices the transition can only be partly adiabatic which is usually still satisfactory to observe good quantization [72, 75]. However, deviations can occur because of non-unit transmission probability of propagating modes and non-zero transmission of evanescent modes [73]. Besides the geometry and exact shape of the constriction, the observed conductance steps, as already mentioned, also depend on scattering from defects, the sample boundaries and temperature [72]. Below a certain temperature quantum-interference effects will become more visible on top of the plateaus while for higher temperatures they will acquire a finite slope, until they can no longer be resolved. This is mainly due to the smearing of the Fermi-Dirac distribution [73]. Devices that do not have a specular reflection on the walls and rather show diffusive transport will no longer exhibit

quantization steps.

3.2.2. Electron beam collimation

Another fascinating consequence of ballistic transport through a point contact is the angular selection of incoming and therefore also outgoing electron modes. In fact this is a result of classical mechanics [77]. Mode selection is achieved by the gradual narrowing of the constriction at the entrance and the continuous widening at the exit, referred to as horn collimation, and the introduced potential barrier in the constriction. Both lead to a restriction for the electron momentum in k_x. As illustrated in Fig. 3.5 a) only electrons with a sufficiently large impulse in k_x direction can overcome the potential barrier. Because of its conical entrance, electrons with an incoming angle larger than α are reflected as outlined in Fig. 3.5 b). Thus, the initial injection cone of its value of π is reduced to a angle of $2\alpha_{\text{max}}$. For a wave moving adiabatically along a guide the number of modes n is preserved. For a constriction with gradually decreasing width W, this implies that the transverse energy is constantly reduced, while the longitudinal one increases [78]. Note that the product of channel width and absolute transverse momentum $|k_y|\,W \equiv S$ is approximately constant from the point contact entrance to its exit [73] in the adiabatic picture. It turns out, that for an abrupt opening of the constriction into the 2DEG the transverse momentum is conserved, therefore leading to a collimated electron beam [78–80]. Analytically, the collimation effect can be calculated as illustrated in Ref. [73]. We assume the maximal potential above the edge of the conduction band in the 2DEG region E_{c} is at the minimal width

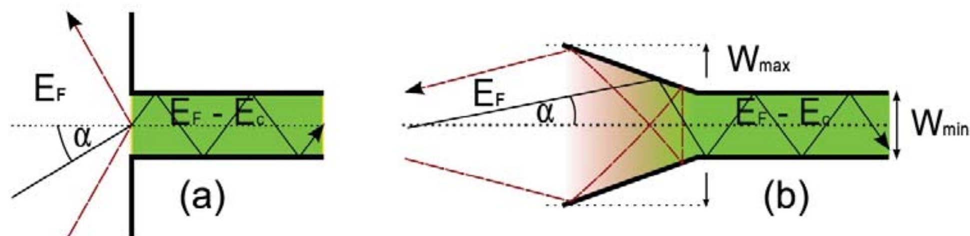

Figure 3.5.: *Illustration of the collimation effect for an abrupt potential barrier of height E_{c}* ***a)*** *and a horn shaped structure* ***b)****. Different electron trajectories are outlined. For both cases electrons approaching at an angle α (red dashed lines) are reflected. Shaded areas indicate the potential barrier, W_{min} and W_{max} denote the minimal and maximal constriction width. Adapted from Ref. [78].*

of the constriction $W_{\min}$. Thus, the maximal value of S can be determined as

$$S_1 \equiv \sqrt{\frac{2m}{\hbar^2}} \cdot \sqrt{E_\mathrm{F} - E_\mathrm{c}} \cdot W_{\min}. \tag{3.10}$$

Assuming adiabatic transport until the constriction reaches its maximum width $W_{\max}$, we determine

$$S_2 \equiv \sqrt{\frac{2m}{\hbar^2}} \cdot \sqrt{E_\mathrm{F}} \cdot \sin\alpha_{\max} W_{\max}. \tag{3.11}$$

Because of the invariance of the product of momentum and channel width it follows that $S_1 = S_2$ and hence

$$\alpha_{\max} = \arcsin\left(\frac{1}{f}\right), \text{with } f = \sqrt{\frac{E_\mathrm{F}}{E_\mathrm{F} - E_\mathrm{c}}} \cdot \frac{W_{\max}}{W_{\min}}. \tag{3.12}$$

The variable f is referred to as the collimation factor and takes both barrier and horn collimation into account.
Using the expression for the classical point contact resistance

$$R_\mathrm{QPC} = \frac{h}{2e^2} N = \frac{h}{2e^2} \frac{\pi}{k_\mathrm{QPC} \cdot W_{\min}}, \tag{3.13}$$

with

$$k_\mathrm{QPC} = \sqrt{\frac{2m(E_\mathrm{F} - E_\mathrm{c})}{\hbar^2}} \tag{3.14}$$

the collimation factor can be rewritten as demonstrated in Ref. [81] as

$$f = R_\mathrm{QPC} \frac{2e^2}{h} \cdot \frac{k_\mathrm{F} W_{\max}}{\pi} = \frac{N_{\max}}{N}. \tag{3.15}$$

The collimation factor f is therefore depending on the ratio of incoming $N_{\max}$ and actual transmitted electron modes N and thus is a measurement of the point contacts' mode selectivity. The angular distribution of the injection is given in Ref. [73] as

$$P(\alpha) = \begin{cases} \frac{1}{2} f \cos\alpha & \text{for } |\alpha| < \alpha_{\max} \\ 0 & \text{otherwise} \end{cases}. \tag{3.16}$$

One possible way to visualize the collimation effect experimentally was demonstrated by Molenkamp *et al.* [81] using two opposite point contacts, based on the observation

of Wharam *et al.* that the series resistance of two opposite point contacts formed in a 2DEG is non-additive [82]. Figure 3.6 a) illustrates the device layout used for the experiment with two sets of opposite point contacts in a distance of $L = 4$ µm. One is serving as an injector, the opposite as a collector. By sweeping a perpendicular magnetic field, it is possible to deflect the injected electron beam and map the beam profile by measuring the collector voltage V_c relative to the ground potential. The injector current I_i is grounded to either one - (four-terminal measurement) or two sides (three-terminal measurement) of the 2DEG channel which is separating the two QPCs. The transmission probability for such a geometry follows from Eq. 3.16 and is in the semiclassical model given by

$$T_d = f\frac{W_{max}}{2L}N, \tag{3.17}$$

for N occupied subbands. For a three terminal geometry at $B = 0$ T this leads to

$$\frac{V_c}{I_i} = \frac{1}{G}\frac{T_d}{N}, \qquad \text{for } T_d << N \tag{3.18}$$

as a consequence of the Landauer Büttiker formalism [78]. Expanding Eq. 3.18 by adding the expression for the two-terminal point contact resistance 1/G and substituting T_d with Eq. 3.17 we get the expression for the non-local resistance $R_{NL,3t}$

$$R_{NL,3t} = \frac{V_c}{I_i} = \frac{h}{2e^2}f^2\frac{\pi}{2k_F L}, \tag{3.19}$$

as illustrated in Ref. [73]. This gives the possibility to extract the collimation factor f from the collector voltage V_c [81]. A similar expression can be found for the four-terminal case [73],

$$R_{NL,4t} = \frac{V_c}{I_i} = \frac{h}{2e^2}(f^2 - \frac{1}{2})\frac{\pi}{2k_F L}. \tag{3.20}$$

Small values of the magnetic field are already sufficient to bend the beam away from the detecting QPC [81]. This is demonstrated in the measurement (solid line) shown in Fig. 3.6 a) at values of roughly $B = 0.05$ T. The resulting non-local resistance V_c/I_i is compared to a simulation using the semiclassical model (dots) and the expected profile without collimation (dashed line). Figure 3.6 b) shows the corresponding angular distribution of the injection, calculated for a collimation factor of $f = 1.85$ at $B = 0$ T.

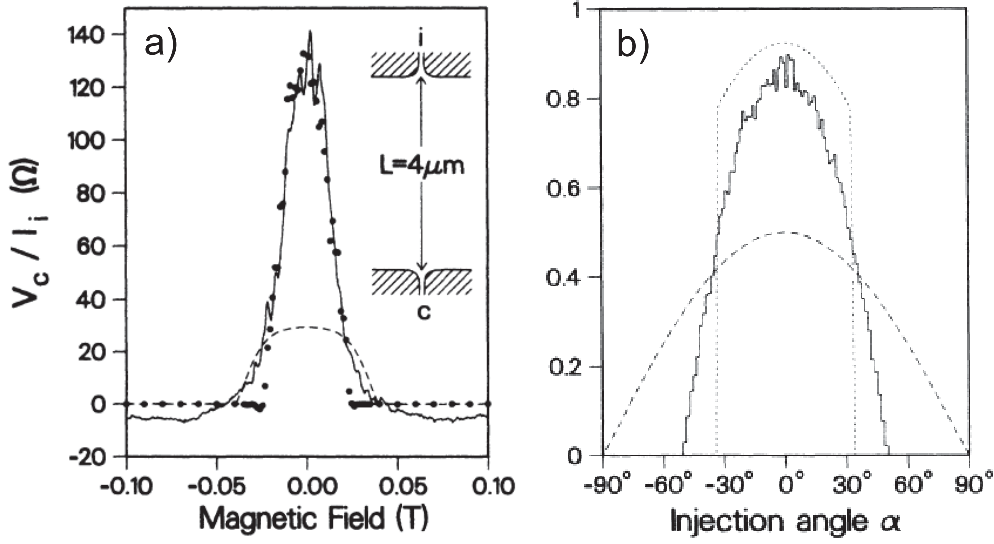

Figure 3.6.: ***a)*** *Plot of the collector voltage* V_c *divided by the injector current* I_i *versus magnetic field. The solid line shows the experimental data, dots show simulation results, dashed lines show the expected signal without collimation* ***b)*** *Calculation of the adiabatic angular distribution at* $B = 0$ T *for a collimation factor* $f = 1.85$ *(dotted line) and without collimation* $f = 1$ *(dashed line). The solid line shows a simulation for a conical potential. Adapted from Ref. [81].*

From the geometry it can be understood that at a cyclotron radius of

$$l_{\mathrm{cycl}} = \frac{L}{2\alpha_{\mathrm{max}}} \tag{3.21}$$

the transmission probability T_d is reduced to zero, assuming that $W_{\mathrm{max}} << L$ and its maximum should be observed at $B = 0$ T. While the total signal height is given by Eq. 3.19, the total width in magnetic field may be described as

$$\Delta B = \frac{4\hbar k_\mathrm{F}}{eL} \arcsin \frac{1}{f}, \tag{3.22}$$

which is again linked to the collimation factor. In view of spin optic experiments the collimation factor is an important measure to characterize the injection quality of a quantum point contact.

3.3. Realization of QPCs in HgTe quantum well structures

The following section explains the differences and challenges of the realization of QPCs in HgTe/HgCdTe heterostructures compared to other material systems. The basic lithography concept is shown, while lithography developments will be explained in detail in Chapter 4. Measurements in various configurations are discussed.

3.3.1. Concept

One reason that it is not trivial to realize QPCs in HgTe/HgCdTe heterostructures is that the material exhibits the properties of a topological insulator. Since the formation of the QSH edge channels is bound to be at the sample edge, an easy definition via split gate technology is not possible. This is illustrated in Fig. 3.7. Even without the conducting edge channels, because of the narrow bulk band gap, impurities and an inhomogeneous gate influence can lead to a mixture of n-conducting, p-conducting or insulating areas making it difficult to rule out parallel conductance under the split gates. This effect should be more pronounced for samples with smaller band gaps. The band gap is mainly depending on the substrate material and the quantum well width. Figure 3.8 shows the direct and indirect band gap for undoped CdTe and CdZnTe (001) substrates as a function of quantum well width. The lattice constant a is given in the graph. From the crossing point of E1 and H1 (refer to Fig. 2.5) the direct band gap increases while the indirect band gap continuously decreases. At a critical well width of 7.2 nm the effective band gap is then dominated by the indirect band gap. It should be noted that the maximum effective energy gap is approximately 12 meV for CdTe substrates and 20 meV for CdZnTe.
As demonstrated for the devices in Refs. [14, 31], QPCs in HgTe QWs have to be physically etched, which can be challenging for structures in the order of only a few tens to hundred nanometer. As a consequence this leads to a fixed QPC width that cannot be altered during the measurement. As already mentioned, the observation of clear quantization steps is strongly depending on the correct length to width ratio. Therefore, size variations of the order of a few nanometer can already make a large difference in the measurement. Another drawback of a physical definition is the rather poor adiabaticity compared to electrostatically defined constrictions. As described in Ref. [83] this can

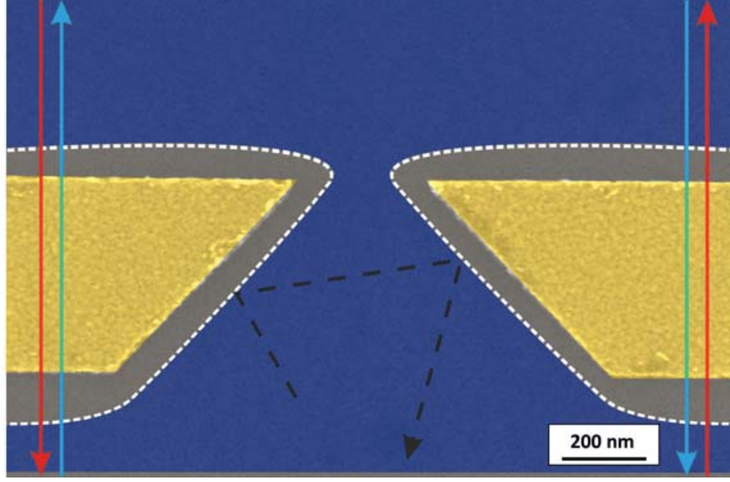

Figure 3.7.: *Colored SEM micrograph of a typical GaAs/AlGaAs split gate QPC structure. White dashed lines schematically indicate the potential formed around the yellow gate electrodes. Blue areas indicate the 2DEG area, grey areas depict depleted regions. Electrons cannot pass this barrier except for tunneling and will therefore be reflected (dashed black line). QSH edge channels (marked in red an blue) however, are bound to the physical sample edge and are not influenced by the gate as they continue to exist in the band gap.*

have a significant influence on the quality of the observed quantization steps. For this reason we developed a combination of low energy and low temperature optical- and electron beam lithography to guarantee the necessary precision and flexibility and to prevent material damage. The QPC layout for the electron beam lithography was adapted to produce smooth round shaped structures.
In order to control the mode transmission through the point contact a topgate electrode has to be introduced. Instead of changing the constriction width, the topgate influences the electron density n

$$k_{\mathrm{F}} = \sqrt{2\pi n} \tag{3.23}$$

and by that the Fermiwavelength λ_{F}

$$\lambda_{\mathrm{F}} = \frac{2\pi}{k_{\mathrm{F}}}, \tag{3.24}$$

which determines the number of occupied modes in the constriction. An example of a final structure can be seen in Fig. 3.9. The fixed constriction width w in this example

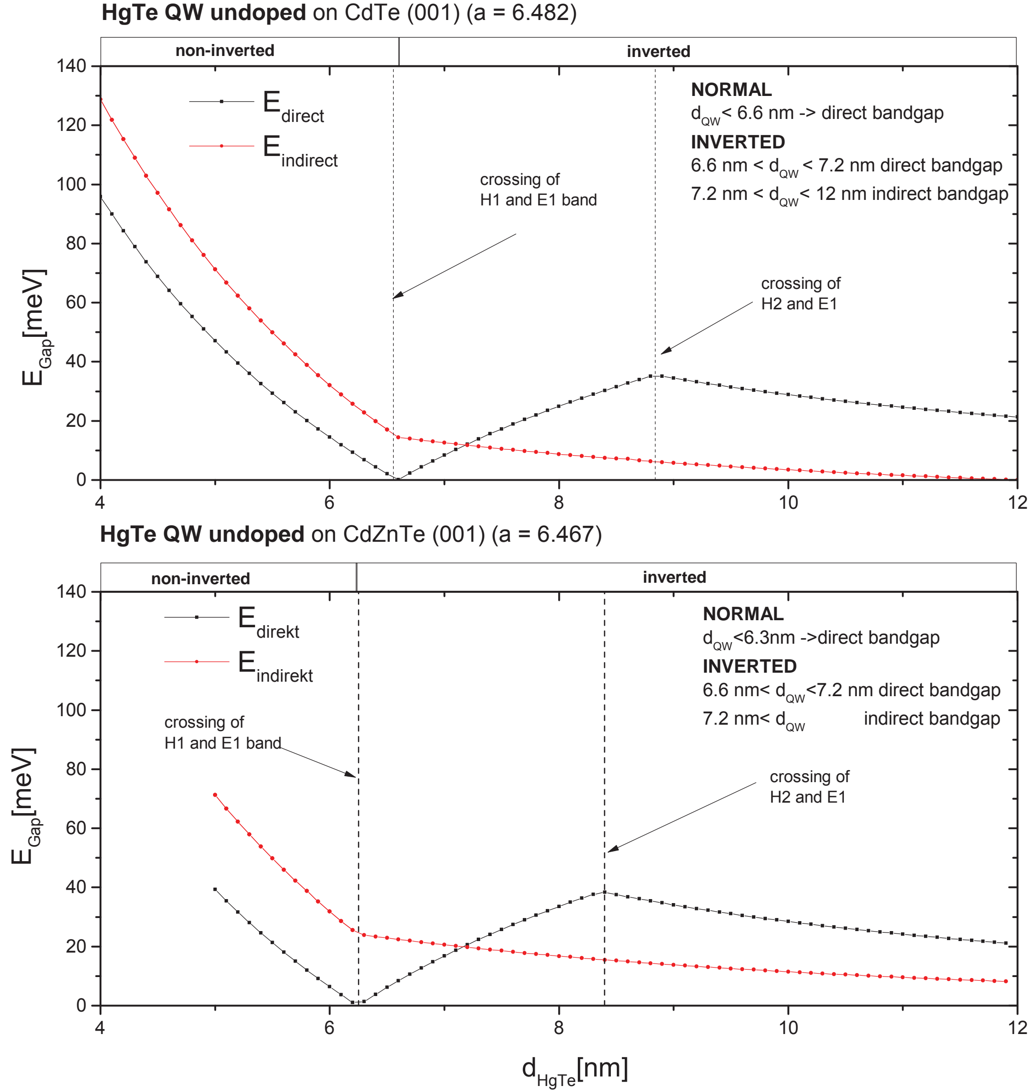

Figure 3.8.: *Direct and indirect band gap for undoped CdTe and CdZnTe (001) substrates as a function of quantum well width* d_{HgTe}.

is nominally 200 nm while the QPC length l is 80 nm. Blue marked regions indicate the mesa area with the underlying 2DEG. The actual one dimensional constriction is covered with a 500 nm wide topgate marked in yellow. Mesa and gate are separated by a 30 nm thick insulating multilayer consisting of SiO_2 and Si_3N_4. The rather grainy surface structure originates from SiO_2 clusters formed during the PE-CVD growth at 80°C and not from the MBE grown heterostructure. Our experiments show that pure Si_3N_4 grown at the same temperature produces smooth layers, but unfortunately

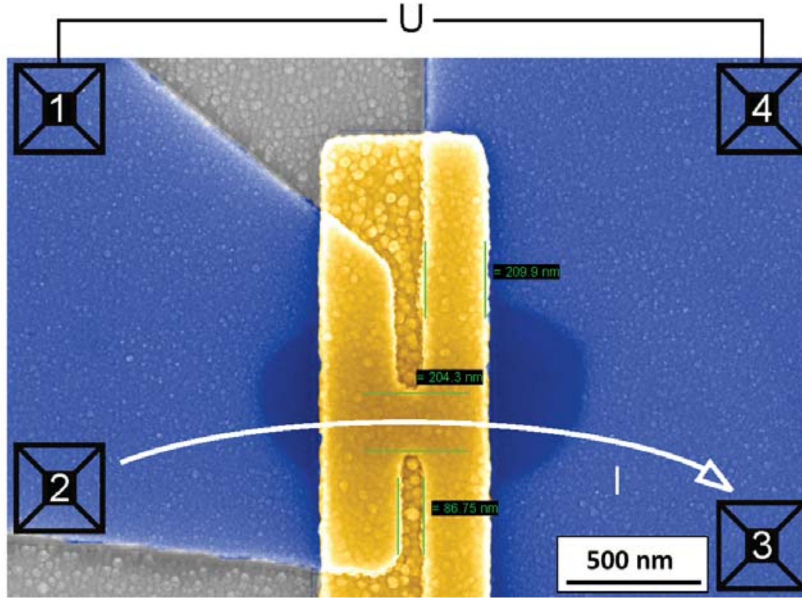

Figure 3.9.: *Colored SEM micrograph of a typical etched HgTe/HgCdTe QPC with a width of* 200 nm *and a length of* 80 nm*. For better illustration the 2DEG area is marked in blue and the topgate electrode is colored in yellow. Both are separated by a* 30 nm *insulating SiO_2/Si_3N_4 lattice grown in a PE-CVD process. The grainy structure on the surface has its origin in the low growth temperature of the insulator at 80°C. The typical four-terminal measurement configuration is illustrated schematically. Current is passed from terminal 2 to 3 while the voltage drop over the constriction is monitored between terminal 1 and 4.*

exhibits a reduced adhesion. To achieve a smooth insulating SiO_2 layer with PE-CVD, higher temperatures - usually 200°C or above - are required. This temperature range, however, cannot be applied to HgTe/HgCdTe heterostructures because it would lead to a rapid degradation of 2DEG quality. This issue and possible solutions are discussed in detail in Chapter 4.

3.3.2. Conductance measurements

AC measurements were conducted at a frequency of 13 Hz with an excitation voltage of 100 μV using standard lock-in techniques and known reference resistors. DC measurements were performed using state of the art nanovoltmeter and an excitation voltage of 1 mV. Unless stated otherwise all presented measurements were performed in ^{4}He-bath cryostats in a temperature range between 1.8 K and 4.2 K, equipped with a 1K-pot and a 10 T magnet. Conductance measurements were performed in a four

terminal configuration as illustrated in Fig. 3.9 without applied magnetic field. As shown, current is passed from terminal 2 to terminal 3, while the voltage is probed between terminals 1 and 4. The separation of current path and voltage probes reduces the influence of the unavoidable serial resistance from the mesa and the leads to the QPC to a minimum, which is depending on the specific circuit design and material properties.
Figure 3.10 shows the point contact resistance of a 195 nm wide constriction formed by two etched circles with a radius of 500 nm as a function of gate voltage. A 1.5 μm wide topgate centered over the QPC was used to control the mode transmission. The wafer Q2386 exhibits an electron mobility of $\mu = 297000$ cm^2/Vs and an electron density of $n_{0V} = 2.98 \times 10^{11} cm^{-2}$. Further material details are listed in the appendix. The solid lines in the resistance curve indicate the theoretical conductance plateaus shifted by an offset of 1.3 kΩ to account for the remaining serial resistance. Note the good agreement with plateaus observed in the measurement. The step-like behavior becomes more visible in the conductance plot shown in the lower part of the graph. As expected the conductance gradually declines with increased gate voltage in steps of 2e^2/h. It should be noted that the resistance approaches 12.9 kΩ, which is an indication of the remaining QSH edge channels in this measurement configuration. A slight hysteresis effect is observed between the two measurements, indicating charging at the interface between insulator and semiconductor as observed by Hinz *et al.* [8]. The measurement displays a constant noise level, which is more apparent in the conductance plot for higher conductance values, leading to a stronger scattering of data points. Deviations of ideal plateau values could be explained with an inhomogeneous potential landscape within the constriction as described in Ref. [83]. Figure 3.11 shows a four-terminal DC measurement of another etched constriction. The QPC width was increased to 280 nm formed by two circles with the radius reduced to 250 nm and a 1 μm wide topgate. The excitation voltage in this measurement was set to 10 mV to improve the measurement signal. All signals were measured using nanovoltmeter and 1:1 pre-amplifiers with an input impedance of 1 TΩ. As in the previous measurement the solid black lines in the resistance plot indicate the theoretical conductance plateaus shifted by a constant offset to take the serial resistance of the device geometry into account. The offset for this sample was determined to 500 Ω. Within the displayed voltage range both resistance and conductance plot exhibit distinct plateaus. The conductance decreases with applied gate voltage in steps of 2e^2/h. Comparing the measurements of Fig. 3.10

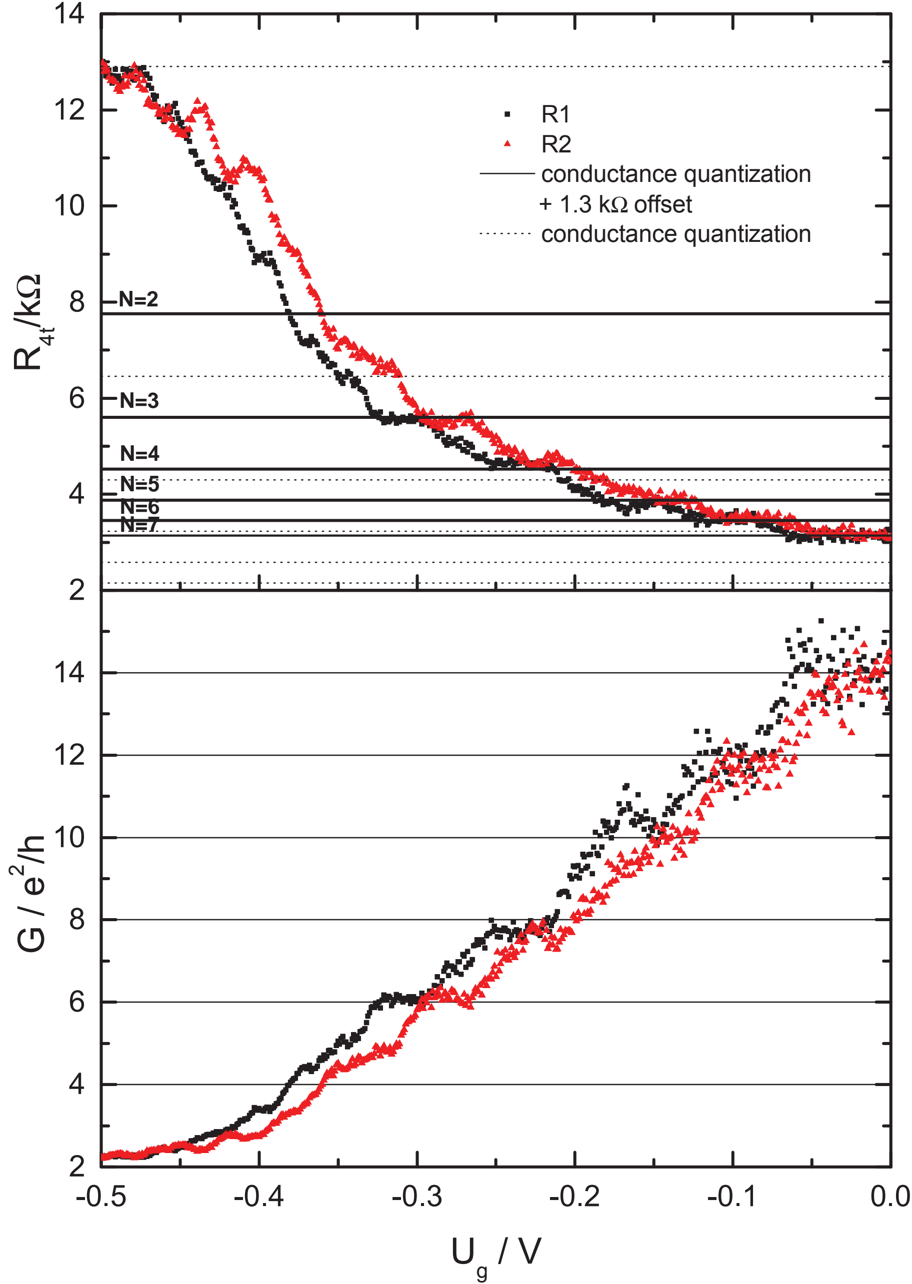

Figure 3.10.: QPC-01: *AC four-terminal resistance measurements of an etched QPC, varying the applied topgate voltage form* 0 V *to* −0.5 V *(red triangles) and back (black squares). The measurement was performed at* 4.2 K*. Dashed lines indicate the expected theoretical quantization values. Solid lines indicate the quantization values shifted by an offset of* 1.3 kΩ *to demonstrate the good agreement with steps appearing in the measurement, especially for higher mode occupation numbers N. The lower graph shows the conductance plot including the offset of* 1.3 kΩ*. Note that the resistance value approaches* $2e^2/h$ *for* −0.5 V*, which is an indication of the remaining QSH edge channels.*

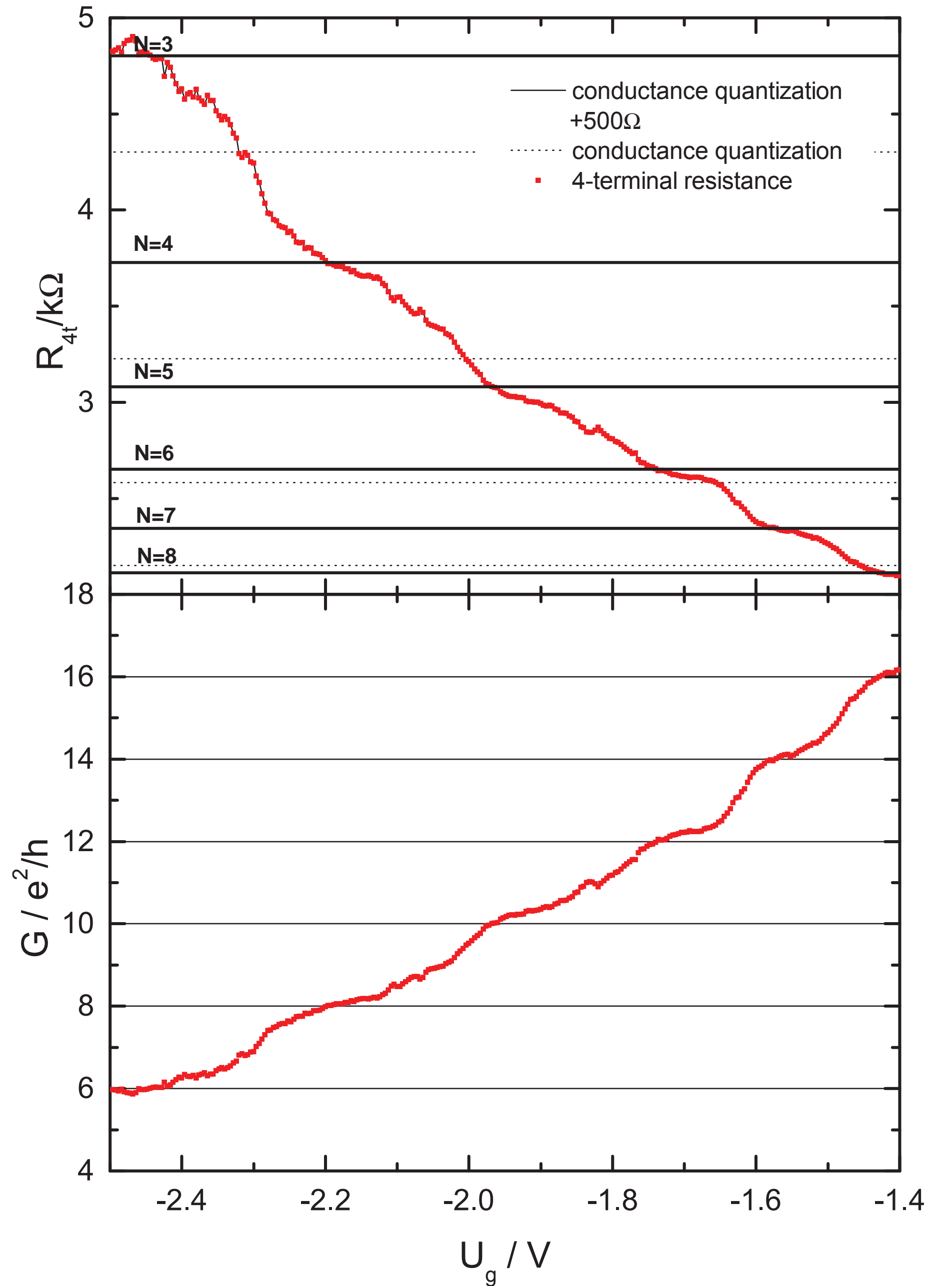

Figure 3.11.: QPC-02: *Four-terminal DC resistance measurement of an etched QPC, as a function of topgate voltage from* -1.4 V *to* -2.5 V*. The measurement was conducted at* 4.2 K*. Dashed lines indicate the theoretical quantization values. Solid lines indicate quantization values shifted by an offset of* 500 Ω *to demonstrate the good agreement with steps appearing in the measurement. The lower graph shows the same measurements as conductance plot including the offset. Note the decrease in conductance in steps of* $2e^2/h$ *as expected from theory.*

to Fig. 3.11 the DC measurement appears to be much smoother. The wafer Q2382 exhibits an electron mobility of $\mu = 229000$ cm^2/Vs and an electron density at 0 V of $n_{0V} = 3.10 \times 10^{11}$ cm^{-2}, which is comparable to the previous device.

Discussion

The main reason for deviations of the measurement from ideal quantized conductance steps is most likely scattering from potential fluctuations within the constriction. A theoretical study conducted by Nixon *et al.* in 1991 suggests ionized donors as origin for these fluctuations [83]. Although the calculations were performed for split-gated GaAs/AlGaAs point contacts, the model can be transferred to etched QPCs. The dimensions of their modeled constrictions are comparable to those of our etched structures. Their calculated conductance plots show, that scattering within the constriction is amplified in longer QPCs ($l = 0.6$ µm) compared to shorter constrictions ($l = 0.2$ µm). This can even lead to a total breakdown of conductance quantization. This is in good agreement with our observation as the shorter QPC-02 (Fig. 3.11) produces smoother conductance plateaus compared to the longer QPC-01 (Fig. 3.10). It should be noted that the quality of conductance steps is not depending on the bulk mean free path, which is approximately the same for both QPCs. Reducing the QPC length further to avoid multiple scattering, however, will increase the probability of mode tunneling through the constriction, which again leads to observed fluctuations on the conductance. Therefore in order to observe ideal quantization steps, the point contact dimensions have to match the material properties and the adiabaticity has to be maintained. Fluctuations in HgTe/HgCdTe heterostructures can either originate from growth defects, irregularities at the constriction walls or trapped states between the insulator and semiconductor surface, which can be linked to a poor insulator growth. The 2DEG used for QPC-01 is capped by only 15 nm HgCdTe, thus being more vulnerable to potential surface effects compared to the 84 nm layer of QPC-02. Unfortunately these charging effects can have a permanent influence on the sample, making it necessary to thermal cycle the device. The rearrangement of charge traps during a gate sweep strongly influences the sample behavior and can lead to a different resistance signature. Similar behavior was described by Ref. [79]. Irregularities at the sample walls generated during the dry etching process will additionally influence the measurement quality. Topinka *et al.* [84] made the observation that induced potentials in the QPC area can lead to deviations of ideal quantization values. The inhomogeneous potential

landscape and its influence in HgTe was also observed in scanning gate measurements of similar 2DEGs by König *et al.* [85]. These observations motivate the search for alternative insulator materials and growth methods as well as novel gating methods such as backgates or airbridges. Nevertheless our measurements demonstrate the feasibility of etched QPCs in HgTe QWs, which exhibit conductance quantization in steps of $2e^2/h$ and can be controlled over a large conductance range with a topgate electrode.

3.3.3. Collimation measurements

In order to utilize QPCs as injectors and detectors for spin polarized currents, we conducted four-terminal magnetoresistance measurements in a generalized longitudinal geometry to directly determine the collimation factor f of our point contacts as proposed in Ref. [86]. For this purpose two etched QPCs were arranged in series, one serving as the electron injecting device the other as the detector.
For these ballistic electron transport experiments we estimated the electron mean free path l_{mfp} for the samples to ensure that our QPC setup is within the ballistic limit. In order to obtain the Fermi wave vector k_{F} of the 2DEG, macroscopic Hall bar structures (200 µm × 600 µm) were fabricated on a separate chip from inverted material using purely optical lithography. Measurements were performed in a ^{4}He-Bath-cryostat equipped with a 5 T magnet at 4 K. An exemplary result for wafer Q2190 is shown in Fig. 3.12. From the Hall slope at $B = 1$ T we are able to calculate the electron density n using the relation

$$n = \frac{B}{R_{\mathrm{xy}} \cdot e} \tag{3.25}$$

and obtain $n_{0\mathrm{V}} = 1.36 \times 10^{12}\ \mathrm{cm}^{-2}$. In addition, the electron mobility μ of approximately 338000 $\mathrm{cm}^2/\mathrm{Vs}$ can be extracted from the known sample dimensions and the longitudinal resistance R_{xx} at $B = 0$ T using the following equations

$$\rho_{\mathrm{xx}} = \frac{1}{ne\mu} \qquad \text{and} \qquad \mathrm{R}_{\mathrm{xx}} = \rho_{\mathrm{xx}} \frac{\mathrm{l}}{\mathrm{b}}. \tag{3.26}$$

From the parabolic band approximation it is possible to estimate the corresponding electron mean free path

$$l_{\mathrm{mfp}} = \frac{h\mu}{e}\sqrt{\frac{n}{2\pi}} \tag{3.27}$$

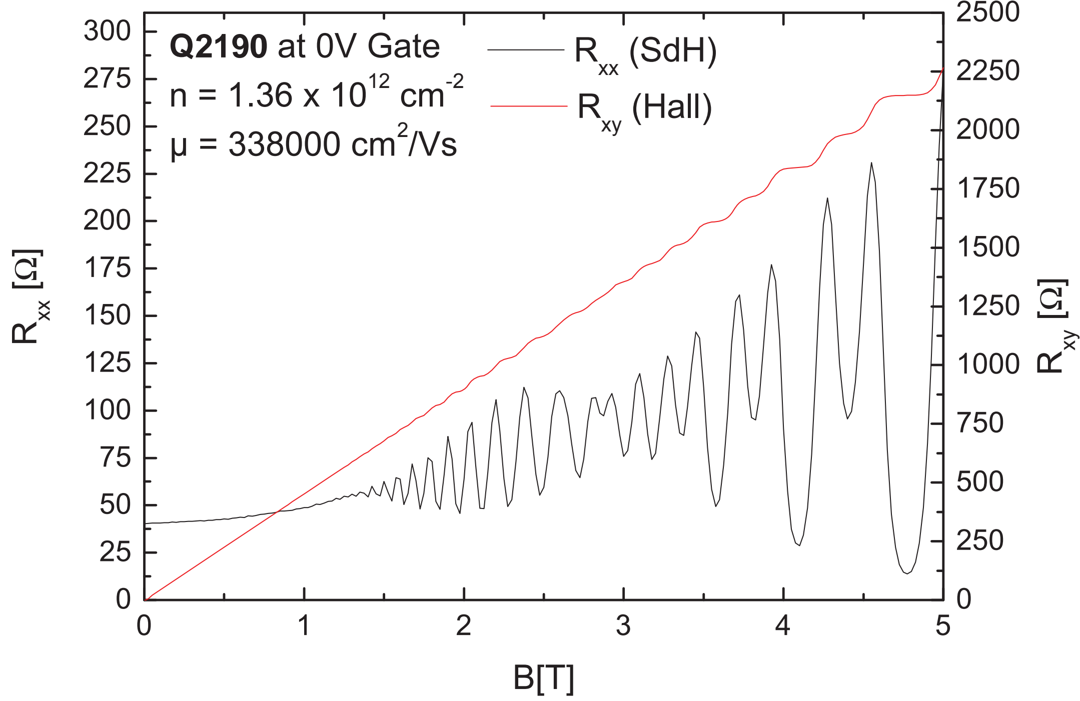

Figure 3.12.: *Hall resistance R_{xy} (red) and longitudinal resistance R_{xx} (black) of a macroscopic Hall bar at $T = 4$ K as a function of magnetic field B.*

resulting in $l_{\mathrm{mfp}} \approx 6.5$ µm for this particular material. These measurements and calculations were conducted for all used materials and the distance between the QPCs was kept well below the electron mean free path.

Using wet-chemically etched cross structures of different sizes, successful quasi-ballistic transport has already been demonstrated for HgTe/HgCdTe inverted 2DEGs by Daumer *et al.* [87]. The measurement is shown in Fig. 3.13 a). Figure 3.13 b) shows a non-local resistance measurement of a dry etched double QPC structure as a function of magnetic field B between -0.9 T and 0.9 T. The QPC width of both constrictions is $W_{\mathrm{min}} = 290$ nm, and their distance is $l = 930$ nm. The measurement was performed at 4.2 K without any applied gate voltage. A clear collimation peak is observed at $B = 0$ T while the signal continuously decreases for non-zero field, as expected from the adiabatic theory. The signal drops to zero as the beam is deflected away from the

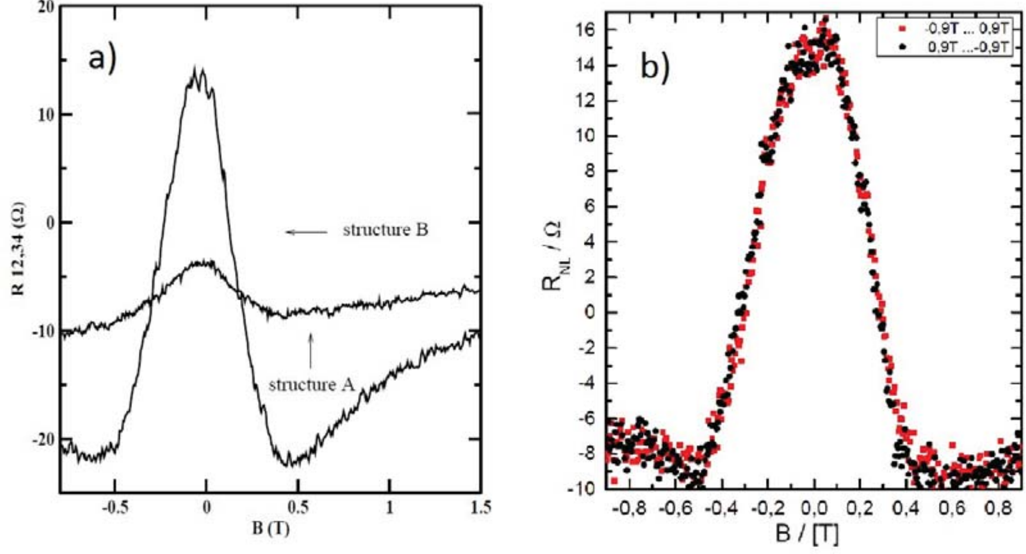

***Figure 3.13.:** **a)** Non-local resistance (NLR) signal for structures with lead widths of* 1.0 µm *(structure A) and* 0.45 µm *(structure B), adapted from Ref. [87].* ***b)** For comparison the NLR of two identical dry etched* 290 nm *wide ungated QPCs, separated by a distance of* 930 nm.

collecting QPC. This happens when

$$\frac{2r_{\mathrm{cycl}}}{l} = f \tag{3.28}$$

with the cyclotron radius

$$r_{\mathrm{cycl}} \equiv \frac{\hbar k_{\mathrm{F}}}{eB}. \tag{3.29}$$

These measurements demonstrate that dry etched quantum point contacts exhibit a collimation signal, which is in good agreement with measurements conducted on wet etched cross structures by Ref. [87].

Note that in both measurements, displayed in Fig. 3.13 a) and b), the signal shows negative resistance values for higher magnetic fields. As demonstrated in Ref. [88] this can be explained by applying the Landauer Büttiker formalism to this geometry. In a four-terminal measurement configuration one finds the following expression for the non-local resistance signal [88]

$$R_{\mathrm{nl,4t}} = \frac{V_{\mathrm{c}}}{V_{\mathrm{i}}} = \frac{h}{2e^2} \frac{T^2 - t_{\mathrm{r}} t_{\mathrm{l}}}{(t_{\mathrm{r}} + t_{\mathrm{l}})\left(2T^2 + 2\left(t_{\mathrm{r}} + t_{\mathrm{l}}\right)T + {t_{\mathrm{r}}}^2 + {t_{\mathrm{l}}}^2\right)}. \tag{3.30}$$

There t_r, t_l and T are the transmission coefficients to the right, left and opposite channel seen from the injector. From this equation it is clear that negative signals are only observed, if the product $t_\mathrm{r} \cdot t_\mathrm{l}$ exceeds T^2, meaning that the transmission to the side channels is greater than the transmission into the collector. This can be observed as the magnetic field increases and the electrons are guided along the walls. For very large values of B the signal will then rise to zero again. In a three terminal configuration the measured signal stays positive, as can be seen from the adapted equation from Ref. [88]

$$R_{\mathrm{nl,3t}} = \frac{V_\mathrm{c}}{V_\mathrm{i}} = \frac{h}{2e^2} \frac{T}{(t_\mathrm{r} + t_\mathrm{l})\,(2T + t_\mathrm{r} + t_\mathrm{l})}. \tag{3.31}$$

In the next step we want to demonstrate the controllability of the electron transmission $T_{\mathrm{i}\to\mathrm{c}}$ from injector to collector using a topgate electrode. Figure 3.14 displays the non-local resistance measurement of a second device of the same material as a function of external magnetic field. Both QPCs have a width of $W_\mathrm{min} = 290$ nm and are separated by a channel of $l = 930$ nm. Additionally both point contacts are equipped with a topgate to control their transmission. The left graph displays measurements with QPC A as injector and QPC B as detector, the right graph shows measurements for the reversed configuration. Applying a negative gate voltage of -2 V to QPC A noticeably increases the height of the observed collimation peak compared to the ungated signal. A further increase of the applied negative gate voltage for QPC A (not displayed in the graph), however, did not lead to a higher signal, indicating that no additional mode selection took place. This behavior is attributed to the charging effects at the interface between the insulator and the semiconductor [8], as already mentioned in the context of conductance quantization measurements. The accumulated charge screens the 2DEG from further gate influence. Similar measurements conducted on QPC B for 0 V and -9.75 V are displayed in the right graph. As observed in the previous measurement the gated signal is increased, suggesting an improved electron collimation. In order to quantify the quality of the point contact collimation, we calculated the collimation factors f from Eq. 3.20 as demonstrated in Ref. [81]. All necessary parameters are directly accessible from the experiment. The QPC width W_min and channel length l were obtained from SEM measurements on a reference structure. The non-local resistance of QPC A at magnetic field $B = 0$ T shows a peak height for $U_\mathrm{g} = 0$ V of $R_{\mathrm{nl,0V}} \approx 30\ \Omega$ and $R_{\mathrm{nl,-2V}} \approx 45\ \Omega$ for $U_\mathrm{g} = -2$ V, measured relatively to the background. The approximate peak height for QPC B for $U_\mathrm{g} = 0$ V

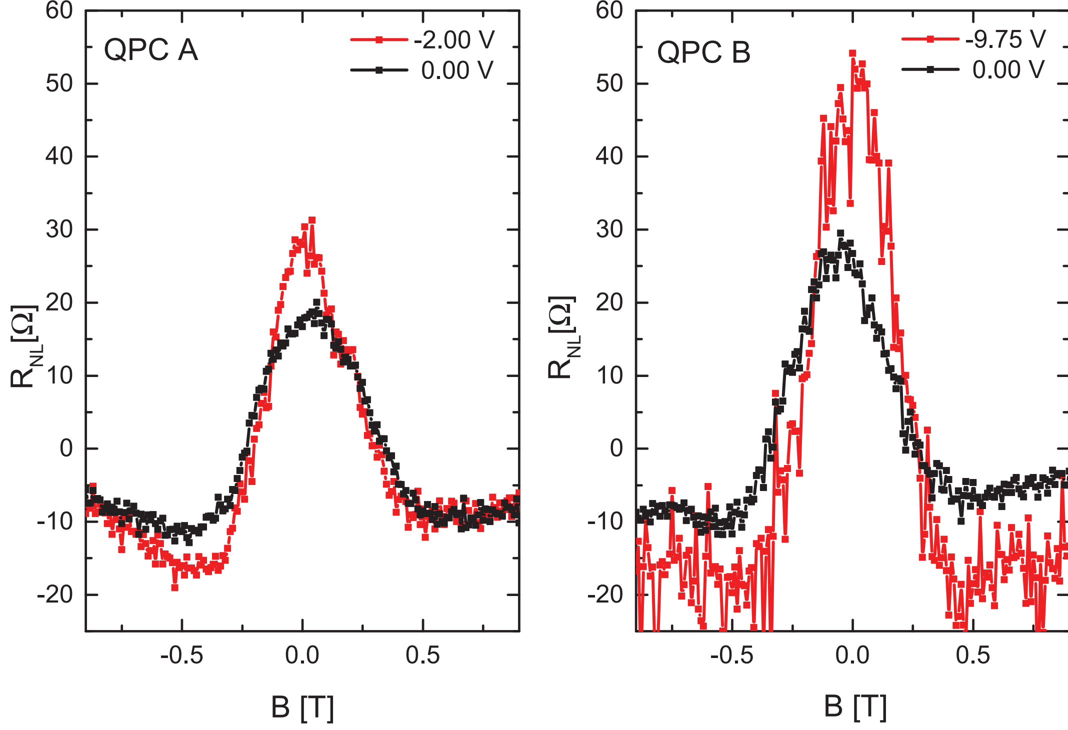

Figure 3.14.: *Non-local resistance measurement (collimation signal) of two* 290 nm *wide QPCs in a distance of* 930 nm *for different topgate voltages of QPC A and B as a function of applied external magnetic field B.*

is $R_{\mathrm{nl,0V}} \approx 38\ \Omega$ and $R_{\mathrm{nl,-9.75V}} \approx 71\ \Omega$ for $U_{\mathrm{g}} = -9.75$ V. Assuming that the electron density determined from the macroscopic Hall bar matches the density between the two QPCs, the collimation factors can be estimated as $f_{\mathrm{A,0V}} \approx\ 0.95$, $f_{\mathrm{A,-2V}} \approx\ 1.05$, $f_{\mathrm{B,0V}} \approx\ 1.00$ and $f_{\mathrm{B,-9.75V}} \approx\ 1.21$.

As the collimation factor is defined as $f\ \geq\ 1$ there has to be an error in at least one of our assumptions. One possible explanation could be an increase in electron density compared to the value determined from the macroscopic Hall bar structure. Note that in the Hall bar structure the electron density can be varied as a function of gate voltage between $n_{\mathrm{0V}} = 1.39 \times 10^{12}\ \mathrm{cm}^{-2}$ and $n_{\mathrm{-2V}} = 1.15 \times 10^{12}\ \mathrm{cm}^{-2}$ and the mobility changes from $\mu_{\mathrm{0V}} = 338000\ \mathrm{cm}^2/\mathrm{Vs}$ to about $\mu_{-2V} = 225000\ \mathrm{cm}^2/\mathrm{Vs}$. From the four-terminal resistance of the ungated injector we can recalculate the number of

transmitted electron modes N within the QPC

$$N = \frac{h}{2e^2 \cdot R_{4t}}. \tag{3.32}$$

With a measured resistance of $R_{4t} \approx 390\ \Omega$, the known minimum point contact width W_{min}, the relation

$$N = \frac{W_{min} \cdot k_F}{\pi} \tag{3.33}$$

and Eq. 3.23, this leads to a theoretical electron density of $n_{QPC} \approx 2.05 \times 10^{12}$ cm^{-2}, which is considerably larger than measured in the Hall bar geometry.[1] Taking this into account, the previously determined collimation factors increase to $f_{A,0V} \approx 1.00$, $f_{A,-2V} \approx 1.12$, $f_{B,0V} \approx 1.06$ and $f_{B,-9.75V} \approx 1.30$. These values indicate that the ungated structures exhibit only a very weak collimation. As the constriction geometry remains constant and the signal is enhanced with applied gate voltage, we conclude that the observed collimation in these structures is dominated by the barrier effect induced from the topgate rather than from horn collimation effects.

From these factors we can now estimate the full opening angle $\Delta\alpha \equiv 2\alpha_{max}$ of the formed electron beam. According to Eq. 3.12 we calculate $\Delta\alpha_{A,-2V} \approx 126°$ and $\Delta\alpha_{B,-9,75V} \approx 100°$. From Eqs. 3.28 and 3.29 we would expect the signal to vanish around a magnetic field B between 0.37 T for $f = 1.12$ and 0.33 T for $f = 1.30$ which is in good agreement with our observation.

The upper graph in Fig. 3.15 shows the simultaneous measurement of the four-terminal injector QPC resistance and the non-local resistance of the collector QPC at $B = 0$ T on a third device (QPC C) fabricated from a different wafer Q2226. The electron density $n_{0V} = 8.80 \times 10^{11}$ cm^{-2} and the mobility $\mu_{0V} = 363000$ cm^2/Vs were determined from a macroscopic Hall bar. Here the point contact width was increased to $W_{min} = 320$ nm and the channel lentgh was reduced to $l = 750$ nm. Although the QPC resistance does not exhibit quantization steps as a function of gate voltage, it clearly demonstrates the increase of electron collimation with increased point contact resistance, indicating the mode selection. From the maximum value of the non-local resistance R_{nl} and assuming no collimation for the ungated constriction we calculate a maximum collimation factor of $f \approx 1.65$. The lower graph in Fig. 3.15 shows the collimation factor f as a function

[1] A possible reason for the large difference in electron density could be attributed to the different lithography process for macroscopic samples and e-beam written nanostructures, which could lead to unintentional doping. See Chapter 4.

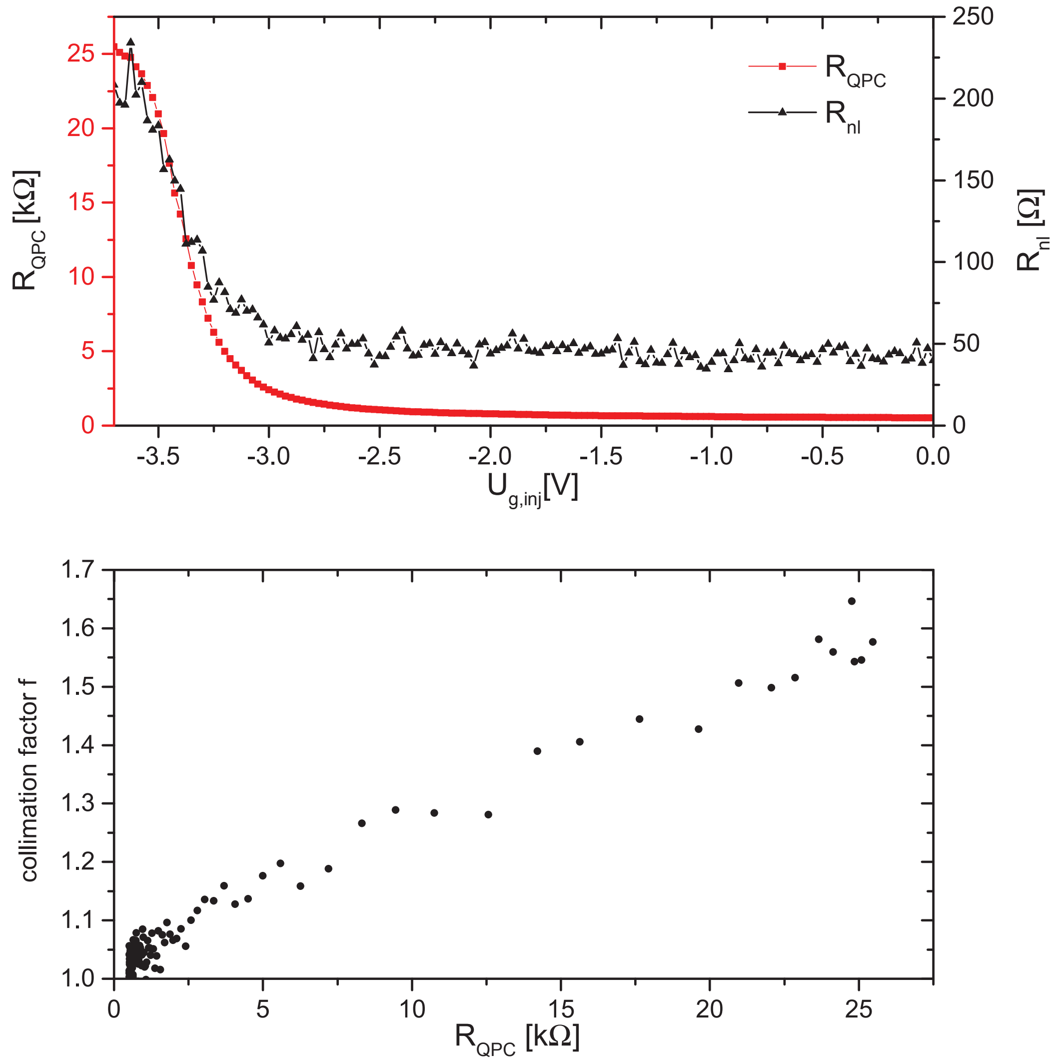

Figure 3.15.: Upper graph: *Simultaneous measurement of the four-terminal injector QPC resistance (red squares) and the non-local collimation resistance at* $B = 0$ T *(black triangles) as a function of injector gate voltage.* ***Lower graph:*** *The collimation factor* f *as a function of injector QPC resistance. A linear dependence is expected from the adiabatic theory.*

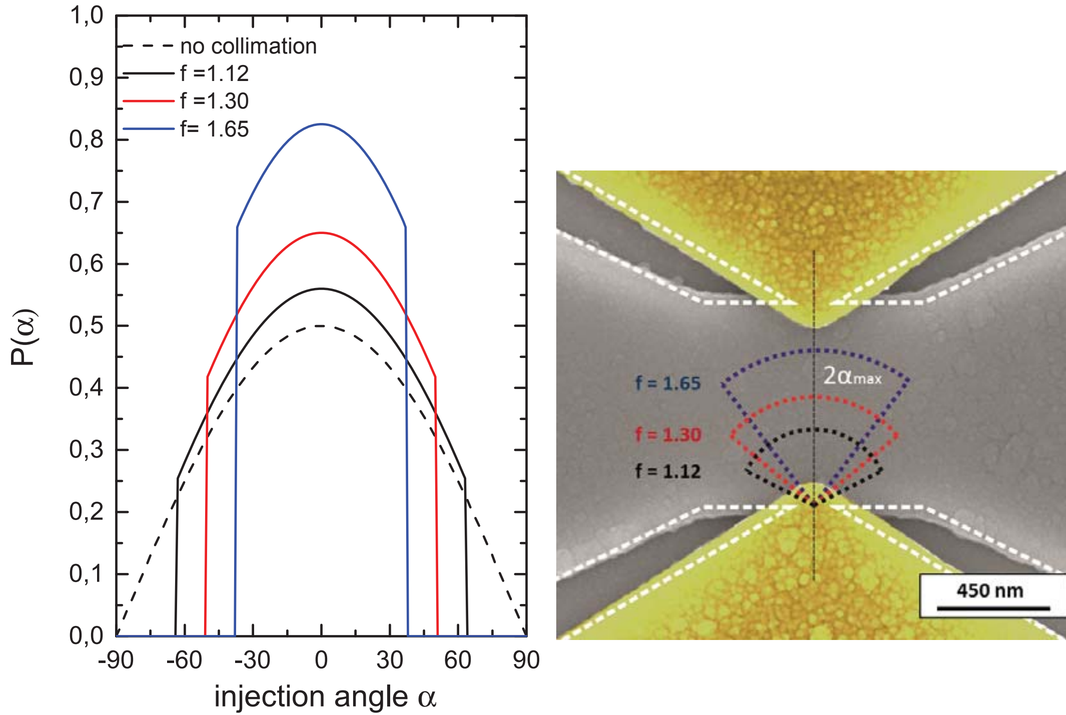

Figure 3.16.: *The angular distribution as a result of the adiabatic approximation for collimation factors $f = 1.12$ (black), $f = 1.30$ (red) and $f = 1.65$ (blue). The dashed line in the left graph indicates the distribution without collimation. The angular distribution of the transmitted electrons is schematically illustrated in a SEM micrograph of an actual structure on the right.*

of the injector QPC resistance. A linear dependence is observed, as expected from the adiabatic approximation, although the slope strongly deviates from the theoretical values. Note that for all presented collimation signals the detector QPC remained ungated. Figure 3.16 indicates the angular distribution of the injected electrons according to the adiabatic approximation from Eq. 3.16 for the different maximum collimation factors (solid lines) and in absence of collimation (dashed line). The picture shows a SEM micrograph of an actual structure with a schematic illustration of the different angular distributions of the transmitted electrons after leaving the injector QPC.

Discussion

As pointed out in Ref. [81] their observed collimation is most probably due to flaring from the potential boundaries which is the dominating effect for rather wide point contact structures ($W \geq 100$ nm). Reference [77] illustrates that the total collimation factor is a combination of the horn collimation

$$f_{\mathrm{h}} \equiv \frac{W_{\max}}{W_{\min}} \tag{3.34}$$

and the barrier collimation,

$$f_{\mathrm{b}} \equiv \left(1 - \frac{E_0}{E_{\mathrm{F}}}\right)^{-1/2} = \frac{k_{\mathrm{F}}}{k_{\mathrm{QPC}}} \tag{3.35}$$

as mentioned earlier. In contrast to Ref. [81], for the presented etched constrictions, there is practically no collimation present for the ungated QPC. This implies that the point contact only shows an inadvertent small ratio between $W_{\max}$ and $W_{\min}$ and that the observed collimation effect is mainly due to the induced barrier from the topgate electrode and does not originate from the flaring of the etched walls. This could also be an indication that the etched point contacts do not provide a sufficiently adiabatic transition. The reason could be rather rough constriction walls, having their origin in the applied dry etching technique. Multiple reflections at those wall irregularities can destroy the collimation leading to a reduced resistance signal [81]. This problem, however, could be addressed by developing a more reliable wet etching technique, making it possible to etch structures as small as 100 nm. Impurity scattering could also lead to a reduced collimation signal. The strongly increased carrier density points to unintentional doping during the fabrication process. A reason could be diffusion of the etch mask material which would also lead to local impurities or thermal stress. Thus it seems necessary to re-evaluate the fabrication process. It should be noted that the collector QPC remained ungated during the non-local resistance measurements, which could also lead to a reduced signal. Nevertheless, these measurements provide direct evidence for electron collimation in HgTe/HgCdTe QPCs and for its controllability with a topgate electrode.

3.4. Spin polarizer

Idea

Having shown that QPCs in HgTe/HgCdTe heterostructures are capable of forming collimated electron beams, and demonstrating their controllability via external gate structures, we wanted to turn to one particular proposal made by Khodas *et al.* in 2004 [89]. In their scheme, the lateral interface between two regions of different spin-orbit coupling strength is utilized to spin polarize electrons. The polarization is solely controlled by the applied gate voltage and the use of non-magnetic semiconductor materials. The spin orbit interaction can either be of the Rashba [51] type, which originates from a structural inversion asymmetry of the confinement of the 2DEG, or of the Dresselhaus type [90] which originates from the bulk inversion asymmetry, present in materials with e.g. zinc-blende structure. Both effects can be found in HgTe/HgCdTe quantum wells, but especially the Rashba spin orbit coupling can be particularly strong [8, 52, 53] while the Dresselhaus contribution can be widely neglected for narrow gap semiconductor systems [91, 92]. This approach proves particularly interesting, since the technology to inject polarized electrons into a semiconductor system has posed multiple challenges in the past [93]. Figure 3.17 a) illustrates the idea using the example of an optical polarizer. Light with both polarization directions collimated through a lens is directed onto a birefringent material in a non-zero critical incident angle θ_C. As illustrated the different polarizations are split at the polarizer interface and therefore propagate on different paths. In this illustration the in-plane polarized light is totally reflected at the interface while the out-of-plane component is refracted and transmitted. The idea of the spin polarizer follows the same principle. If an unpolarized electron beam hits the polarizer interface in a non-zero incident angle, as illustrated in Fig. 3.17 b), the electrons will also be spin polarized and propagate into different directions, comparable to the birefringent effect in classical optics where the light polarization determines the amplitudes of the refraction. Here a quantum point contact serves as a lens to generate a collimated beam of electrons. The key to realize this device is to create the polarizing interface. In contrast to the optical analog it is not necessary to introduce a different material into the beam path. Instead it is possible to locally alter the material properties by changing the Rashba SO strength with a topgate electrode.

The splitting effect can be understood by looking at the Hamiltonian with Rashba spin

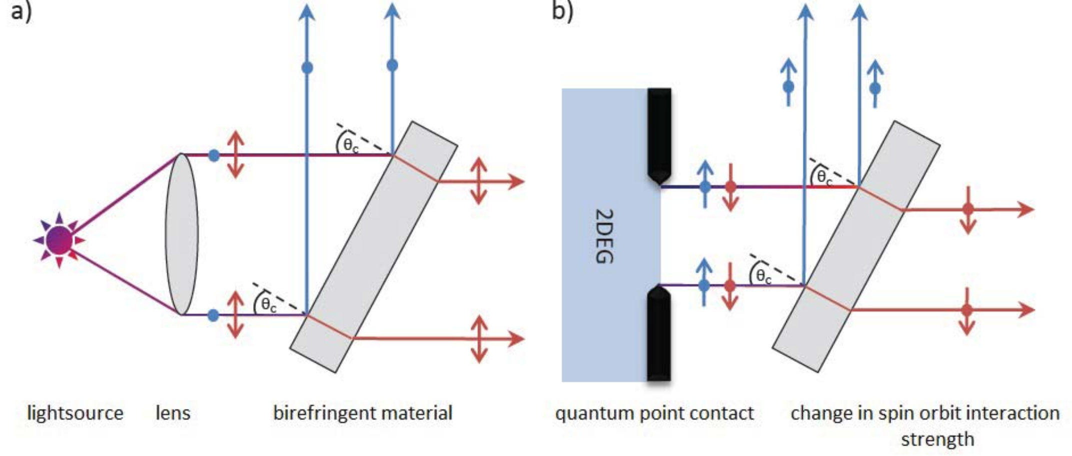

Figure 3.17.: *Schematic of an optical polarizer a) and a spin polarizer b) as proposed by Khodas et al. [89]. In classical optics the splitting of different polarization directions (in plane, red and out of plane, blue) happens at the interface of a birefringent material. Analogue the separation of electrons of different polarization (spin up, blue and spin down, red) happens at the interface between two regions of variable spin orbit interaction strength.*

orbit interaction which can be written as

$$H_R = \frac{{p_x}^2}{2m(x)} + \frac{{p_z}^2}{2m(x)} + B(x) + \frac{1}{2}(\hat{\mathbf{l}} \times \sigma)[\alpha(x)\mathbf{p} + \mathbf{p}\alpha(x)] \tag{3.36}$$

with the corresponding current operator

$$\mathbf{J} = \frac{\mathbf{p}}{m} + \alpha(x)(\hat{\mathbf{l}} \times \sigma), \tag{3.37}$$

which also contains a spin dependent part [89]. Here α denotes the SO strength, $B(x)$ is the bottom of the conduction band, $\hat{\mathbf{l}}$ is a unit operator perpendicular to the 2DEG plane, σ the Pauli matrices, $\mathbf{p}$ the electron wave vector and m the effective electron mass. The continuity conditions for the wave function also involve the spin degrees of freedom for scattering at the interface between regions of varying SO strength α [89]. From that one can calculate the dispersion relations for electrons of different chirality

$$E^{\pm} = \frac{p^2}{2m} \pm \alpha p + B, \qquad \nu = \frac{\partial E^{\pm}}{\partial p} = \frac{p}{m} \pm \alpha \tag{3.38}$$

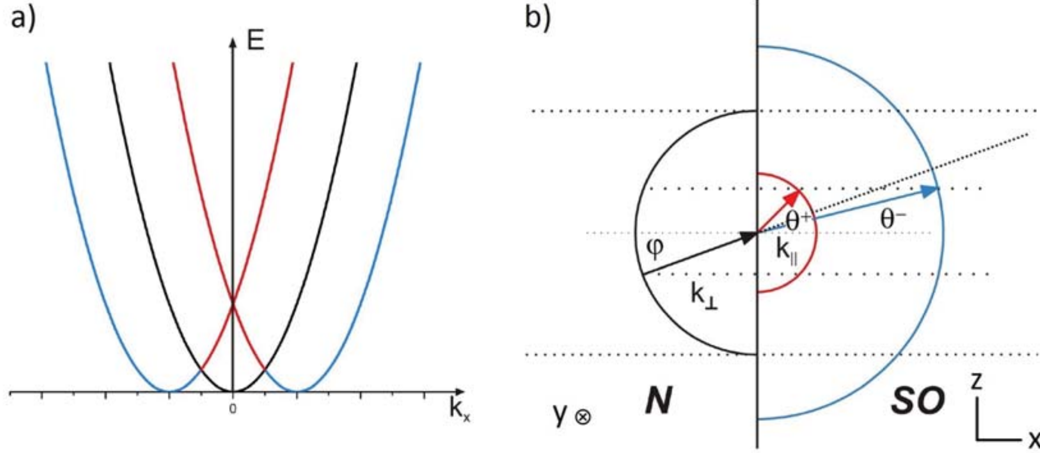

Figure 3.18.: *a) Schematic illustration of the dispersion relation with (red and blue) and without (black) Rashba spin orbit coupling. b) Topview of the dispersion relation in the k_x and k_z plane at the Fermi surface. The momentum of the incoming beam from a region without spin orbit coupling "N" (black) parallel to the scattering interface is conserved while the perpendicular momentum changes depending on the chirality of the electrons (red and blue) in a region with spin orbit interaction "SO".*

and their momenta,

$$p^{\pm} = m(\sqrt{2(E-B)/m + \alpha^2} \mp \alpha. \tag{3.39}$$

The conservation of the projection of the momentum ($k_{||}$) at the scattering interface together with Eq. 3.39 determines the propagation directions of the reflected and transmitted electron beams [89]. The effect is illustrated in Fig. 3.18. Figure 3.18 a) schematically shows the different dispersion relations from the side, while Fig. 3.18 b) illustrates the top view at a given Fermi energy and the spatial separation of the incident wave at the interface. The region with SO coupling is optically more dense for the (-)-modes and less dense for the (+)-modes. This can even lead to a total reflection of the (+)-modes in an interval $\varphi^c < \varphi < \pi/2$, where φ^c is the critical angle. Vice versa the (-)-modes have a limited aperture in the SO region where in an interval of $\pi/2 > \theta > \theta^c$ only the (+)-modes can penetrate the interface [89]. Therefore a potentially promising regime for a spin filtration lies in an interval $\varphi^f < \varphi < \varphi^c$ since there is no overlap between modes of different chirality. The (+)-mode scatters into the interval $\theta^s < \theta < \pi/2$ while the (-)-mode propagates in the interval $\theta^f < \theta < \theta^s$, as illustrated for a constant α in Fig. 3.19. The full theory and additional details can be found in Ref. [89].

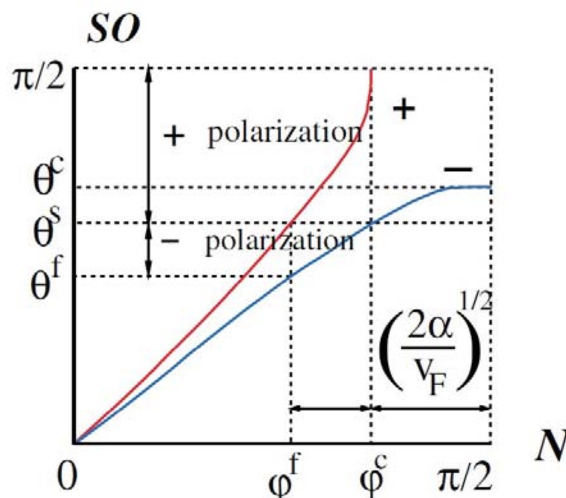

Figure 3.19.: *The angle of refraction for the two polarization modes as a function of the angle of incidence. φ^c is the angle for total internal reflection for (+)-mode. θ^c determines the aperture for (-)-mode. θ^s defines the angle of separation between modes of different chirality. Other angles are related to the spin filtration and are explained in the text. With $\alpha = 0.1$ and B(x) = const. From Ref. [89].*

Experiment

In an actual device, the SO interaction strength can either be adjusted by asymmetric doping of the quantum well or by applying a gate voltage over the specific area. The latter is the method of choice as it allows the dynamic control of the spin orbit coupling strength over a defined zone and can therefore act as a spin switch. For a first experiment we chose a material with an asymmetrically bottom doped QW structure. This leads to a homogenous intrinsic Rashba spin orbit coupling over the whole device. Hinz *et al.* [8] demonstrated a change in Rashba SO spitting Δ_R of approximately 15 meV in a voltage range between −2 V and +2.4 V on comparable material with a 12 nm QW. In order to induce a region without spin orbit coupling, a thin gate stripe was fabricated diagonally between the electron source and the detector. The gate was separated from the heterostructure by a 110 nm SiO_2/Si_3N_4 layer serving as an insulator. Applying a negative voltage at the splitter gate increases the asymmetry and leads to an even larger SO interaction, while a positive voltage leads to a more symmetric setup and diminishes the observed Rashba SO splitting. The applicable gate voltage range is mainly limited by the observed hysteresis effects originating from charge accumulation at the insulator semiconductor interface. The overall change in Rashba SO

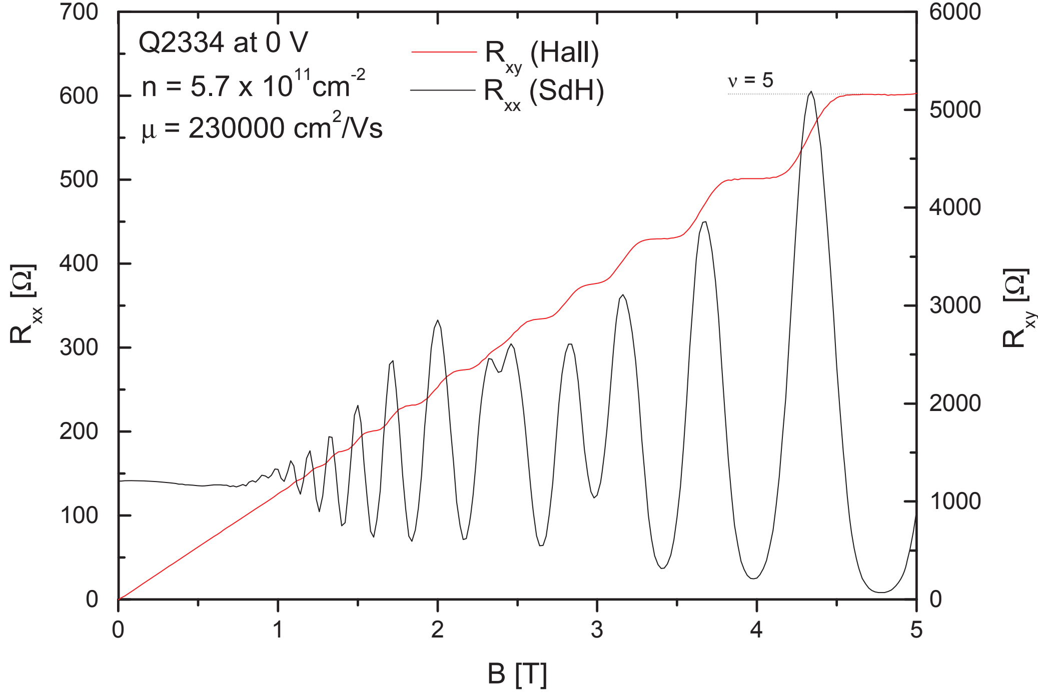

Figure 3.20.: *Hall resistance R_{xy} (red) and longitudinal (SdH) resistance R_{xx} (black) of a macroscopic Hall bar at $T = 4$ K as a function of magnetic field B.*

splitting therefore is determined by a combination of intrinsic bandstructure [52] and gate control [8].

A change in gate voltage also leads to a change in electron density in the QW. Figure 3.20 shows the Hall resistance R_{xy} and the Shubnikov de Haas (SdH) oscillations R_{xx} of a macroscopic Hall bar as a function of magnetic field B at $T = 4$ K and $U = 0$ V. The heterostructure has an inverted 8 nm QW and a top barrier of only 15 nm in order to further improve the influence of the topgate. The observable beating in the SdH trace is a sign for the Rashba SO splitting present in the material. The corresponding electron mean free path calculated from the determined carrier density n and the mobility μ, together with Eq. 3.27 gives roughly $l_{\mathrm{mfp}} = 2.86$ μm. Figure 3.21 displays additional SdH measurements of the same device. Note that the observable beating of the oscillations at $U = 0$ V gradually diminishes as the gate voltage is increased to larger positive values until it is barely visible at $U = +2.0$ V. The disappearing of the beating pattern indicates the decreasing Rashba SO splitting. Thus it is

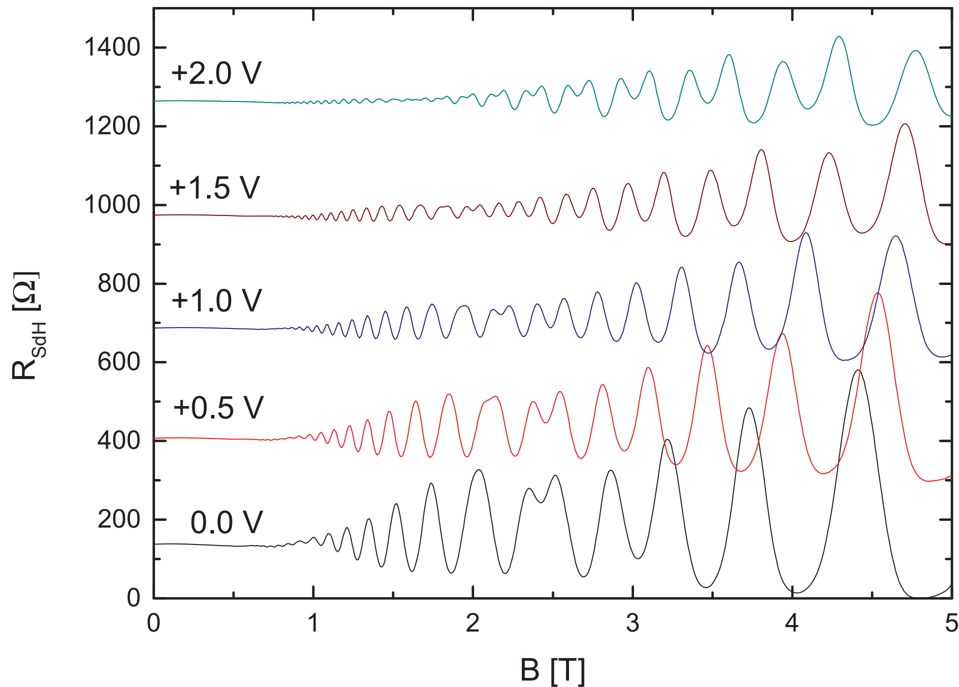

Figure 3.21.: *Shubnikov de Haas (SdH) oscillations at* $T = 4$ K *as a function of magnetic field* B *at increasing positive gate voltages. Note that the observable beating at* $U = 0$ V *gradually diminishes with increased gate voltage. For clarity the traces are displayed with a constant offset of* $300\ \Omega$*.*

possible to introduce a region without SO coupling (N) within the defined gated area, realizing the SO-N-SO setup as proposed by Ref. [89].

The injection of an unpolarized, collimated electron beam is realized by an etched QPC similar to the structures discussed in Chapter 3.3. A second QPC in a distance of 1 μm, well below l_{mfp}, serves as a detector. The whole setup is visible in the colored SEM picture in Fig. 3.22. The mesa is marked in blue, gates are marked in yellow, etched parts are displayed in grey. As lithographic reasons limit the number of gatestructures, only the injector QPC at the bottom of the image is equipped with a topgate. The injected electrons are supposed to enter the channel and scatter at the diagonal interface between areas of different SO coupling strength. The splitter gate has a width of approximately 170 nm and the angle of incidence for the electrons is roughly 45°. The splitter gate spans the complete channel width to make sure all electrons have to pass

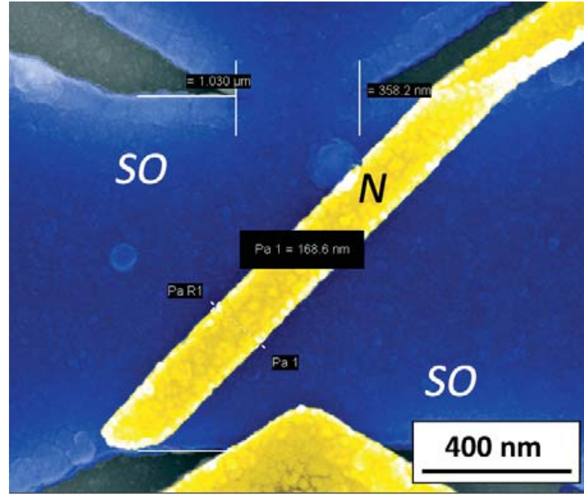

Figure 3.22.: *Colored SEM micrograph. The 2DEG is marked in blue, gates are marked in yellow. Two QPCs are separated by a thin gate stripe. The ungated areas exhibit spin orbit coupling (SO) while in the gated area the spin orbit coupling can be adjusted to larger, or smaller values (N).*

the interface. Ideally only one spin direction is able to pass the splitter while the other is totally reflected. The design presented in Fig. 3.22 allows to measure charge accumulation in different terminals, however, it does not allow to probe for different spin states. Figure 3.23 shows a series of non-local resistance measurements as a function of magnetic field. The observed collimation signal shows a strong asymmetry at a splitter voltage of 0 V and a shift of its maximum to negative B-field values. Note that already the mere presence of the gate without any applied voltage does have an influence on the underlying potential landscape. Increasing the splitter voltage to positive values up to 3 V leads to a stronger and more symmetric collimation signal. An increase to positive gate voltages is equal to a decrease in Rashba SO interaction as depicted in Fig. 3.21. At the same time this will lead to an increase in electron density, better screening of scattering centers and a longer electron mean free path, thus leading to an improved transmission to the detecting QPC. The observed asymmetry could be an indication of electron selection at the splitter interface, although the spin state of the transmitted electrons cannot be verified with this setup. Continuously decreasing the splitter voltage down to -1.4 V as shown in Fig. 3.24 leads to a strong drop of the observed collimation signal. Negative voltages increase the Rashba SO interaction in the gated region. However, the simultaneous decrease in electron density will also lead to a potential barrier. This in turn will lead to a momentum selection of the

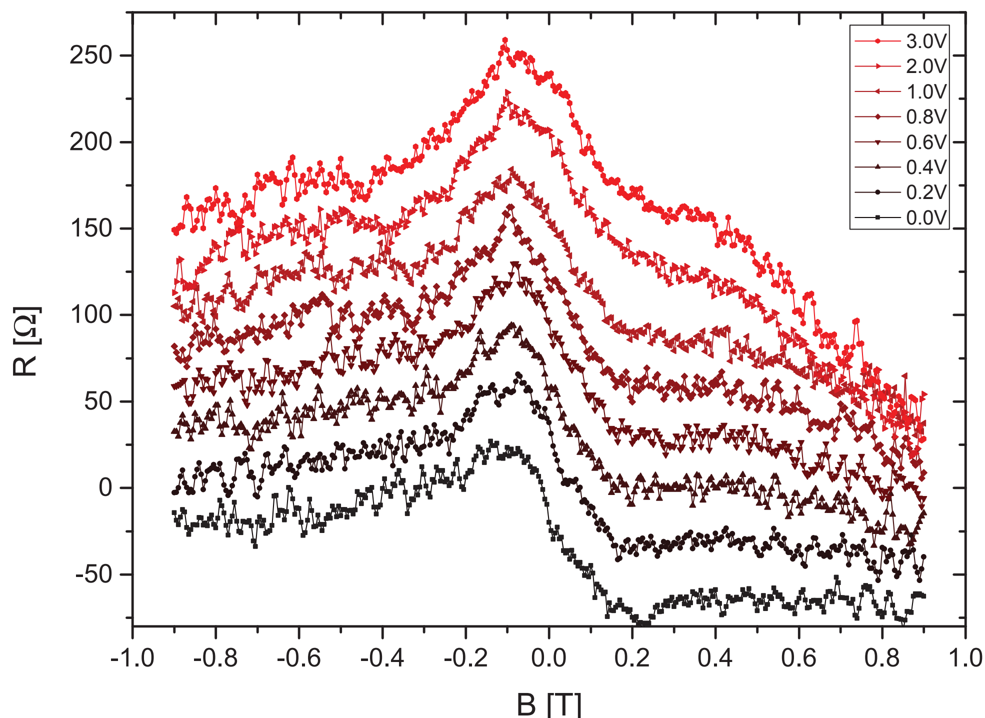

Figure 3.23.: *Non-local resistance measured as a function of magnetic field B and different positive splitter voltages. Electrons are injected via one point contact to interfere with the splitter gate. Increasing the voltage up to $3\ \mathrm{V}$ continuously increases the detected signal at the second QPC. Measurement curves are displayed with a constant offset of $25\ \Omega$ for better visualization.*

impacting electrons, comparable to the barrier-effect within the QPC. The observed shift to negative resistance values is an indication that the product of the scattered electron signals t_l and t_r in Eq. 3.30 exceeds the transmitted signal T, even without applied magnetic field.

Independent of the Rashba SO interaction, the gated area will be either optically more or less dense, depending on the applied voltage. Either scenario will lead to a shift in the observed resistance signal, but only in the case of an optically less dense splitter region, total reflection can be observed. Snell's law of refraction does also hold for ballistic electrons and can be rewritten as

$$\frac{\sin(\theta_1)}{\sin(\theta_2)} = \sqrt{\frac{n_2}{n_1}}. \tag{3.40}$$

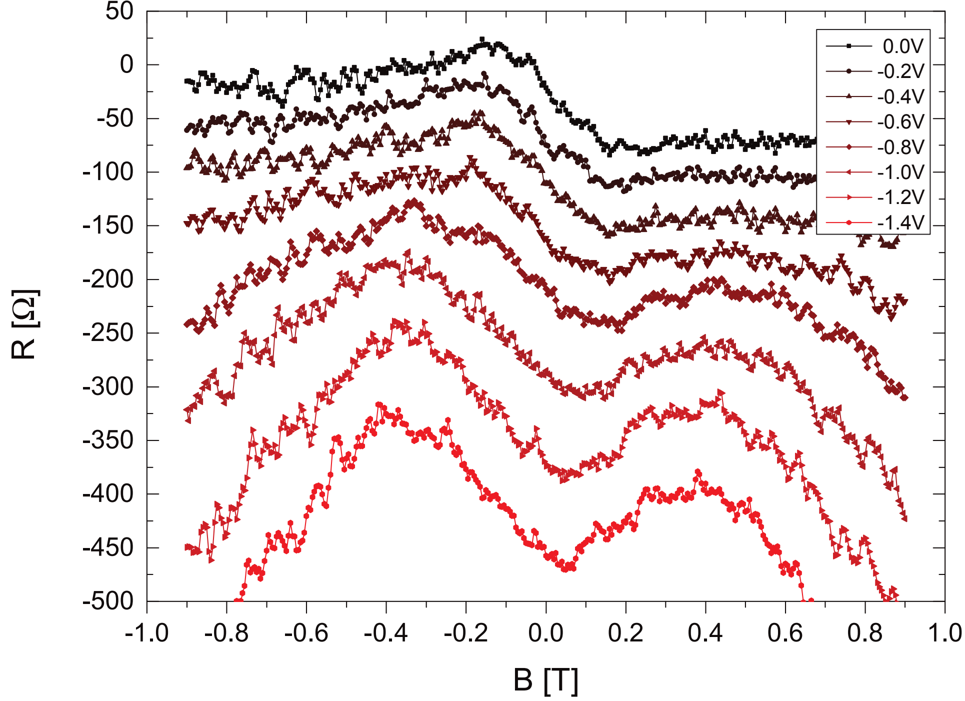

Figure 3.24.: *Non-local resistance measured as a function of magnetic field and different negative splitter gate voltage. Electrons are injected via one point contact to interfere with the splitter gate. Decreasing the splitter voltage down to* $-1.4\,\mathrm{V}$ *continuously reduces the detected signal at the second QPC. The observed drop suggests a downgrade in electron transmission because of increased scattering. Measurement curves are displayed with a constant offset of* $-25\,\Omega$ *for better visualization.*

with the two different electron densities n_1 and n_2 [94]. Electrons at the Fermi energy E_F impinge at an angle θ_1 from a region with a carrier concentration of

$$n_1 = \frac{mE_\mathrm{F}}{\pi\hbar^2}, \tag{3.41}$$

while in the splitter region the concentration is

$$n_2 = \frac{m(E_\mathrm{F} - \Phi)}{\pi\hbar^2}. \tag{3.42}$$

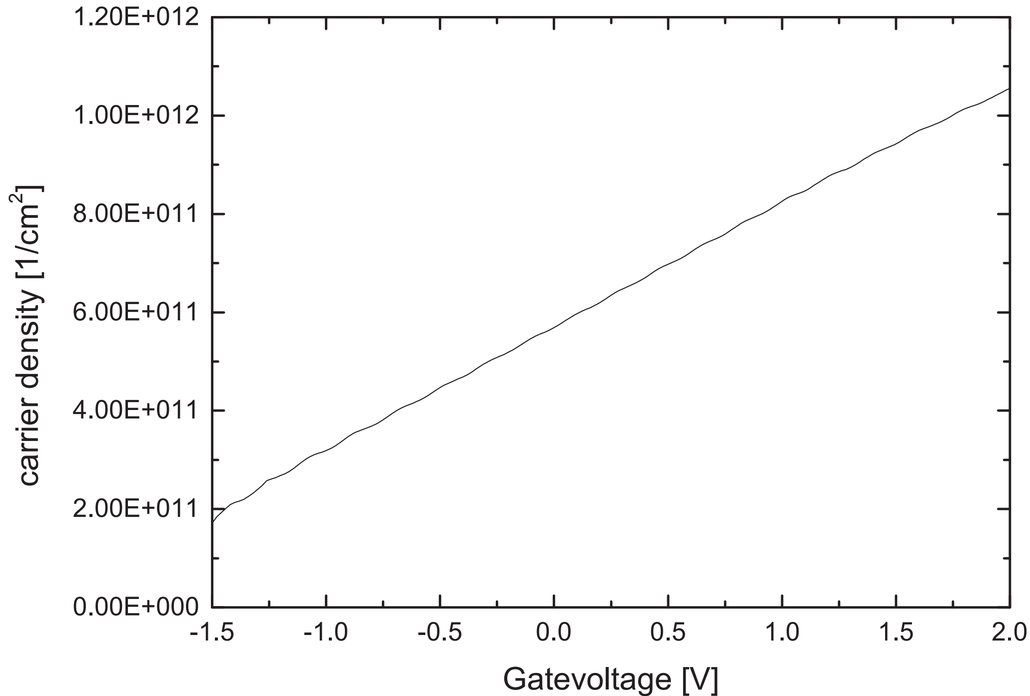

Figure 3.25.: *Calculation of the carrier density plotted against the applied gate voltage for a reference Hall bar. To obtain this graph the Hall resistance was measured at a constant magnetic field of* $B = 1$ T *in a gate voltage range between* -1.5 V *and* $+2$ V.

This consequently leads to

$$\frac{\sin(\theta_1)}{\sin(\theta_2)} = \sqrt{1 - \frac{\Phi}{E_{\mathrm{F}}}}. \tag{3.43}$$

In contrast to photons entering a medium with a larger dielectric constant, for positive values of Φ the outgoing angle of the transmitted electrons θ_2 is larger than θ_1. This originates from the different dispersion relations for photons and massive particles [95]. For electrons a lower velocity corresponds to a longer wavelength [95]. An applied negative gate voltage will lead to larger angles of θ_2 while positive voltages will lead to smaller outgoing angles. This seems consistent with our observation in Fig. 3.24, that for increasingly negative splitter voltages the transmission into the opposite point contact is drastically reduced, as electrons are totally reflected at the splitter interface. Figure 3.25 shows the carrier density versus the applied gate voltage. To obtain this graph we monitored the Hall resistance of a reference Hall bar of the same wafer at

a constant magnetic field of $B = 1$ T while changing the applied gate voltage from -1.5 V to $+2.0$ V. The electron density was calculated using Eq. 3.25. The Hall slope approximately equals the measured Hall resistance at the given magnetic field. From this measurement we conclude that for the splitter setup this voltage range allows us to change the density in the gated region by almost an order of magnitude. To give an estimate at which splitter voltage we would expect total reflection of the straight injected electrons we calculated the expected refracted angles of incoming electrons at a 45° angle as a function of carrier density n. The calculation is based on a 0 V electron density in the ungated 2DEG of $n_1 = 5.7 \cdot 10^{11}$ cm^{-2}. The result is displayed in Fig. 3.26. Total reflection will occur at densities in the splitter region smaller than $n_c = 2.85 \cdot 10^{11}$ cm^{-2}. For smaller incident angles θ_1 this critical density n_c will be consequently larger. Comparing these values to our measurement displayed in Fig. 3.25 this is equal to gate voltages of roughly -1.2 V and below. This nicely agrees with the observed dip in the measurement in Fig. 3.24 for small magnetic fields and splitter voltages below -1.0 V. The increase of the signal and the observed asymmetry for increasing values of B to either side can be explained by steeper incident angles to one side and possible rebound electron trajectories.
As already mentioned, positive splitter voltages lead to larger electron densities but also to a decrease in the Rashba SO interaction (see Fig. 3.21), thus improving the spin splitting at the SO-N interface. Within the gated region, multiple reflections are possible, thus making it difficult to interpret the signal. The observation of only one collimation peak at the detector QPC does not explicitly mean that only one spin state was transmitted. Since the splitter region is only 170 nm wide, a potential path difference originating from the discrete refraction for different spins may be small and might not be resolved in the measurement. The distance which an unrefracted electron injected at a 45° angle travels within the gated splitter region is roughly 240 nm. Even large carrier densities of $n_2 = 1.0 \cdot 10^{12}$ cm^{-2} only lead to refraction angles θ_2 of approximately 30°, that will translate into a lateral beam shift of 40 nm. In the case of imperfect total reflection, if both spin states are transmitted but refracted at different angles, the peak shift will probably be only a few nm. Based on the collimation factors calculated earlier and the corresponding injection angles a transmission of both spin states at different angles would most probably lead to a broadened collimation peak. A slight broadening of the collimation signal can be seen for increasing positive splitter voltages in Fig. 3.23.

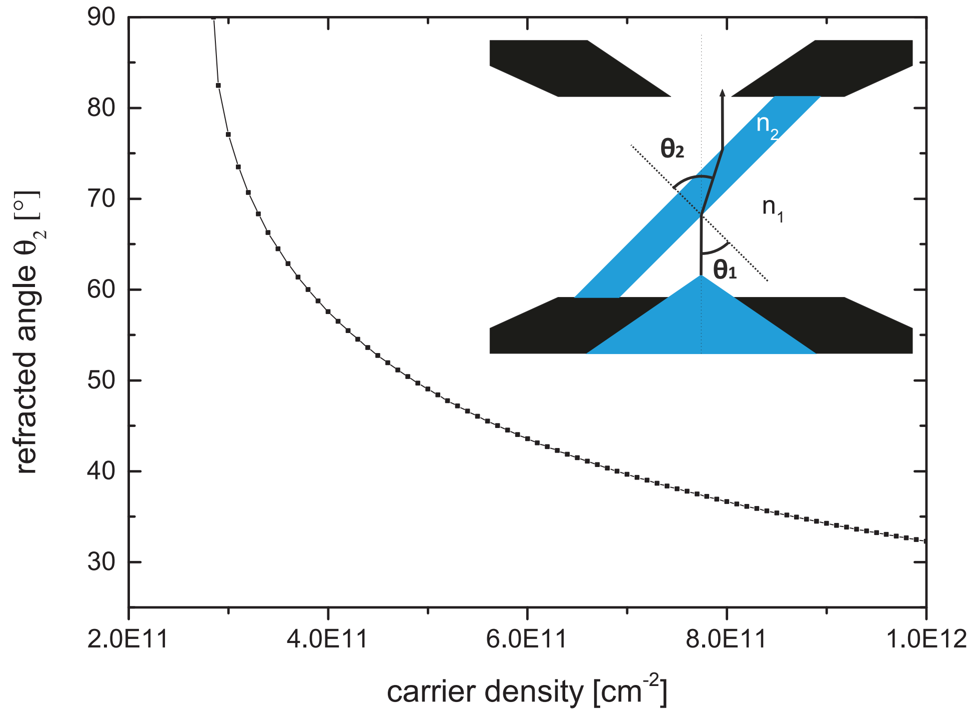

Figure 3.26.: *Calculation of refracted angles θ_2 as a function of electron density in the splitter gate region, based on a 2DEG density of $n_1 = 5.7 \cdot 10^{11}\ \mathrm{cm}^{-2}$ and an incident angle θ_1 of 45°.*

In order to clarify the observations we propose to use a different setup utilizing a prism structure instead of a gated stripe, comparable to the experiments in Ref. [96]. Thus injected electrons only have to cross one transition. In addition it should be evaluated, if the transmitted collimation signal can be probed similarly to the QSH states via the inverse SHE as demonstrated in Ref. [35]. There the spin accumulation leads to a detectable voltage difference. Another proposed detection scheme utilizes two subsequent beam splitters to fully electrically probe the spin state as described by Ref. [97]. To realize this setup, however, several improvements in lithography and 2DEG quality are necessary to provide a narrow beam and an increased electron mean free path.

To fully understand the influence of the splitter gate on the electron transmission, a multi-QPC scheme as displayed in Fig. 3.27 is useful. Electrons injected from terminal A are spin split at the interface and detected at the terminals B and C, depending

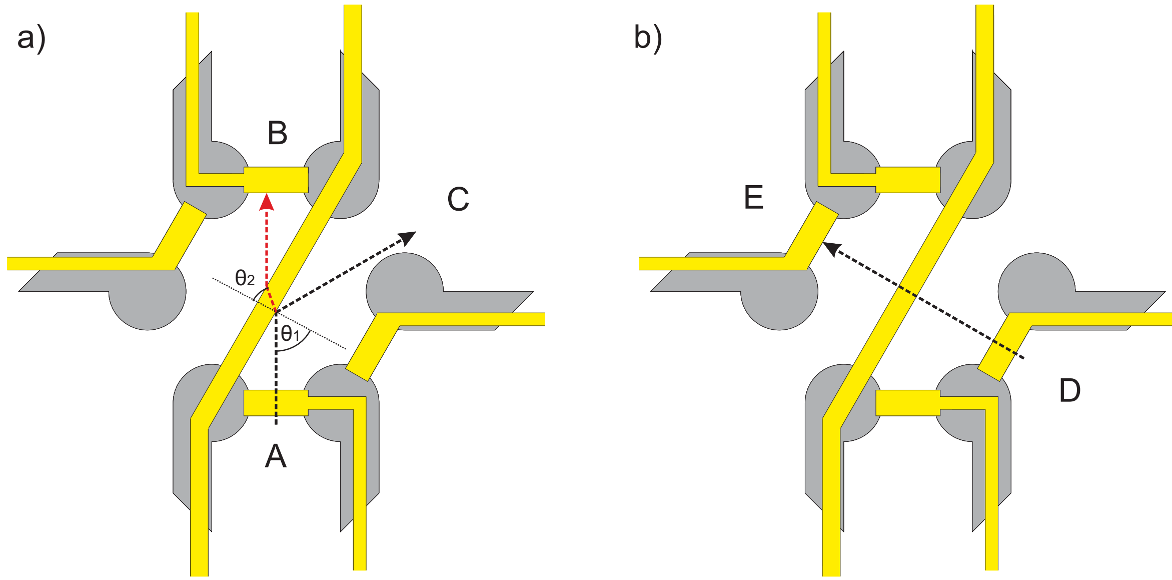

Figure 3.27.: *Schematic multi-QPC setup for two angles of incidence θ_1, 60 ° (a) and 90 ° (b). Depending on the applied splitter voltage, the detected signal will either be received in terminal B or terminal C.*

on their transmission or reflection, as schematically illustrated in Fig. 3.27 a). As displayed in Fig. 3.27 b), terminal D as injector QPC and terminal E as a detector can be used for a reference measurement as the angle of incidence is 90° and the beam will not be refracted.

Summary

Although these measurements demonstrate that electron optical experiments are possible in HgTe/HgCdTe heterostructures, we have not yet been able to realize a spin optic device as proposed in Ref. [89] in a satisfying quality. To achieve this goal, we have to further improve the electron collimation to narrow down the injection angle. Additional gate structures are necessary to allow for a more precise control of injector, detector and splitter. Smooth sample walls can reduce back scattering and enhance the transmission. In order to distinguish between classical electron optics and spin optics additional nano-structures have to be implemented. Backgating gives additional control over the Rashba SO strength in the entire sample and could help to overcome charging effects. All of these developments are rather challenging, as many lithographic techniques well established for other material systems cannot be easily adapted. Despite the long history of HgTe in the infrared detector community, high electron mobil-

ity transport experiments on nano-structures and the necessary lithography have only been evolving in the past few years.

4. Lithographical developments

Since the sample design and lithography used for the first quantum spin Hall measurements, nanolithography on HgTe based heterostructures has been under constant development and has experienced continuous improvements. This chapter will focus on some major adaptations and refinements in low temperature and low energy lithography, which are necessary for such heat sensitive material systems. The main focus will be on improvements in ohmic contacting and bonding, hard-mask lithography and the introduction of a sacrificial layer as a protective coating. The need for low temperature lithography and related problems will be explained and finally air bridges as a new gating method and its possible advantages will be presented.

4.1. Ohmic contacts, bonding and miniaturization

Motivation

In order to understand the development of the lithographic process I want to outline briefly the state of the art prior to this work. In 2007 M. König *et al.* published the first measurements of the quantum spin Hall insulator state observed in HgTe/$Hg_{0.3}Cd_{0.7}Te$ quantum well structures [14]. For their experiments they used modulation-doped molecular beam epitaxial (MBE) grown layers, on CdZnTe (001) substrates, with quantum well widths that varied between 5.5 nm and 12 nm. Although the devices were specified in length and width with values ranging between $(1.0 \times 0.5)\ \mu m^2$ for the smallest and $(600 \times 200)\ \mu m^2$ for the largest sample, these dimensions only refer to the actual Hall bar geometry. The chip itself which is also hosting leads and bond pads has dimensions in the range of $(6 \times 4)\ mm^2$. A typical macroscopic Hall bar structure as used in Ref. [14] is shown in Fig. 4.1. The miniaturization of bond pads is limited by the bonding technique. So far the standard bonding procedure for these samples relied on Au wires attached directly to the mesa using In

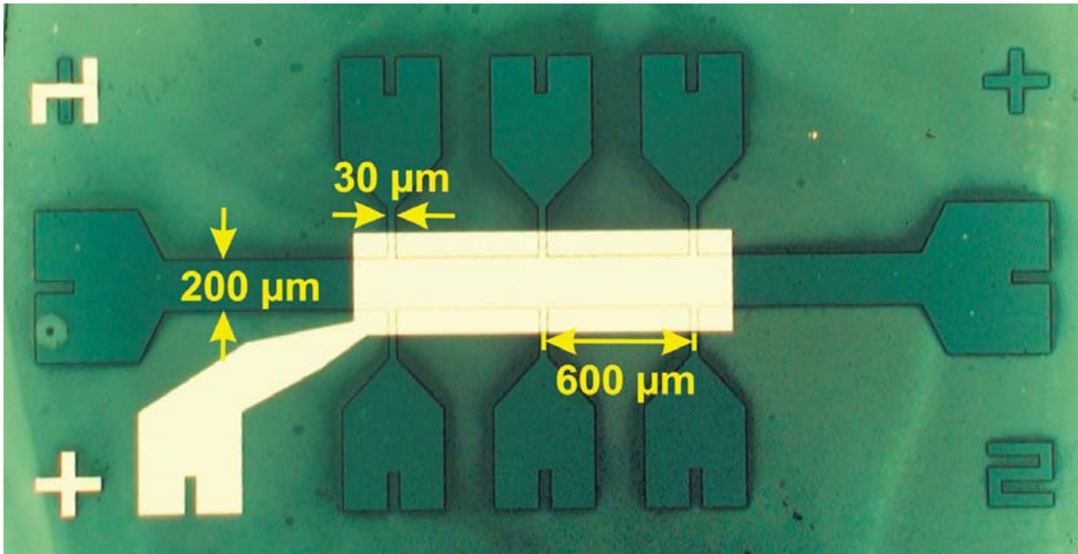

Figure 4.1.: *Optical microscope picture of a macro Hall bar structure with topgate as used by Ref. [14] prior to thermal bonding. Arrows indicate the device dimensions.*

as solder material. While this bonding technique has the advantage that it is rather easy to apply and does not require advanced lithography, there are some drawbacks that motivate the search for alternative methods.

Ohmic contacts

The quality of ohmic contacts is depending on the difference between the chemical potentials of metal and semiconductor. To achieve a low contact resistance R_c either the doping concentration at the metal-semiconductor transition has to be large, or the barrier height between them low. Therefore it is rather difficult to achieve good ohmic contacts on wide band gap semiconductors [98]. Even though HgTe/HgCdTe quantum wells exhibit a very narrow band gap of few meV, the band gap E_g of the barrier material $Hg_{0.3}Cd_{0.7}Te$ is relatively large, approximately 1 eV. For the substrate material CdZnTe this value is approximately 1.4 eV [22].
For III-V semiconductors such as GaAs with a comparable band gap E_g of 1.43 eV a variety of techniques exists to achieve good ohmics [99]. The main mechanisms that form ohmic contacts are the regrowth of alloys, ion implantation and diffusion. Usually the desired contact metal is deposited either by evaporation or sputtering. To achieve good diffusion and to get rid of adhesion problems, the evaporated metals often contain a mixture of compounds e.g. Au, Ge and Ni. After the deposition it is in general nec-

essary to add an annealing step. The annealing temperatures for common alloys range from 150 °C to 1800 °C depending on the metal-semiconductor combination [99]. Since the MBE growth temperature for HgTe quantum wells is around 180 °C at a high Hg background pressure these annealing temperatures cannot be applied without the risk of damaging the HgTe QW structure. Due to the low vapor pressure of Hg, too high temperatures lead to a loss of Hg and induce interdiffusion processes between barriers and well, both causing severe damage to the structure. Therefore the process temperature for all lithography steps should not exceed 80 °C, which has been established as a safe value for short periods of time. Quantum Hall measurements of samples tempered at 80 °C for one hour showed no sign of increased carrier densities or reduced mobilities and were identical to reference measurements before annealing.
Because of the high interest in HgTe/$Hg_{1-x}Cd_xTe$ for sensor- and optical applications there has been a lot of effort in developing proper contacts [100]. It should be noted that for HgTe Bulk material or HgTe capped layers a whole variety of metals is suitable to form ohmic contacts [100]. In our case the 2DEG is confined between two $Hg_{0.3}Cd_{0.7}Te$ barriers. Therefore we have to penetrate the cap layers to reach the quantum well. Under these aspects it is reasonable to start with a metal that has a low melting point and serves as an excellent donor. The material of choice therefore is In. An additional advantage of In is the possibility of local diffusion by the use of thermal bonding. With a needle heated to 160 °C In can be acquired from a small reservoir and locally deposited on the substrate and wire. Although this temperature considerably exceeds the safe range, it only leads to a local destruction of the 2DEG and does not affect the complete wafer. Because of the low thermal conductivity in CdTe/CdZnTe substrates, it can be assumed that for large remote bondpads the thermal stress for the device under test (DUT) can be kept at a minimum.
Despite the advantages, this method also has some major drawbacks, mainly affecting the reliability of the contacts. Indium forms a natural semiconducting oxide (In_2O_3), when exposed to air. This oxide is thermally much more stable and covers the acquired In droplet like a protective coating. Although conducting at room temperature, this oxide can cause contacts to freeze out at common temperature settings for transport experiments like 4.2 K and below. Furthermore it prevents proper adhesion of the bond and the diffusion of the metal into the semiconductor barrier. Additionally, even at room temperature In is known to form the brittle intermetallic compound $AuIn_2$ in contact with Au wires. The rapid growth of this compound is shown in Fig. 4.2,

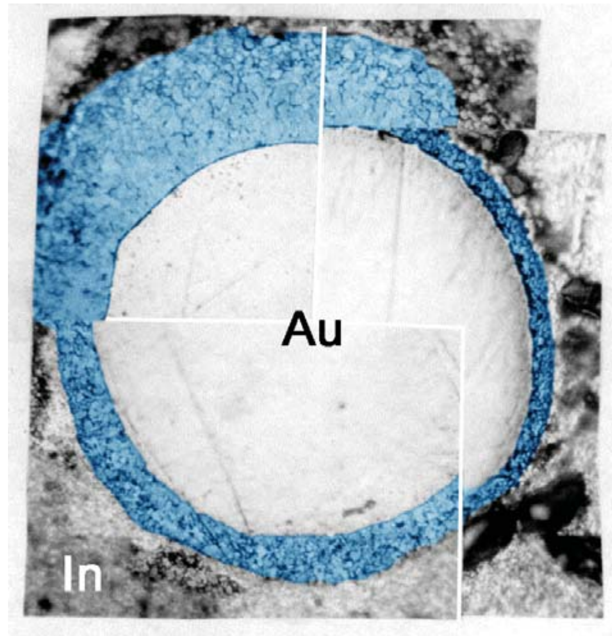

Figure 4.2.: *Composite photograph at 500x showing growth of an intermetallic compound at* 100°C *(blue). Clockwise: 72 hours, 1 to 5 o clock; 144 hours, 5 to 9 o clock; and 240 hours, 9 to 1 o clock. Adapted from Ref. [103] and colored for better visualization.*

where a 25 μm Au wire is surrounded by In and monitored at 100 °C up to 240 h. The clockwise increase of the $AuIn_2$ region (blue) with time is easily visible. Problematic for the sample reliability are the high diffusion rate of In into Au and the different thermal expansion of the neighboring metals [101]. This can cause the samples to fail after a few thermal cycles [102]. Another disadvantage poses the bonding technique itself. Usually the diameter of the soldering needle and the size of the acquired metal droplet are in the range of several 100 μm. This already limits the miniaturization of the bondpads. Because of the oxide coating, the wetting of the substrate is variable, which of course leads to variable contact sizes and quality. The different sizes and shapes of the In solder joints are visible in Fig. 4.3. Additionally one can notice bubbles appearing around the contacts. These bubbles originate from outgasing material underneath the insulating layer that covers the whole structure. This reveals the minimum range of the thermal stress for the sample due to the soldering. Although the thermal conductivity in the CdTe substrate is an order of magnitude lower than in e.g. GaAs, obviously thermal conduction through the high mobility 2DEG cannot be neglected.

Taking all these aspects into account it is reasonable to look for contacting alterna-

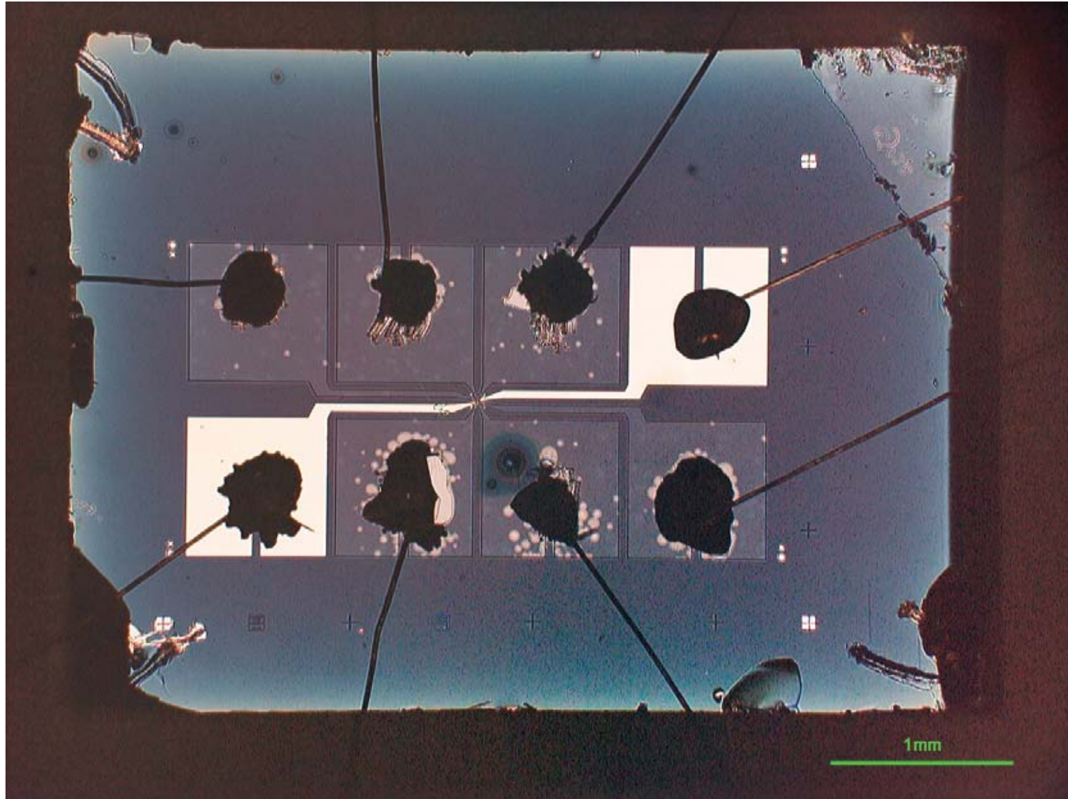

Figure 4.3.: *Optical microscope picture of a typical indium bonded chip with optical mesa and gate leads including bondpads and Au wires. The different shapes and sizes of the indium contacts (black) are visible. Bubbles appearing around the contacts are due to outgasing beneath the insulator during the In soldering.*

tives which should allow for smaller contacts that are more reproducible and more reliable. We therefore studied the possibility of combining optical lithography with electron beam physical vapour deposition (EB-PVD) of compatible metals, and a subsequent lift-off, as common for GaAs/AlGaAs 2DEGs. In our experiments we focused on establishing this technique without the need of an additional annealing step. With this method it should be possible to define contact areas down to a few microns with a high reproducibility and almost any desired shape while minimizing the heat load for the QW. The bondpads can be contacted directly using ultrasonic bonding, which significantly reduces the required pad area.

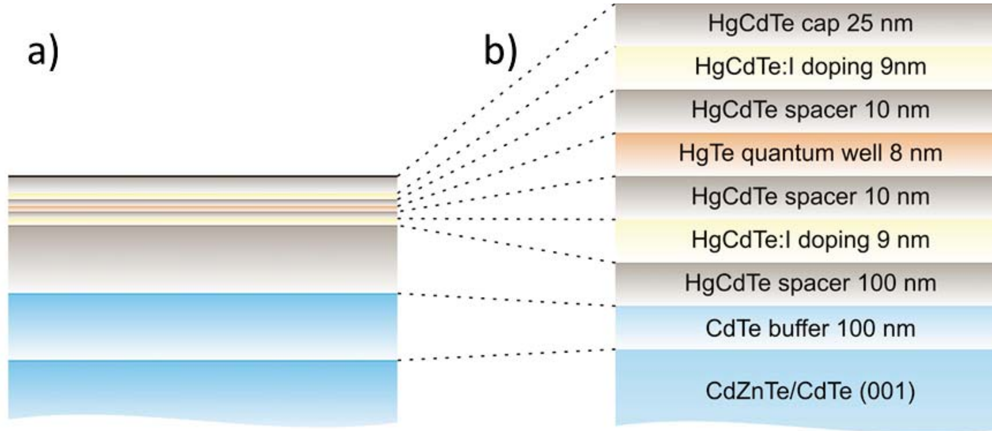

Figure 4.4.: *Schematic picture of a typical HgTe/HgCdTe heterostructure with the correct aspect ratio of all MBE layers a) and a detailed description b).*

Experiment

Although it has been proven difficult to achieve good ohmic contacts to CdTe and HgCdTe for sensor applications [104], one has to keep in mind that the aim for contacting high mobility n-conducting QWs is to penetrate the cap layer of a few (10 to 100) nm. Fig. 4.4 shows a schematic picture of a typical MBE grown heterostructure, which is comparable to the samples measured by König *et al.* [14]. Figure 4.4 a) shows the layers with a correct aspect ratio. For a better overview a detailed description is denoted in Fig. 4.4 b). In this example the metal has to diffuse at least 44 nm to contact the QW.
In order to do representative contact tests, several aspects have to be kept in mind. The overall contact resistance R is usually depending on the contact area A and the specific contact resistance R_c and thus can be denoted as

$$R = \frac{R_C}{A} \tag{4.1}$$

in a first approximation. Consequently, the evaporated area must be kept comparable for different metals. However, Eq. 4.1 does not hold for a varying current density over the area, which will be addressed in detail later. Moreover different metals tend to have different diffusion lengths. This for example can lead to higher resistance values for wafers with larger cap layers but does not necessarily exclude them as suitable contact

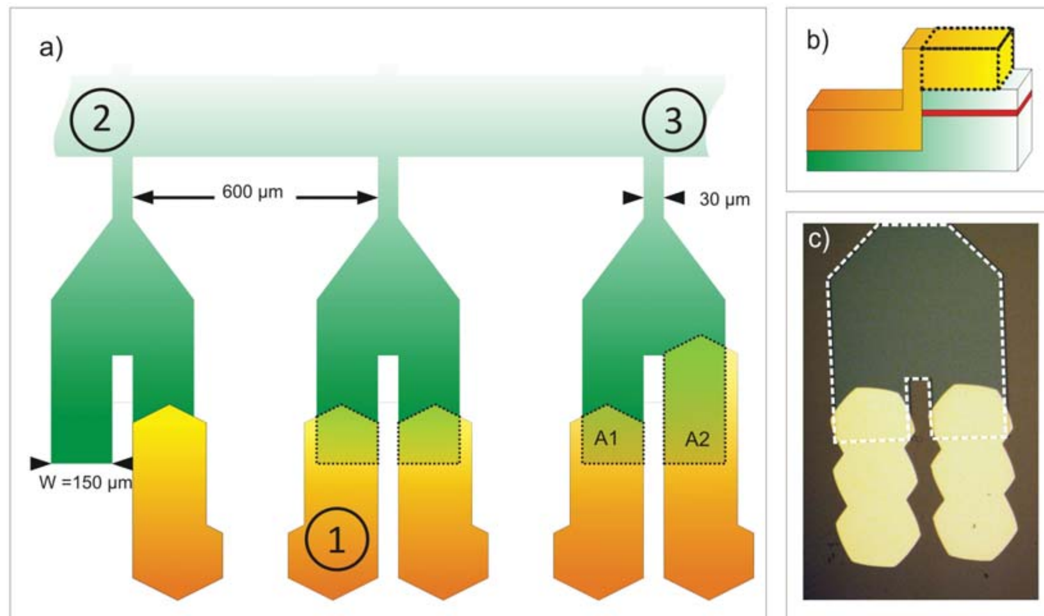

Figure 4.5.: ***a)*** *Schematic picture of a section of the test structure. Green parts indicate the dry etched mesa area, orange parts symbolize the evaporated metal and dashed lines show the actual overlap between mesa and metal, the contact area A. Different contact sizes A1 and A2 can be achieved by repeated exposure using the hexagonal aperture. Note that the contact width W is defined through the etched mesa and kept constant at* 150 µm. *The contact resistance is measured in a three terminal configuration. Current is passed from contact 1 to contact 2, while the voltage drop is measured between 1 and 3.* ***b)*** *Schematic cross section of metal and mesa. The position of the QW is indicated in red.* ***c)*** *Optical microscope picture of an actual test sample. The dashed white line indicates the mesa perimeter.*

material for shallow 2DEGs. Quite the contrary this can be essential for separately contacting the 2DEG and for a possible back-gate underneath the QW[1]. Eventually the carrier density n of the tested wafer also has an effect on the measured resistance and the quality of the ohmic contacts. Thus it becomes necessary to structure ohmic contacts from different metals on the same chip.

In order to exclude variations in n, the following parameters have always been tested on a single wafer: contact material, etch depth and contact area. First a mesa in a standard Hall bar geometry was defined, similar to the structure depicted in Fig. 4.1. The pattern was transferred using a Cr lithography mask in soft contact mode, and

[1]Unlike a top gate, a back gate is used to control the carrier density from underneath the QW. A conducting substrate or highly doped MBE grown layer can be utilized as electrode.

a Hg-vapor lamp as UV source with its main emission at $\lambda_I = 365$ nm. The pattern was dry etched using an Ar^+ ion beam source with optical resist employed as an etch shield. This dry etching technique gives more precise etch results compared to wet etching processes on HgTe [105]. This process provides reproducible samples with precisely defined dimensions, that serve as a basis for our tests. Instead of utilizing a lithography mask as for the mesa, the ohmic contact areas were exposed sequentially, using an optical microscope with a hexagonal aperture. This allows us to define each contact separately and change its parameters giving a high flexibility. Furthermore, contacts can be extended into the etched sample area, allowing for ultrasonic bonding without mechanical destruction of the heterostructure and thus affecting the observed resistance. The contact metals were evaporated in an ultra high vacuum (UHV) chamber with a base pressure of (10^{-8} to 10^{-9}) mbar, using electron beam induced physical vapor deposition. The estimated distance between the crucibles and the sample was 40 cm. The sample holder was not cooled during the evaporation process. A schematic picture of the test structure is shown in Fig. 4.5. Green areas show the etched mesa, orange areas indicate the evaporated metal area and dashed lines demonstrate the actual overlap between metal and mesa. The width W of the evaporated contacts is defined by the etched mesa design and is kept constant at 150 µm, while the overall contact area A can be enlarged by simply extending the length of the exposed area [compare Fig. 4.5 a)]. In order to measure the contact resistance, a current is passed for example from contact 1 to contact 2, while the voltage is measured between contacts 1 and 3.

Table 4.1.: *Tested metals and corresponding melting temperatures.*

Metal	Melting temperature T_{m} [°C]
In	156
Al	660
Ni	1455
Ti	1668
Co	1495
Pt	1768
AuGe (eutectic, 80/20)	361

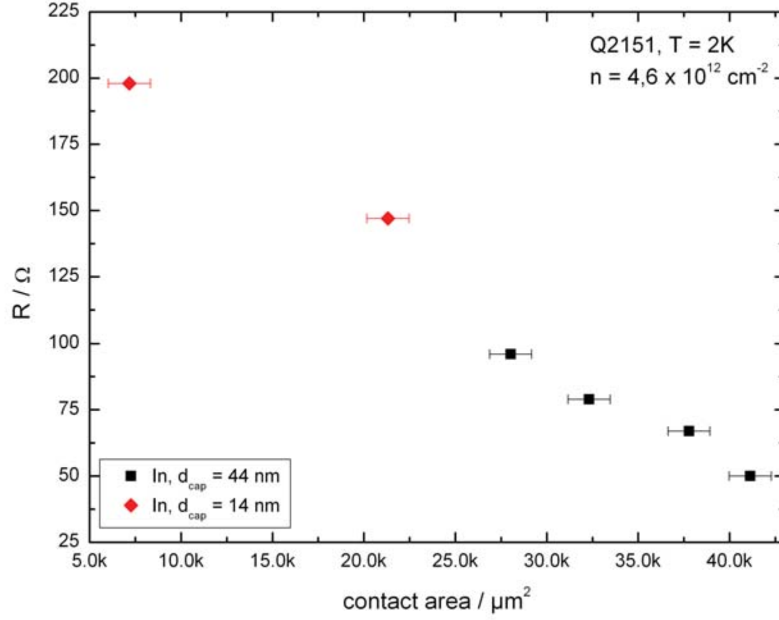

Figure 4.6.: *Three terminal resistance measurement of evaporated In contacts at* $T = 2$ K*, plotted against the contact area. The error bars are estimated from the technological uncertainty in identifying the actual contact area. Dry etched contacts with a thinner cap layer are marked as red diamonds.*

In this three terminal configuration the residual resistance of cables, bonding wires and 2DEG is assumed to be negligible and the main voltage drop should occur at the ohmic contact. The current is determined form the voltage drop over a reference resistor. The metals evaporated in our experiment and their corresponding melting temperatures T_{m} are listed in Tab. 4.1. We will mainly focus on the results obtained with In and AuGe. The first samples were prepared with In contacts for optimum comparability with the established thermal bonds and because of its very low melting temperature T_{m}, suggesting to have the lowest necessary temperature to initiate the diffusion process. AuGe was chosen as it is a well established material combination for GaAs/AlGaAs heterostructures. As a eutectic alloy AuGe has a very low melting point which is much lower than the melting temperature of the single compounds [106]. Figure 4.6 shows a low temperature measurement ($T = 2$ K) on a sample structured from wafer Q2151. Note that the carrier density $n = 4,6 \cdot 10^{12}$ cm^{-2}, determined from a reference Hall bar, is one order of magnitude larger for this particular wafer than for the samples measured by König *et al.* [14]. The contact size in this test was varied

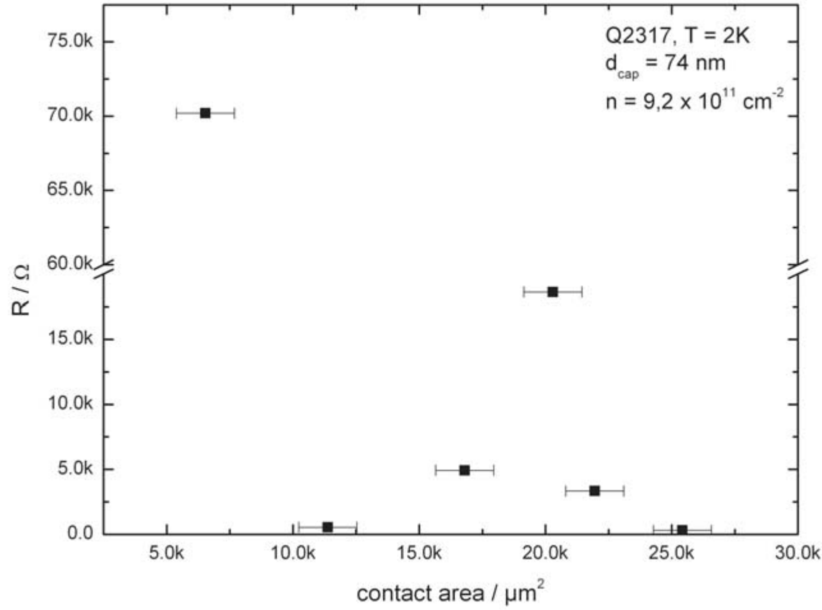

Figure 4.7.: *Three terminal resistance measurements of evaporated In contacts at* $T = 2$ K, *plotted against the contact area.*

to observe a possible dependence. A detailed parameter list of all used wafers can be found in the appendix. Four In contacts on the device were evaporated directly on top of the 44 nm cap layer, without any previous etching or post annealing. For two additional contacts the cap layer was thinned down prior to metallization to 14 nm using Ar^{+} ion beam etching (IBE). The actual contact size was determined from optical microscope pictures at a fixed magnification and by calibrating the ratio of pixel to µm. The pixel in the contact area were counted automatically using digital image processing software. The error bars were estimated from the uncertainty of the initial pixel-to-µm calibration and deviation in the pixel selection for area calculation. The contact areas are equivalent to squares of 70 µm to 220 µm edge length or, normalized to the fixed mesa width of 150 µm, lengths of 30 µm to 300 µm. The low resistance values indicate an almost perfect interface to the 2DEG. The data also demonstrates a decreasing resistance with increasing contact size. However, there is no indication that the contact resistance for that wafer and metal is significantly improved by diminishing the distance between evaporated In and 2DEG. The data points for the thinned cap layer fit well to the area dependence observed for the unprepared contacts. This measurement already suggests that the effect of diffusion, doping or the eventual formation

of an amalgam, happens over a range longer than the cap layer of 44 nm. Remarkably it is neither necessary to clean the contact area from the natural oxide, nor is an additional annealing required to achieve a low contact resistance. Indium is successfully used as n-type dopant in MBE grown HgCdTe and CdTe layers and forms good ohmic or at least pseudo-ohmic contacts [107–109]. The In-Hg amalgam is also known to make good ohmic contacts to various II-VI semiconductors [110, 111]. Like an ohmic contact, a pseudo-ohmic contact has a sufficiently low resistance value compared to the semiconductor device, but does not necessarily have a ohmic I-V characteristic over the whole voltage range.
These preliminary results, however, cannot be transferred to wafers with lower carrier densities, as can be seen in the measurement in Figure 4.7. This data was obtained on material Q2317, which exhibits a lower carrier density of $n = 9.2 \cdot 10^{11}$ cm^{-2} and was grown with a larger cap layer thickness of $d_{\mathrm{cap}} = 74$ nm. The contact sizes are comparable to the previous experiment, but no clear area dependence can be observed. None of the measured contact areas were etched before metallization. The measured resistance values are scattered over a wide range of a few 100 Ω up to several kΩ. Inhomogeneities in wafer material with lower carrier densities would be more pronounced in transport measurements. However, this cannot fully account for the large deviation in resistance of identically structured contacts. It is more likely that the diffusion through the cap layer is not uniform. This effect is amplified by the almost doubled distance between the metal layer and the 2DEG and the reduced carrier density. This assumption is supported by measurements conducted on wafer Q2388, presented in Fig. 4.8 and Fig. 4.9. Contact sizes are again comparable to those of the previous measurements. The carrier density $n = 2.1 \cdot 10^{11}$ cm^{-2} is much lower than in the prior samples and the cap layer $d_{\mathrm{cap}} = 114$ nm is much larger. This setup enables us to structure multiple contacts with different cap layer thickness on the same sample. The cap layer thickness for different contacts was varied in steps of 114 nm, 84 nm, 54 nm and 34 nm using Ar^{+} ion milling. Figure 4.8 and Fig. 4.9 show resistance measurements for contacts as a function of cap layer thickness and contact area. As can be extracted from Fig. 4.8 the reliability of ohmics decreases with larger cap layers, while Fig. 4.9 shows that even for small contact areas the quality of etched ohmics is very good. In addition, the measurements show that, even with cap layers as large as 114 nm, ohmic contacts can be achieved for low density QWs. These observations are in line with reports in Ref. [112]. Almost immediately with beginning evaporation a loss of Hg occurs in the first 10 Å of

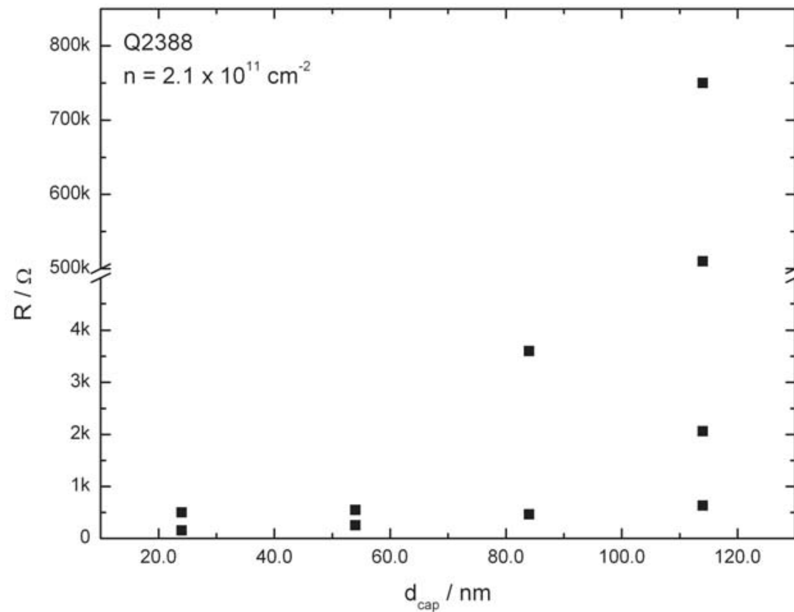

Figure 4.8.: *Three terminal resistance measurements of evaporated In contacts at* $T = 2$ K*, plotted against the cap layer thickness* d_{cap}.

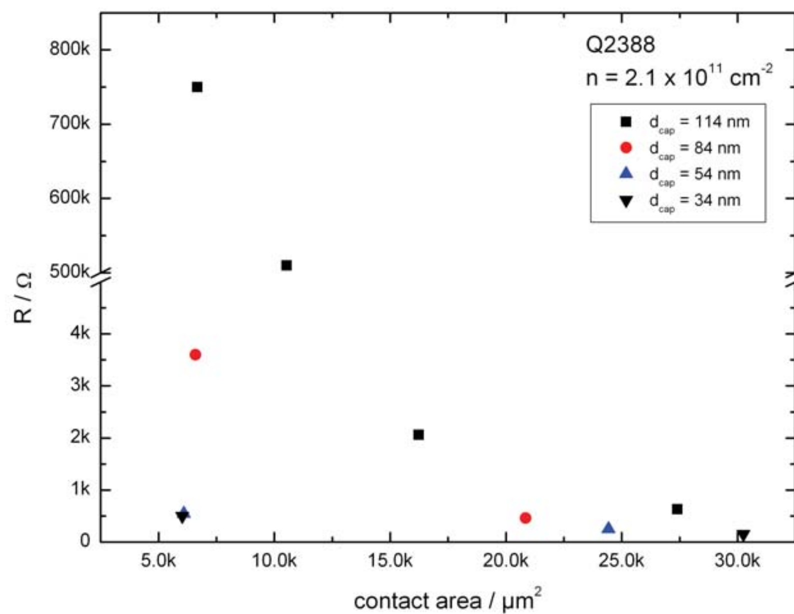

Figure 4.9.: *Three terminal resistance measurements of evaporated In contacts at* $T = 2$ K*, plotted against the contact area.*

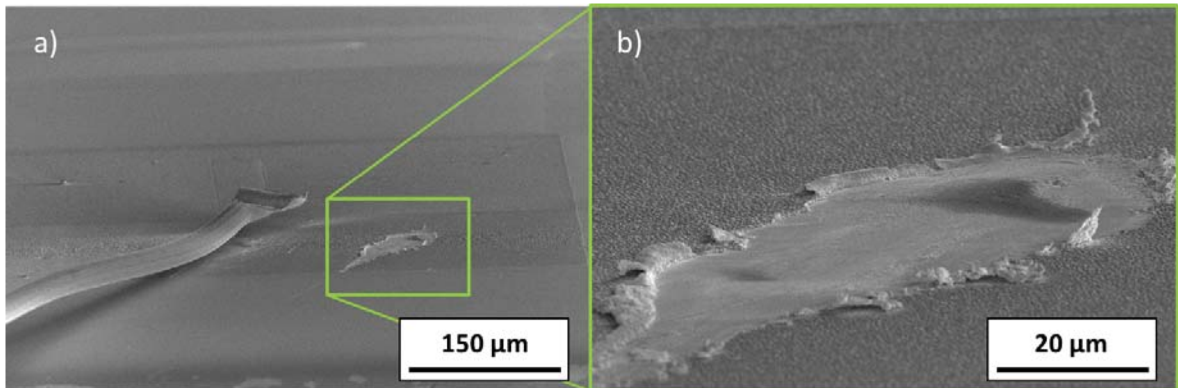

Figure 4.10.: ***a)*** *SEM micrographs of a ripped off Au bonding wire on evaporated In.* ***b)*** *Closeup of the bonding area.*

the In/HgCdTe interface. With increasing metal thickness, outdiffusion of Te can be observed, while the electrical properties are mainly dominated by the indiffusion of In, leading to n-type doping [112]. It was also observed that the metal evaporation leads to a reduction of the natural surface oxide [112]. Despite the good electrical properties of the evaporated In ohmics, other material combinations should be considered mainly for technical reasons. Because of the soft In surface, it proves difficult to directly bond the Au wire on the evaporated ohmic contact as can be observed in Fig. 4.10. Although this problem can be addressed with e.g. extended Ti/Au leads, reliability issues of the contacts at low temperatures remain for the previously discussed reasons. Similar results as for In were observed with the evaporated Al contacts. Al is also reported to lead to a massive depletion of Hg from the surface of HgCdTe substrates during the evaporation process. This is true for room temperature but also for cold evaporation at 100 K [112]. This fact should be kept in mind for further lithography applications. Al reacts with the semiconductor anion forming Al_2Te_3, while the diffusion of Al leads to a n-type doping. Because of the high reactivity of Al, the possibility to form tunnel barriers on HgCdTe using few monolayers of evaporated Al and subsequent oxidation, as e.g. possible for graphene, is questionable. At the same time it is very likely that the electron density of the well will be affected, thus changing the intrinsic MBE doping level. Note that also for evaporated Al no post annealing is necessary to form ohmic contacts.

Evaporation of pure Au on a HgCdTe surface behaves slightly different than observed for In or Al. Photoelectron spectroscopy (PES) and x-ray photoelectron spectroscopy (XPS) data from [112] confirm that no significant depletion of Hg is observed. How-

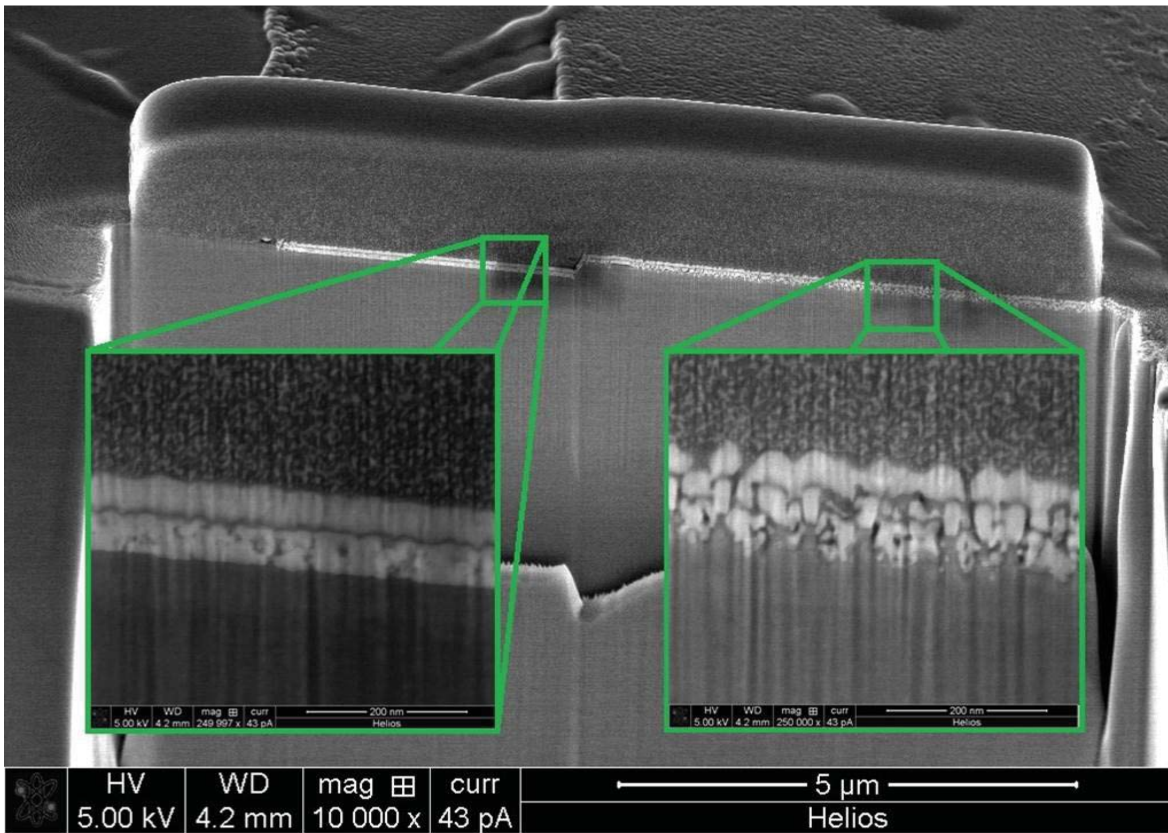

Figure 4.11.: *SEM image of a cross-section through an evaporated ohmic contact at the mesa edge prepared by standard FIB techniques. Insets show magnified pictures of the metal/CdTe interface (left) and the metal/HgCdTe interface (right). While the layer structure of the evaporated metal (AuGe/Ti/Au) is still visible on CdTe, strong clustering can be observed for the HgCdTe interface.*

ever, a strong interdiffusion of Te into the metal area and of Au into the semiconductor surface is reported. This leads to a p-type doping in the HgCdTe layer. For HgTe rich layers clustering of Au can be observed and Hg is expelled rapidly. This could be especially important for three dimensional strained HgTe bulk layers if surface states are probed locally, since strong alteration of the composition is expected. Pure Au has been used in the infrared detector community to form ohmic contacts on p-type HgCdTe. Despite good electrical properties, the mechanical interface appears to be rather weak, often leading to delamination of the Au sheet during further processing [113] similar to Pt. Both was observed during our tests. This delamination can be attributed to the difference between the thermal expansion coefficient α of Au ($14.2 \cdot 10^{-6}$/K at 20°C) and

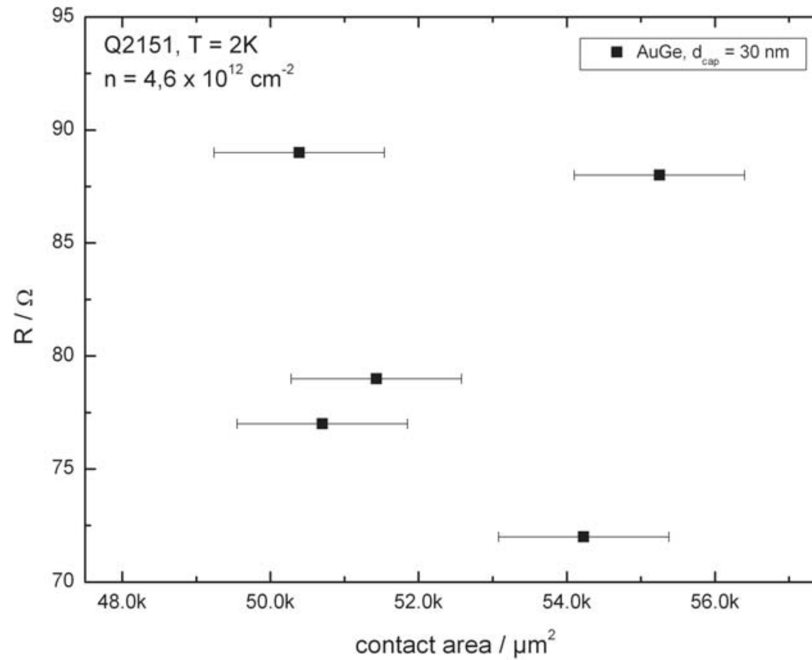

Figure 4.12.: *Resistance measurement for different AuGe contacts on Q2151.*

CdTe ($5.9 \cdot 10^{-6}$/K at 20°C). Attempts using Mo as interface layer to reduce mechanical stress have proven successful [113]. The thermal expansion coefficient of Ge with $\alpha = 6.0 \cdot 10^{-6}$/K at 20°C is close to that of Mo ($5.2 \cdot 10^{-6}$/K at 20°C), suggesting that Ge could have a similar effect. Our experiments show that bonding is significantly improved for AuGe pads compared to pure Au or Ti/Au and that contacts survive multiple thermal cycles without noticeable degradation. Au in combination with Ge forms an eutectic material, leading to a strong reduction of the melting temperature. The intention behind the use of this eutectic for HgTe/HgCdTe is to reduce the heat load for the sample and at the same time promote the diffusion process of the evaporated metal. In order to demonstrate the strong diffusion mechanism for Hg containing layers, a cross-section through an AuGe/Ti/Au ohmic contact at the mesa edge was performed using focused ion beam (FIB) techniques. The result is shown in Fig. 4.11. The evaporated metal layer completely covers the mesa on the right side which consists of HgCdTe. On the left side the HgCdTe was removed by an Ar^+ ion milling step until the CdTe substrate was reached. The mesa definition is followed by a electron beam evaporation step, depositing 50 nm of AuGe 5 nm of Ti and 50 nm of Au. The metal

sheet intentionally extends into the etched region to prevent a magnetic freezeout of the contact during high magnetic field measurements. Except for the Ar^+ IBE step both sides have been treated equally.The insets show magnified pictures of the marked regions. In case of the CdTe surface the layer structure is clearly visible and the interface between metal and semiconductor appears to be very sharp. Remarkably, this completely changes for the HgCdTe interface. Here a tooth like structure can be observed and the sharp transitions between the metal and semiconductor layers vanish. Similar structures have been observed for annealed AuGe/Ni/Au contacts on GaAs based semiconductors [114]. Our observations impressively demonstrate that strong diffusion of AuGe in HgCdTe layers is present even without an additional annealing step. Figure 4.12 shows a measurement for AuGe ohmics, deposited after dry etching the cap layer of Q2151 down to 30 nm. Resistance values are comparable to the In measurements on the same wafer. No conclusive area dependence is visible. Variations in resistance are more likely to occur from different current densities. As already mentioned, the total resistance does not only depend on the contact area. Figure 4.13 a) shows the situation for contacting a horizontal diffusion layer as typical in MOS-FETs. Here the total resistance R between the leading edge of the ohmic, shown as point x

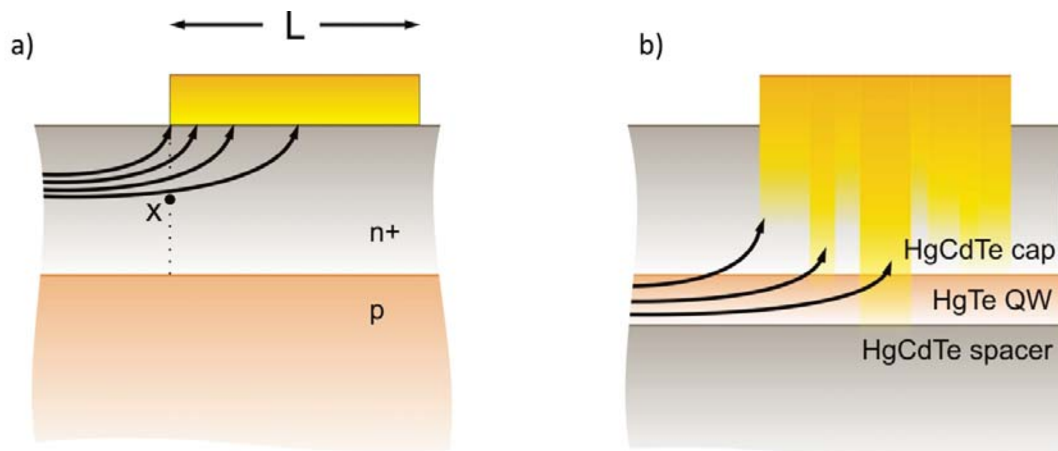

Figure 4.13.: ***a)*** *Current pattern for a horizontal diffusion layer as adapted from Ref. [98]. For higher sheet resistance the current will be forced to the leading edge x of the contact area.* ***b)*** *Equivalent picture for HgTe/HgCdTe heterostructures. Metal diffusion is not uniform over the whole contact area, leading to variations in the sheet resistance.*

in Fig. 4.13 a) and the metal sheet is given by [115]

$$R = \frac{\sqrt{R_\square R_C}}{W} \coth\left(L\sqrt{\frac{R_\square}{R_C}}\right), \tag{4.2}$$

where $R_\square$[2] is the sheet resistance of the diffusion layer in $\Omega/\square$ and L the length of the contact. Figure 4.13 b) displays the situation for ohmic contacts in HgTe/HgCdTe QW structures. The metal diffusion can be inhomogeneous over the whole contact area leading to a varying sheet resistance. If the sheet resistance is large, the current is forced to the leading edge of the contact (current crowding) leading to a nonuniform current density in the diffusion layer. In the limit of $R_\square$ going to 0, Eq. 4.2 is reduced to Eq. 4.1. In our case the sheet resistance is determined through the cap layer thickness and the diffusion of the evaporated metal. Since In contacts show a rather area dependent behavior, it is likely that an almost ideal metallic region is formed between In interface and 2DEG. Figure 4.14 shows measurements for AuGe contacts on wafer Q2320 with different cap layer thicknesses. The contact area is kept fixed at a value of approximately 45000 μm^2. As expected the data suggests, that a reduction of the cap layer leads to better ohmic contacts. Variations in resistance can be explained by inhomogeneities in the wafer, non-uniform metal diffusion, and minor geometrical differences, as has been observed for comparable systems [116]. To achieve an optimal diffusion of the contact metal it is advisable to clean the area from the natural oxide either by wet chemical pretreatment or dry etching. As a general rule, thinner cap layers lead to smaller contact resistance and more uniform diffusion in the metallized area. Linear I-V characteristics are observed also for barriers of 105 nm as shown in Fig. 4.15. As an empirical value, however, it is recommended to etch the top barrier down to a minimum of at least 30 nm, to get most reliable results. To access the well, for example for direct probing of the QSH edge channels, the whole barrier has to be removed very carefully. The observed depth of trenches formed during the dry etching process is about 10% of the total etch depth, thus being able to cut the QW and significantly increase the resistance again.

[2] square resistance

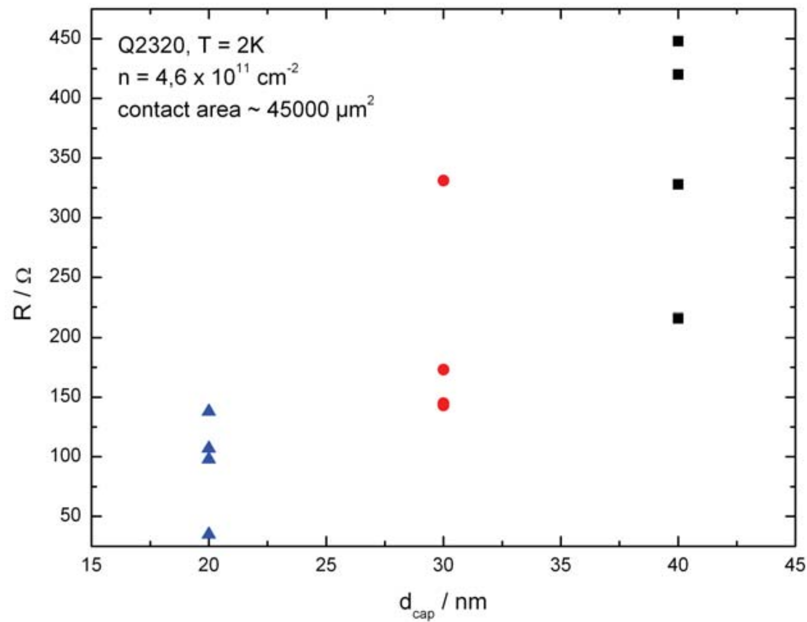

Figure 4.14.: *Resistance of AuGe ohmics on Q2320 for different cap layer thicknesses. A decrease of resistance for thinner cap layers can be observed.*

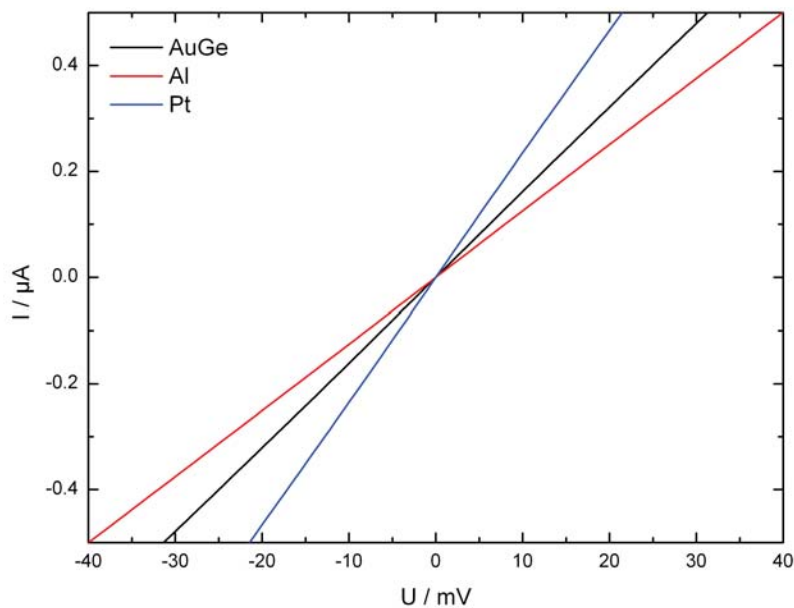

Figure 4.15.: *DC I-V curves for different metals on cleaned HgTe/HgCdTe with a barrier thickness of* 105 nm *measured at* $T = 4\,\mathrm{K}$*. Linear behavior is observed within the common excitation voltage range.*

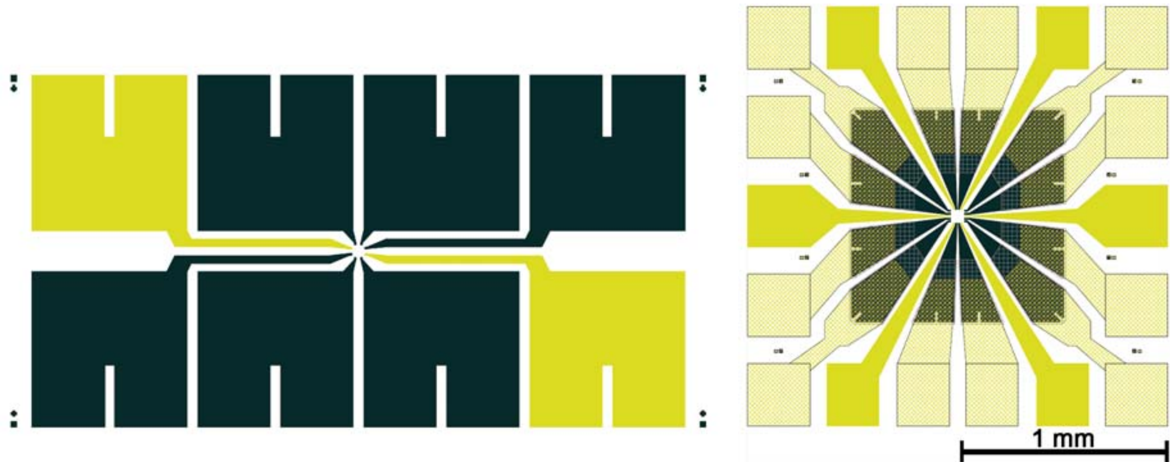

Figure 4.16.: *Comparison of old mask layout for contacting e-beam structures (left) to the new design with extended bondpads (right). The number of ohmics is increased from 6 to 12 and the number of gates from 2 to 6. The scale bar applies to both designs. Further miniaturization is still possible.*

Summary

The new evaporation technique provides a superior contact quality and handling compared to the In soldering that has been used so far. It can be stated that all tested metals form ohmic contacts on HgTe/HgCdTe heterostructures. No additional annealing step after evaporation is necessary, suggesting that the energy distribution during deposition is sufficient to trigger reactions and diffusion. Evaporated In provides very good electrical properties but is difficult in handling during the lithographic process and bonding and causes contacts to age. AuGe provides stable low resistance ohmic contacts, that can be easily structured in any desired shape using standard lithography and lift-off techniques with high reproducibility. No delamination was observed for this material combination. Because of its very good adhesion AuGe is suitable for ultrasonic bonding, thus allowing for a significant reduction in sample size. Adapting this technique into the standard fabrication process we were able to increase the sample output from standard wafers (1×1) cm^2 by 50% and simultaneously more than double the number of contacts available for ohmics or gates. Figure 4.16 shows the old and new mask layout in comparison. The scale bar applies to both designs. Further miniaturization is still possible using this contacting method. Limitations occur from sample cleaving and inhomogeneous resist coating for smaller chip sizes.

4.2. Reduction of sidewalls and fencing for HgTe heterostructures

Nanolithography usually combines various etching and deposition methods to generate complex pattern and devices. Resists are used to transfer the designated design onto the chip and often serve as an etch- or evaporation mask that can be structured in a suitable exposure process. One problem often encountered during the lithography process is the formation of sidewalls and fences. Sidewalls usually occur from evaporated metal which is deposited on the resist walls and is not properly removed during the following stripping process. They can pose a critical threat for the device, as a partial lift-off can cause a short between otherwise isolated areas. Due to their high aspect ratio sidewalls can penetrate insulating layers and even damage measurement equipment as for example used in sensitive scanning probe measurements [38]. Similar effects can be observed for fences. These structures may have different origins like crosslinked resist, material redeposition or a combination of both, but usually result from a not optimized process or improper interplay of different lithography steps. While there have already been efforts to reduce fencing [37] in HgTe/HgCdTe heterostructures, further improvements are possible.

4.2.1. Sidewalls

Avoiding the formation of sidewalls can be difficult for the partly isotropic sputtering deposition process. However, it can be inhibited for the anisotropic EB-PVD by optimizing the tilt angle of the resist walls. Positive resists are usually used as etch masks but can also be suitable for a lift-off process as long as the resist profile exhibits a sufficiently steep slope. For a positive optical resist the attainable wall angle depends on the contrast of the resist. The contrast determines the sharpness of the transition between exposed and non exposed resist parts [117]. The variation of the development rate with depth into the resist depends on the variation of the absorbed exposure dose with depth [118]. Therefore the resist wall slope depends on the absorption in the resist and the selectivity of the developer. As the top of the resist is exposed longer to the developer solution during development the structural width is smaller at the top than at the bottom, resulting in sloped walls. Typical angles for not chemically amplified resists (CAR) are around 80°. As the residual solvent in the resist plays a critical role

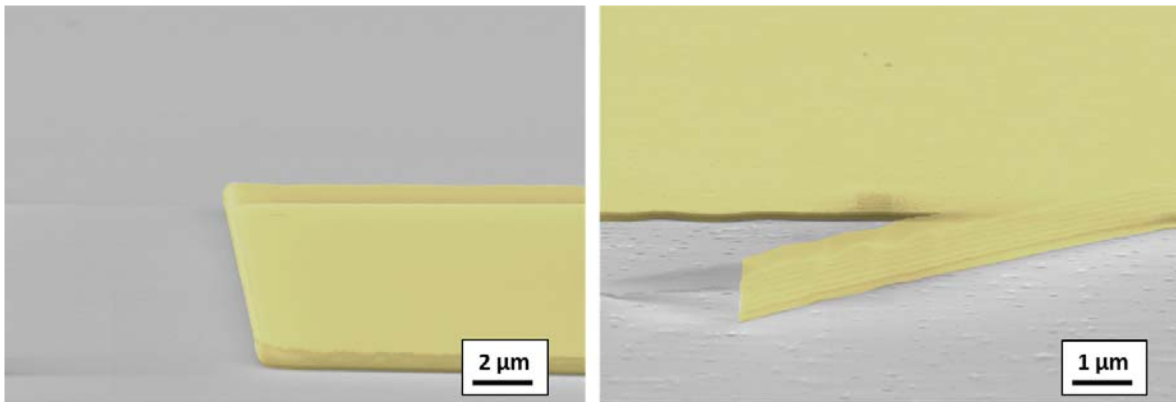

Figure 4.17.: *Colored SEM micrograph of two sidewall examples after evaporation of* 100 nm *Au onto a positive photoresist and lift-off in acetone. The structure height resembles the initial photoresist thickness.*

for the dissolution rate and therefore the resist profile [117], the post apply bake (PAB) temperature has to be chosen carefully. Typically recommended temperatures are often in the range of 90°C to 120°C, depending on the resin and photo-active component. Baking the resist at lower temperatures, as necessary for HgTe/HgCdTe, naturally reduces the contrast. With decreasing angles a thick metal layer will be deposited on the sides during evaporation and eventually form a stable structure that cannot be removed in a subsequent lift-off. Figure 4.17 displays examples of two different metal sidewall structures after evaporation of 100 nm Au on a positive photoresist and lift-off in acetone. Note that in the right figure the sidewall is partly peeled from the metal pad.

A possible alternative which completely avoids sidewalls is the use of a negative resist. Contrary to the positive process, structures exposed in a negative resist remain after the development step. The main advantage is the inverse resist profile originating from the exposure. This leads to a natural undercut[3] which is perfect for directed metal deposition. To harden the structures and keep the correct feature size, a precise post exposure bake (PEB) is necessary. Changes in temperature can result in size variation of the resist structure and therefore affect the final device dimensions. Although comparable temperature limitations do apply for these resist systems, a loss in contrast can influence the resist angle but it will stay an undercut. In order to compare the processes we fabricated reference structures using both types of resist.

[3]Negative slope.

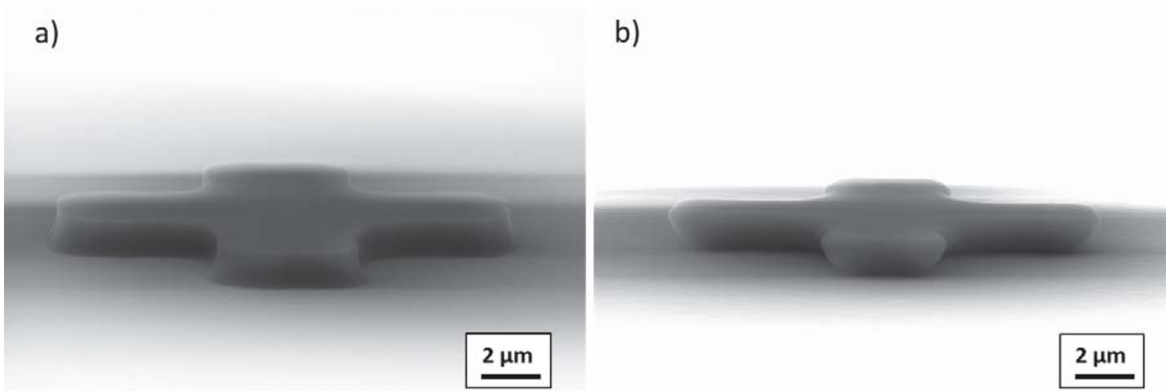

Figure 4.18.: *SEM micrographs of resist structures of nominal identical shape obtained from a positive and negative lithography process, respectively. a) Positive resist profile AZ ECI 3012 b) Negative resist profile AR-N 4340.*

AZ ECI 3012[4] is a novolac based positve photoresist designed for high resolution with strong dry and wet-etch resistance. Recommended baking temperatures are 90°C for softbake and 110°C for post exposure bake. AR-N 4340[5] is a chemically amplified negative resist, also based on a novolac resin with a photoactive acid generator and an amine based crosslinking agent, designed to be plasma resistant and suitable for lift-off processes. The recommended baking temperatures for post apply bake and post exposure bake are between 90°C and 100°C to obtain a sharp resist profile and achieve the optimum resolution. As it is not possible to apply the optimum temperatures for either resist system we had to adapt the process for HgTe. Figure 4.18 displays the nominal identical cross structure for the two different resist systems. Note that both resist profiles deviate from the optimum wall angle achievable with the recommended parameter settings. The result displayed in Fig. 4.18 a) shows the resist profile of ECI 3012 for a 2 min softbake at 80°C and a development time of 23 s in AZ 726 MIF. The active chemical in this developer is tetra-methyl-ammonium-hydroxide (TMAH). The post exposure bake was skipped to reduce thermal stress for the sample. The resist walls exhibit sharp edges, a slight footing is observable. The effective wall angle is approximately 80°. Comparable profiles lead to residual metal structures as shown in Fig. 4.17. Figure 4.18 b) shows the result for a 2 min soft bake at 80°C, a 6 min post exposure bake at 80°C and a development time of 50 s in AR 300-47 (mainly

[4]Manufacturer: AZ Electronic Materials plc / Merck KGaA.
[5]Manufacturer: ALLRESIST GmbH

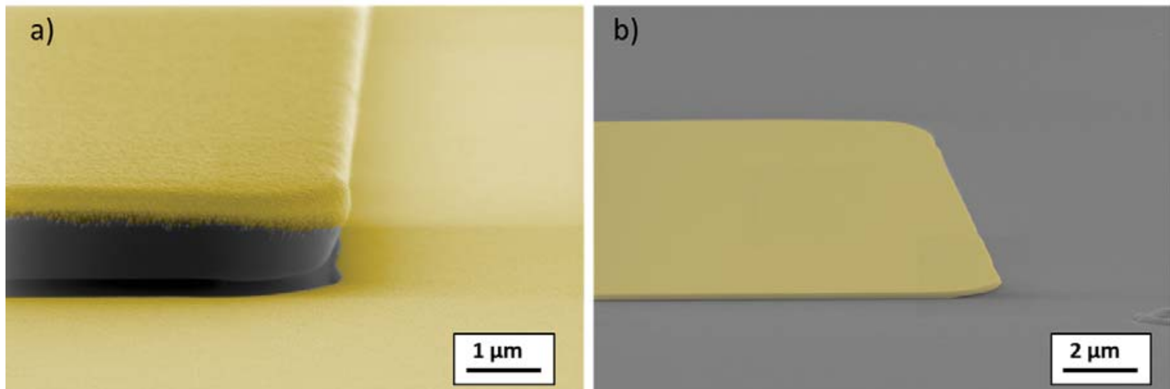

Figure 4.19.: *a) SEM micrograph of* 200 nm *Au evaporated on a* 1.3 µm *thick layer of AR-N-4340. Because of the strong undercut the formation of sidewalls is inhibited b)* 200 nm *Au on HgCdTe after lift-off. No metal sidewalls can be observed.*

TMAH). The lower baking temperatures result in shorter timescales for the complete development and reduced developer selectivity. Consequently this results in rounded resist structures and a significant undercut. Note that the post exposure bake cannot be skipped for the negative resist. A development time of 35 s is sufficient to remove a 1.3 µm thick layer. Increasing the development time leads to a stronger undercut. Figure 4.19 a) shows the negative resist profile after the evaporation of 200 nm Au. As expected for the undercut profile no sidewall formation is observed after resist stripping with acetone [compare Fig. 4.19 b)]. Although using the negative resist outside of its optimum parameter set this demonstrates its usability as lift-off mask, thus enabling a safe low temperature lithography especially suitable for large features like bond pads and macroscopic gates. The attainable resolution goes down to approximately 1 µm for i-line (365 nm) exposure.

4.2.2. Critical dimensions and fencing

Usually for a precise pattern transfer anisotropic etching is desired. Argon (Ar^+) ion beam etching or ion milling is a dry etching process that does not have a chemical reactive component and is purely based on sputtering and is therefore a mostly anisotropic technique. An ideal etch mask has vertical (90°) resist walls with a sufficiently small line edge roughness to assure a proper pattern transfer into the substrate. The change

of the critical dimension (CD) over etch duration is given in Eq. 4.3 [117]

$$\frac{dCD}{dt} = 2(R_H + R_V cot(\phi)). \tag{4.3}$$

The CD is therefore depending on the horizontal etch rate R_H, the vertical etch rate R_V and the resist wall angle ϕ. From this equation it is obvious that even for a fully anisotropic process with a horizontal etch rate $R_H = 0$ the tilt angle of the etch mask leads to an increase in pattern size for wall angles $\phi \leq 90°$. Figure 4.20 shows two SEM pictures of a positive resist etch mask (Shipley Microposit S1813 [6]) on a HgTe/CdTe wafer, exposed with UV-light (i-line) before and after the dry etching step. The chip was cleaved to get a crossection of the resist profile. The resist walls in Fig. 4.20 show an angle of roughly 80° and are comparable to the results discussed in the previous section. For an angle of 80° and an etch rate of 50 nm/min this equals a CD change of approximately 17 nm/min for a typical mesa height of 100 nm. While this deviation may be negligible for macroscopic devices, it becomes relevant for sub-micron structures as QPCs and wires. As already mentioned in the previous section, the wall angle is a result of the interplay between the horizontal and vertical development rate.
Further CD variations can originate from standing waves in the resist pattern [117]. This effect can be observed in Fig. 4.20. The monochromatic light arrives at the resist surface in approximately plane waves. For reflective substrates these waves bounce off the substrate's surface forming a standing wave pattern within the resist, with areas of high and low intensity at different depths. Consequently the exposure dose changes, leaving areas of more and less soluble resist layers in the desired pattern. This interference leads to so called swing curves, a sinusoidal variation in linewidth as a function of resist thickness [117]. The effect can be reduced by an additional PEB after the UV exposure to induce diffusion processes at the interface between exposed and unexposed areas. However, to reduce thermal stress for the sample, the PEB for positive resists can be skipped if not explicitly needed to achieve the desired resolution. Due to the deviation from an ideal vertical profile, not only the resist top but also the walls are exposed to the ion bombardment during the etching. As the ions streak the resist walls at a small angle they are scattered and redirected to the substrate, thus leading to a locally higher etch rate forming trenches to the sides [119, 120]. The trenches can be avoided by rotating the sample at a suitable tilt angle relative to the ion source in

[6] Manufacturer: Dow® Electronic Materials

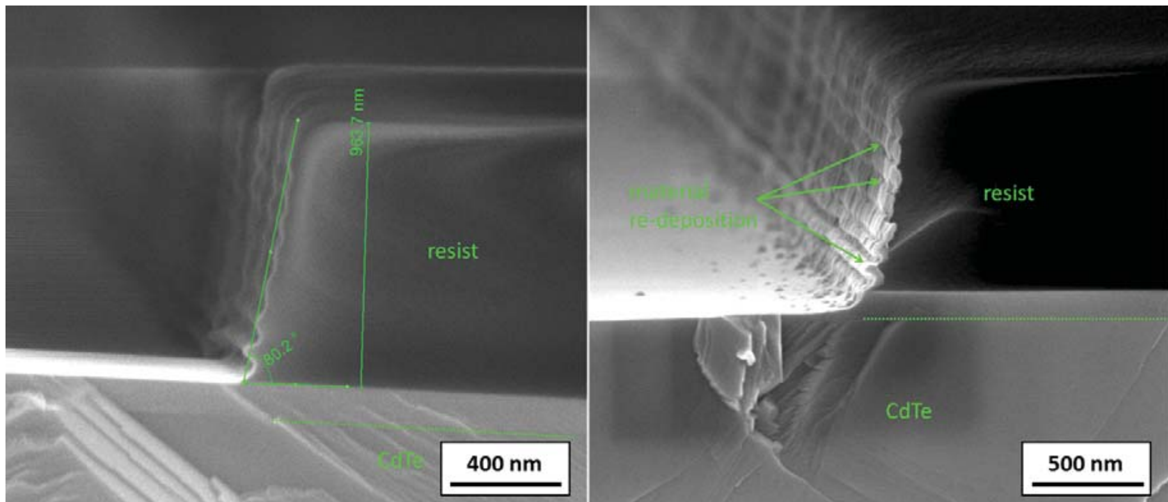

Figure 4.20.: *SEM pictures of a cleaved HgTe/CdTe wafer covered with an etch shield patterned in photoresist (Shipley Microposit S1813) before (left) and after* Ar^{+} *ion milling (right). The resist walls have an angle of roughly* 80°, *the resist thickness is approximately* 1 µm. *Dotted green lines are a guide to the eye for the interface between the HgTe layer and the underlying CdTe substrate. A slight color difference is visible.*

order to increase the angle of incidence for the ions. An even more severe effect than CD variation is the formation of fences. The incident ions can lead to a passivation of the resist walls by induced polymerization [120]. These passivated walls are tough to dissolve in a subsequent stripping step. Additionally they form a stable surface for the redeposition of non volatile material sputtered from the surface. Note that after the dry etch step in Fig. 4.20, the resist walls are covered with a thick shell of several nanometer. This shell mainly consists of redeposited semiconductor material, sputtered from the wafer during the anisotropic etching process. The resist top, however, is not covered, as potentially deposited material is continuously removed during the etching. The difference between redeposited material and resist is easily visible in the contrast variation in the SEM. As the sputtered material does not necessarily grow in the same stoichiometry, the emerging fences will also differ in their electrical properties.
In the subsequent lift-off only the unaffected resist will be dissolved. Depending on resist height, its thickness and the stability of the redeposited material but also the aspect ratio and sample design, fences of several (10 to 100) nm will remain at the mesa edges. Figure 4.21 shows a two-dimensional AFM (atomic force microscope) scan

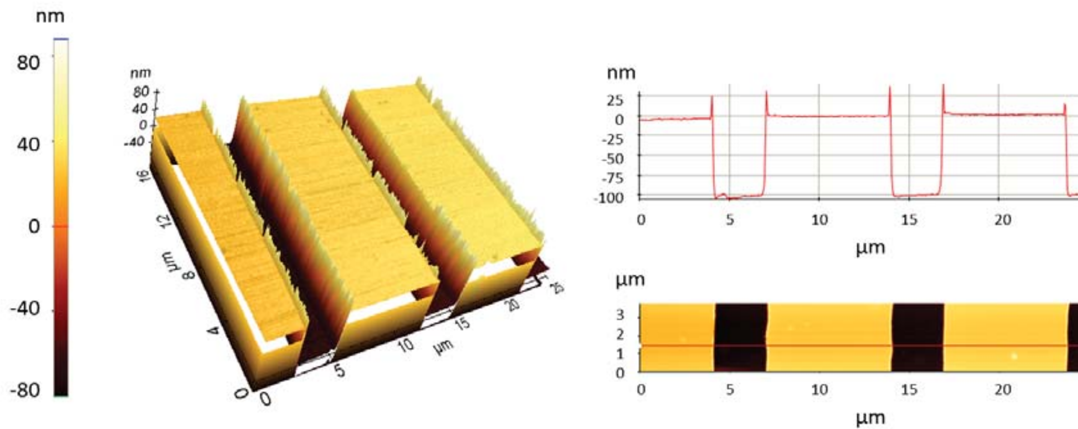

Figure 4.21.: *Two-dimensional AFM scan of a dry-etched stripe array after the removal of the resist etch mask. The profile linescan (red) clearly shows fences at the mesa edges of approximately* 25 nm *compared to a total etch depth of* 100 nm.

of an Ar^+ ion milled stripe array, fabricated in HgTe, after removal of the resist etch shield. The line scan clearly shows the remaining fence structures at the mesa edges. Most techniques used for resist mask removal are based on selective dry or wet etching. As the fences are also partly composed of the sputtered semiconductor material, most etchants capable of removing these residues will likely attack the sample itself, leading to different electronic properties or changing the CD of the structures. There are many commercially available wet chemical resist strippers mainly developed to suit silicone based lithography. These chemicals are often strong acids like e.g. $H_2SO_4 - Cr_2O_3$ but can also be alkaline based. For resist structures that have only been treated at low temperatures acetone will dissolve most of the resin but will also leave a residue, if not rinsed with IPA. Strong solvents like NMP or NEP are able to dissolve crosslinked resist residues, but do not attack redeposited material.
In case of HgTe heterostructures we successfully tested Technistrip® P1316[7] to remove the sidewall polymers (tested with AZ ECI 3012) and other organic residues from the substrate and bondpad surface without any measurable electronic alteration of the sample. Since this chemical is mainly composed of the solvent DMSO and the strong

[7]Manufacturer: Technic Inc.

base TMAH, it will also etch the native surface oxide. Thus Technistrip® P1316 is also capable of etching the redeposited material. More complex strippers usually are a blend of different solvents and alkaline additives in order to optimize stripping time and reduce sample contamination. However, it is crucial not to change the sample properties. It should be noted that many of these substances are toxic or even carcinogenic and can pose a serious health risk if not applied properly. Consequently their use should be as limited as possible. The aim for an ideal lithography process is clearly to inhibit the formation of fences.
One approach to prevent, or at least reduce fencing is the rotation of the sample under a tilted angle during the ion milling process as described in Ref. [37]. However, this requires a very precise adjustment of tilt angle, etch rate and rotation speed. In addition, in more simple machine setups not all of these settings are available. In order to achieve clean structures, even under a 90° incident angle without rotation, a hardmask is the best option. The hardmask material does not degrade during the IBE process. In addition, the mask height can be reduced to only a few nm, offering no basis for redeposition buildup. In semiconductor industry hardmasks are used for etching high aspect ratio features that conventional photoresists cannot withstand. The demand for high-resolution patterning makes this technology more and more necessary [121] and thus new mask materials are continuously being developed [122]. Doped amorphous carbon masks show excellent etch resistance in combination with easy removal after patterning in an O_2 ashing process [122]. As these masks are usually targeted to be only a few nanometer in height, the etch rate for the mask has to be ideally at least an order of magnitude smaller than for the substrate material. We have evaluated two different hardmask approaches for HgTe, using a combination of Ti with SiO_2 or Al_2O_3, suitable for positive and negative e-beam as well as for optical lithography.

4.2.3. Hardmask lithography

The concept of a sacrificial layer

As Chapter 4.1 shows, a high reactivity of various metals on HgCdTe/HgTe is observed. Despite the advantages for contacting the samples, this high reactivity can lead to problems in other lithographic steps and complicates the realization of certain experiments. The mesa for the samples presented in Refs. [14, 31] were produced using Ar^+ IBE. To define the mesa, the designated pattern was transferred into a 120 nm

poly methyl methacrylate (PMMA) layer using electron beam lithography at 2.5 kV. After exposure and development, 15 nm Ti was evaporated to serve as an etch shield. After the etching process, the Ti shield was dissolved in hydrofluoric acid (HF) [123]. Although pure Ti is suitable as a hardmask material, it is also known to react with HgCdTe and to form ohmic contacts, as reported e.g. in Refs. [124, 125]. This was confirmed by our own measurements. Depending on the amount of evaporated or sputtered Ti, this will lead to an alteration of the HgCdTe surface as was observed for other metals described earlier. A possible scenario is the unintentional doping of the HgCdTe cap layer, leading to higher carrier densities, which makes it difficult to access the QSH state in the available gate range.

Since HgCdTe bulk is not affected by HF [126], this acid is an excellent selective etchant to clean the surface from various metals and their oxides. MBE grown HgCdTe layers exhibit a Te rich surface forming TeO_2 after being transferred to atmosphere. TeO_2, however, can be easily dissolved in HF [127]. Ti and TiO_2 have been in use as etch shield for dry etching as well as for wet etching techniques [128, 129]. When exposed to air Ti tends to build a protective coating of TiO_2. Titanium itself is easily dissolved in HF. Although there are reports that TiO_2 is also dissolved in HF or buffered HF (BOE) [130, 131] it is much more stable and the reaction seems to depend strongly on the actual structure, material quality and temperature. Figure 4.22 a) - d) shows SEM micrographs of an evaporated Ti shield on a HgCdTe layer after treating the chip for 60 s in HF:H_2O (1:2). The designated pattern is easily visible indicating that either the Ti/TiO_2 layer was not entirely removed or a new insoluble compound was formed at the interface between HgCdTe and Ti. Figures 4.22 c) and d) impressively show the difference in surface roughness between the initial Ti shield area and the substrate.

This test imposingly confirms the necessity of an additional sacrificial layer which prevents the reaction and diffusion of the Ti etch mask and facilitates its complete removal. Possible barrier materials have to meet several key requirements in order to provide noticeable advantages for the final device. The influence of the sacrificial layer on the electrical properties of the sample has to be kept at a minimum. The barrier ideally is kept at a thickness of a few nm, both to not affect the resolution during the dry-etching process and to prevent the buildup of redeposition fences. It also should be removable, easy to pattern and its application should not exceed the the temperature limit of 80°C.

Two compounds provide a suitable solution for HgTe heterostructures and even offer

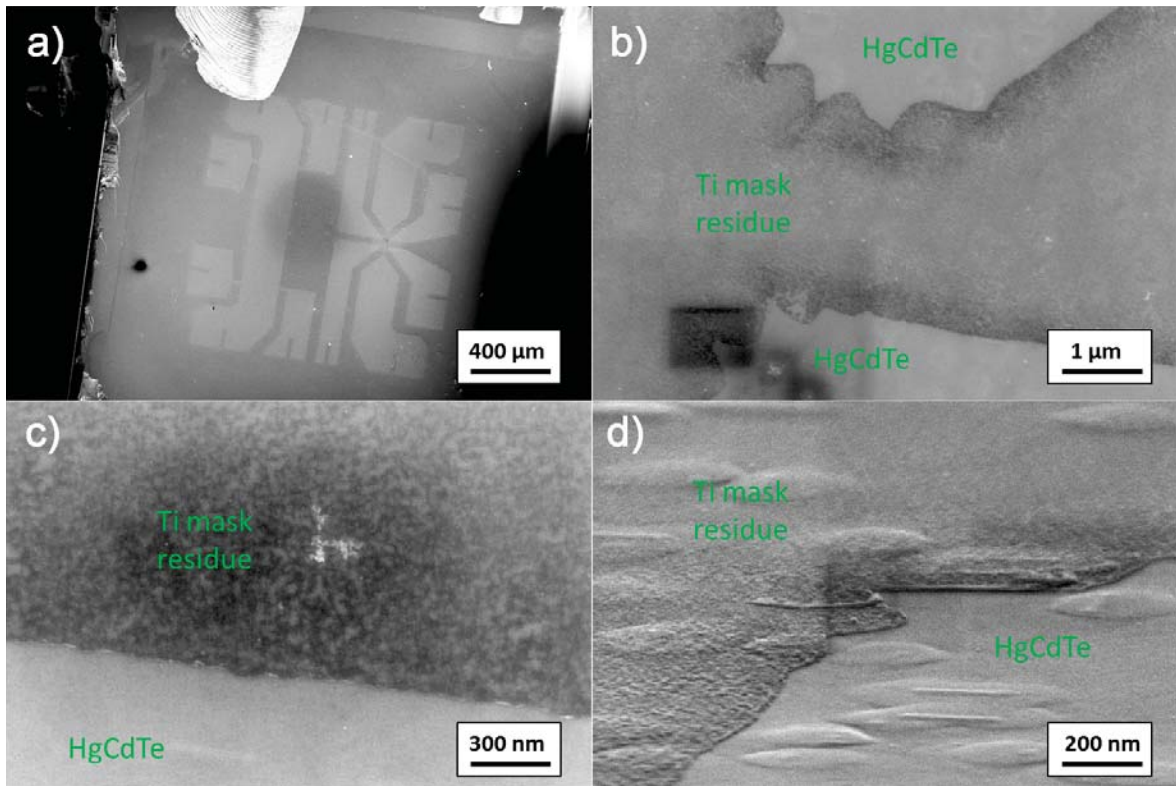

Figure 4.22.: *SEM micrographs of Ti remains on a HgCdTe substrate after treatment with HF. a) Still visible pattern after HF treatment b) Closeup of a Hall bar lead c) Transition between Ti exposed area (above) and not exposed part (below) d) Side view of the same area, clearly showing the surface roughness in the former Ti area. Oval structures show growth defects within the MBE layer structure.*

the choice between positive and negative lithography. One material is Al_2O_3, the other SiO_2.

Silicone oxide (SiO_2)

The MBE grown heterostructure is initially covered with a native oxide. However, this natural TeO_2 surface layer with a thickness of approximately 1 nm and a negative heat of formation of approximately 320 kJ/mol [133] is insufficient to serve as a diffusion barrier. For almost three decades in the infrared detector community Silicon-oxide (SiO_2) has been known to be applicable for HgCdTe surface passivation purposes, depending on the deposition method, growth condition and surface pretreatment [132, 134, 135]. Refractory metals like Ti often react strongly with dielectric surfaces. In case of SiO_2 this leads to the formation of a new interface layer, which is suitable as

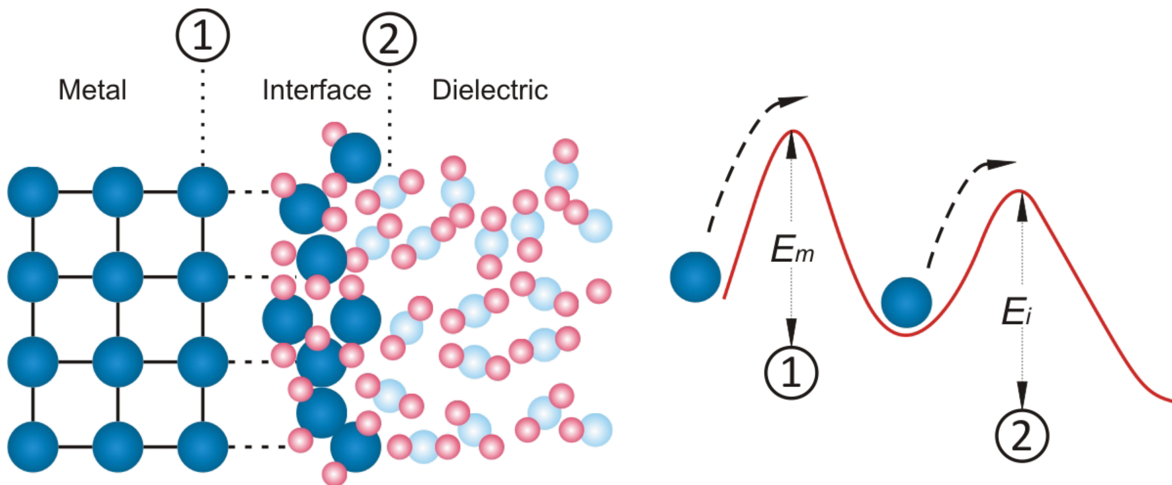

Figure 4.23.: Illustration of the metal-dielectric interface. Two energy barriers prevent the thermal diffusion of Ti into the dielectric, E_m is the energy necessary to leave the metal matrix, E_i is the energetic barrier resulting from the interface oxide. Adapted from Ref. [136].

a barrier against further diffusion into the dielectric. For evaporated Ti, this leads to a reduction of SiO_2 and the formation of a new Ti-oxide layer during the deposition. The reasons for this are the negative heat of formation per oxygen atom for TiO with 542.7 kJ/mol and TiO_2 with 472.0 kJ/mol compared with 455.2 kJ/mol for SiO_2 [136] and the thermal energy from electron beam evaporation. For Al_2O_3 this value is 559, 1 kJ/mol. Smaller negative heat of formation is equivalent to a lower tendency for oxidation. Thus the thermally deposited Ti can easily break the Si-O bonds to form a new oxide layer. Figure 4.23 illustrates the situation at the interface between the metal and the dielectric. In order to diffuse further into the dielectric, the metal atoms have to overcome two energy barriers: The Energy E_m necessary to leave the metal matrix and the energy barrier E_i resulting from the stable interface oxide. Therefore a sacrificial layer of a few nm should be sufficient to prevent metal diffusion into the substrate.

The introduction of this sacrificial layer necessitates further lithography steps. For the deposition of SiO_2 we used plasma enhanced chemical vapor deposition (PE-CVD) at 80°C, as is the standard procedure for the SiO_2/Si_3N_4 multilayer gate insulator, used in transport measurements. With this method the compound is formed in a RF generated plasma at 30 W with a gas flow of 150 sccm SiH_4 and 700 sccm N_2O. PE-CVD leads to an almost isotropic deposition of the formed material, which is not

suitable for a clean lift-off process. Prior to the first lithography steps the whole chip

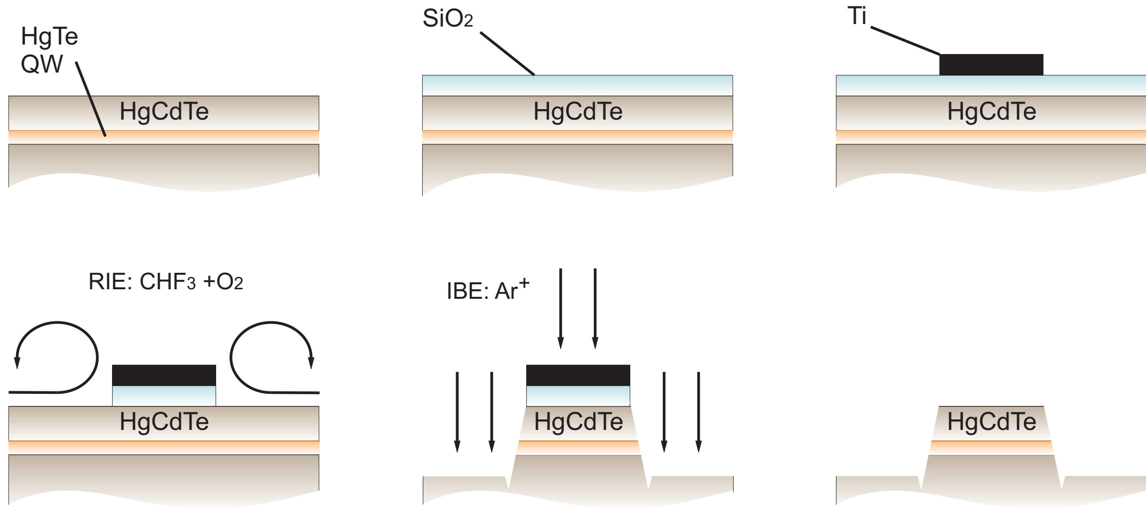

Figure 4.24.: *Schematic concept of the etch shield and mesa fabrication including a SiO_2 sacrificial layer. After deposition of the oxide on the clean substrate, the Ti shield can be structured with standard e-beam or optical lithography. The unnecessary oxide is removed in an isotropic dry etching step, using a combined CHF_3 and O_2 plasma. The mesa is defined using Ar^+ IBE. In a final step the sacrificial layer is dissolved in BOE, lifting the Ti layer.*

is covered with a 10 nm thick SiO_2 layer. This protects the substrate from further surface contamination. In a second step the Ti shield is patterned as usual on top of the SiO_2. Note that this sacrificial layer is not sensitive to the standard developer for PMMA based resists, such as isopropyl alcohol (IPA) and methyl isobutyl ketone (MIBK). Low temperature deposited SiO_2 forms small clusters and exhibits a non-uniform etch profile for pure Ar^+ IBE treatment [see Fig. 4.25 a)]. Therefore, prior to the Ar^+ ion milling, the uncovered areas of the sacrificial layer have to be removed. For selective dry etching of the SiO_2 layer we used reactive ion etching (RIE) with a mixture of CHF_3 and O_2, followed by a cleaning step in a pure O_2 plasma. The O_2 cleaning step is necessary to clear the surface of possible fluorocarbon films. Although not completely inert, the Ti mask layer shows negligible low etch rates, as does the HgCdTe surface. In the final step the mesa is defined by Ar^+ IBE. The sacrificial layer is then easily dissolved in buffered oxide etch (BOE) NH_4F : HF (7:1), lifting also the Ti sheet. The whole process is displayed schematically in Fig. 4.24. The solubility rate of SiO_2 is highly depending on the film quality. Usually using higher

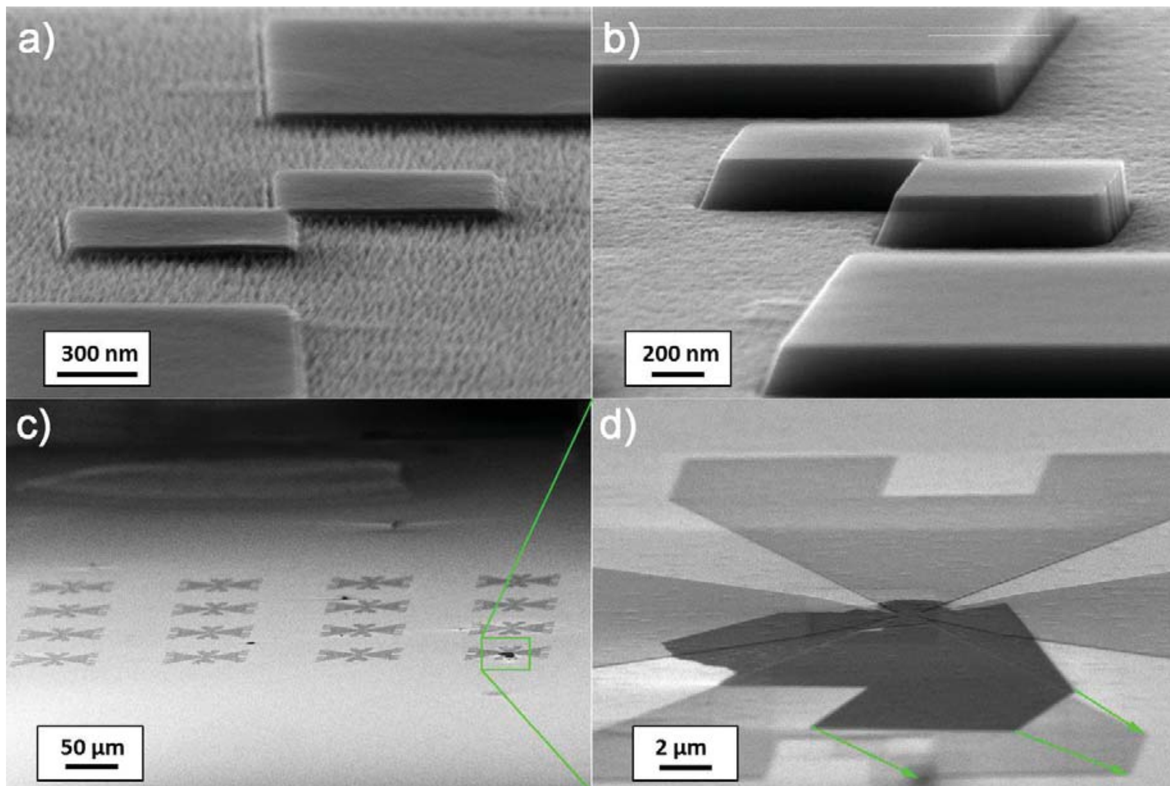

Figure 4.25.: *a) Ti etch shield with underlying SiO_2 sacrificial layer after IBE, without RIE removal of the uncovered SiO_2 b) IBE result with previous RIE step, leading to an obvious improvement. No fencing is observed. c) Array of 16 teststructures, after IBE and subsequent etch shield removal in BOE d) Closeup of one structure revealing the stability of the Ti/TiO2 shield. Only the sacrificial layer was completely dissolved.*

temperatures in the PE-CVD deposition process will increase the necessary etch time. Our experiments show a complete removal and Ti lifting in less than 60 s. In order not to affect the resolution for nano-structures, the total mask thickness needs to be kept at a minimum. Our experiments show that sacrificial layers of SiO_2 as thin as 10 nm and an additional Ti shield of 15 nm are suitable for high resolution pattern (minimum feature size $\approx$ 30 nm) and are still easily removable with BOE. Figure 4.25 shows SEM micrographs of an actual teststructure which has been processed by ion milling at an incident angle of approximately 90° without sample rotation to demonstrate the feasibility of the introduced hardmask/sacrificial layer concept. No fences are observed at the mesa edges. This test also reveals that the Ti/TiO_2 layer is not dissolved in BOE, but rather peeled as an intact sheet, comparable to a lift-off process. Similar behavior for TiO_2 layers has been observed by Ref. [129].

Aluminum oxide (Al_2O_3)

An even more versatile sacrificial layer can be achieved using Al_2O_3 grown by atomic layer deposition (ALD). Unlike in the CVD process during ALD the various reactants are introduced into the growth chamber sequentially and not simultaneously. In addition ALD is possible at relatively low temperatures, making it especially interesting for thermally unstable materials like HgTe. Most ALD processes are based on two different precursor gases and surface reactions. The reactions are self limiting as each precursor can only saturate a finite number of available surface sites. In principle this process allows the deposition of thin films with atomic level control [137]. For Al_2O_3 the precursor gases are tri methyl aluminum (TMA) and H_2O. An important factor for an ideal growth start is the complete surface saturation with the first precursor. While this can be delicate for inert materials like graphene [138], the natural TeO_2 allows for a good growth start. Once the surface is fully covered with the first precursor, longer exposure times do not lead to thicker layers. After the chamber is purged and evacuated the second precursor gas can be introduced, reacting with the hydroxile groups from the first precursor, leaving the surface in the initial growth condition and thus ready for the next cycle. Ideally this leads to a monolayer by monolayer growth. In reality, however, there is a transition between ALD and CVD because of remaining precursor from the previous step. In that context, several parameter determine the final layer quality, like growth temperature, exposure times, purge times and base pressure. While higher temperatures tend to give better layers because of enhanced surface diffusion, better reaction conditions and improved vacuum after the pump cycle, at least some low temperature effects can be accounted for by increasing the timescales for the growth steps. In theory a room temperature application is possible. Since the chamber pressure usually is in the 10^{-3} mbar to 10^{-5} mbar and thus far from MBE conditions, longer waiting times can lead to more defects in the grown layer. While low temperature PE-CVD tends to form small clusters, the alternating application of the two precursor gases still guarantees a better film quality. Although being a slower process than CVD - deposition rates usually do not exceed a few nm per hour - the thermal stress for the HgTe/HgCdTe layers can be reduced. We have grown perfectly insulating layers of 15 nm and below at temperatures between 60°C to 65°C. Apart from the obvious temperature advantage, the high film quality leads to additional lithographic improvements. Since the surface coverage is nearly perfect

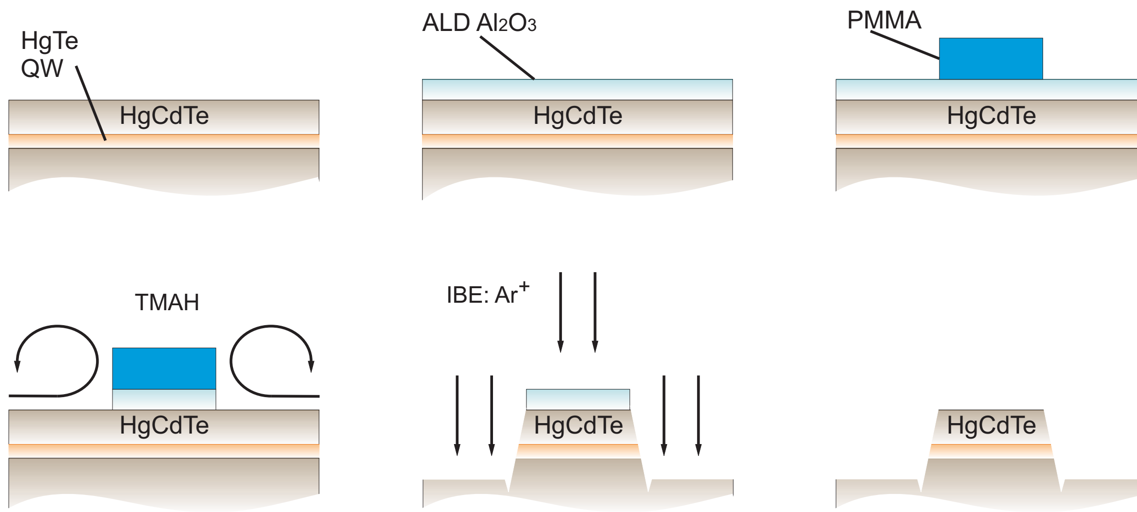

Figure 4.26.: *Schematic concept of a negative lithography process utilizing an Al_2O_3 etch shield grown by ALD. The layer can be patterned using e.g. PMMA as a protective layer. The unnecessary oxide is removed in an isotropic wet etching step, using a solution of TMAH. The mesa is defined using Ar^+ IBE. In a final step the hardmask is dissolved in TMAH or BOE.*

after a few monolayers, the thickness of the sacrificial layer can be reduced significantly. The layer smoothness and absence of larger clusters leads to sharper mesa edges after the IBE step. Its integrity also makes wet chemical applications more predictable and reproducible. In combination, this offers the possibility to choose between a positive lithography process, by adding a Ti mask, as described for SiO_2, or a negative process as illustrated in Fig. 4.26. In that case the Al_2O_3 layer itself serves as etch shield in the subsequent IBE step. Our experiments show that Ar^+ ion milling rates in ALD Al_2O_3 are at least two orders of magnitude lower than in HgCdTe. In order to pattern the layer, a precise resist mask can be structured using e.g. electron beam lithography in PMMA. Standard PMMA developer like IPA or MIBK do not attack the oxide beneath. Since PMMA is not a durable etch shield for chlorine or fluorine etching, the RIE step is substituted by a selective wet chemical etch step with tetra methyl ammonium hydroxide (TMAH).
TMAH is the standard active component for many optical developer solutions and is common for etching Al_2O_3 [139]. Despite that fact, pattern can also be generated using optical lithography. KOH developer solutions also attack the ALD layer but show a

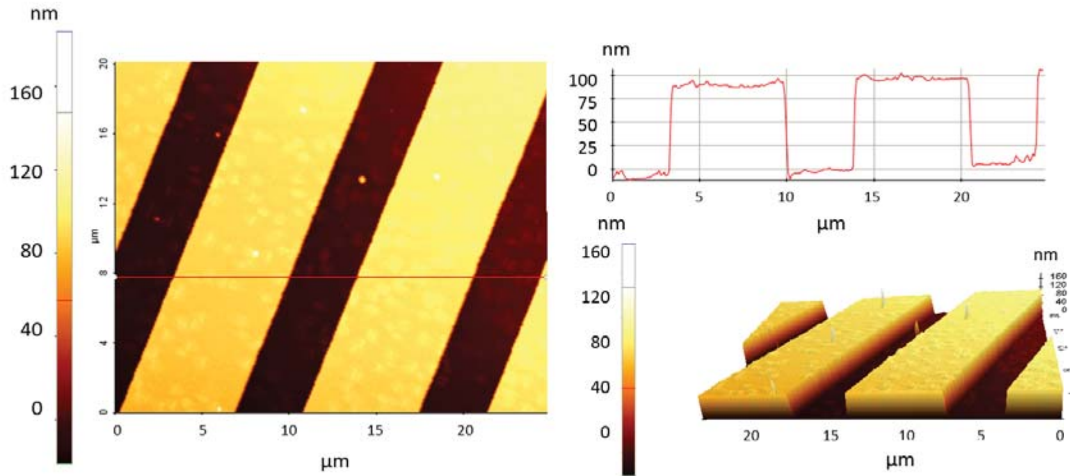

Figure 4.27.: *Two-dimensional AFM scan of a dry-etched stripe array after the removal of a* 10 nm *ALD hardmask. The profile linescan (red) shows no fences at the mesa edges. The surface roughness originates from growth defects in the test material and is not connected to the lithography.*

considerably lower etch rate, and thus are a possible alternative to TMAH. For the described negative process we used the developer Microposit MF CD26[8] with a TMAH concentration of 2,38%. The etching is isotropic and etch rates depend on the film quality, the growth temperature and the sample agitation in the solution. The exact timing for this process is very important in order to achieve a precise mask definition and has to be re-calibrated after changing the ALD growth parameters. Our experiments show that a 15 nm ALD sheet is penetrated in 30 s. Longer etching times can lead to an underetching of the Al_2O_3 below the patterned resist layer and, depending on the pattern geometry, to a complete lift-off of the resist mask. Delamination of the resist pattern timescales has been observed in certain samples but is attributed to surface contamination prior to the Al_2O_3 deposition. The etching process is easily stopped with a deionized (DI) water rinse. In a final step the resist mask can be dissolved in acetone, leaving an extremely thin hardmask for the subsequent IBE step. For the removal of the mask sheet TMAH or BOE can be utilized. Figure 4.27 shows a two-dimensional AFM scan of a stripe array defined with the described negative process, comparable to the array measured in Fig. 4.21. As can be extracted from the line

[8]Manufacturer: Dow® Electronic Materials

scan no fences at the mesa edges are observed for the ALD etch mask. This process was already successfully implemented in Ref. [140].

Summary

We were able to demonstrate that the concept of a sacrificial layer presents an effective alternative to pure Ti etch shields leading to a clean semiconductor surface. These layers can even be utilized as a mask system for positive and negative lithography. Diffusion of Ti into the semiconductor surface is effectively prevented by the SiO_2 or Al_2O_3 barrier. Alterations in the semiconductor surface arising from the sacrificial layer and a resulting change of the QW properties can be widely excluded as these materials are used as the standard insulators for HgTe/HgCdTe heterostructures.

4.2.4. Combining hardmasks and wet etching

As described earlier, material redeposition may not only lead to fences that are a threat to insulating layers causing gate shortages, but can also passivate the sample walls or change the electrical properties of the sample. For experiments focused on the properties of the mesa edge, such as microwave impedance measurements (MIM) of the QSH edge channels [140], it is crucial to have access to the sample walls without a dielectric or even conductive redeposition barrier. For that purpose we successfully combined the technique of an ALD grown Al_2O_3 sacrificial layer with a Ti hardmask with Ar^+ ion milling and an additional wet etch step [140]. As schematically shown in Figure 4.28 the mesa is defined in two steps. After the initial Ar^+ ion milling, for 60 s the sample is dipped into a solution of 1:1400 bromine in ethylene-glycol. The etch rates vary between (50 to 70) nm/min, depending on sample agitation and the exact concentration. As bromine is very volatile, the initial concentration will decrease over time, thus leading to lower etch rates. The result after the etch shield removal is a pristine sample surface with smooth sloped mesa walls. Because of slightly different etch rates for HgTe, HgCdTe and CdTe, the layer stack of the heterostructure becomes visible and the QW position can be directly observed in the SEM[9]. Figure 4.29 demonstrates the stability of the hard mask and how this technique can be utilized for nano-structures on HgCdTe/CdTe wafers. The etch mask is not attacked by the

[9]The MBE layer stack can also be observed in the SEM for cleaved chips imaged from the side, but the contrast between the different sheets will be less obvious.

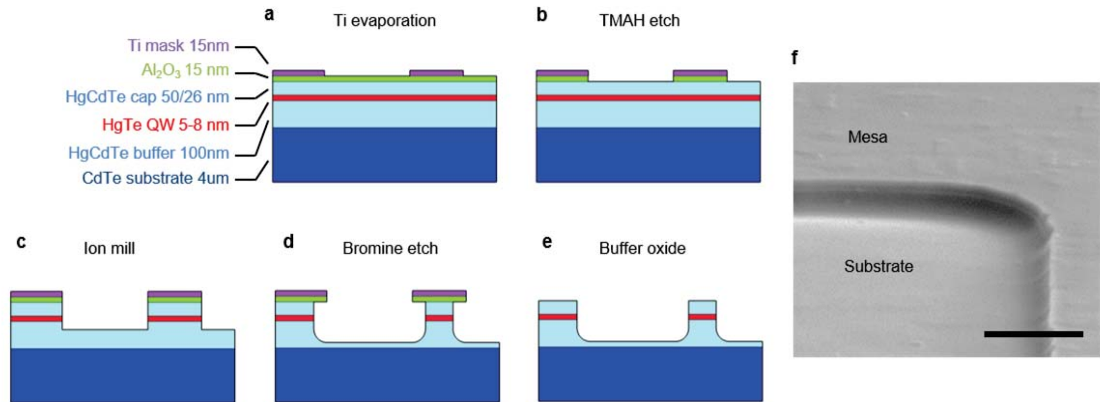

Figure 4.28.: ***a)*** *After growth of the Al_2O_3 sacrificial layer, the Ti mask can be patterned using standard optical or e-beam lithography and e-beam evaporation.* ***b)*** *The final hardmask is defined in a 40 s dip in a solution of TMAH (Developer CD26).* ***c)*** *The Mesa is defined in an Ar^+ ion milling step.* ***d)*** *An additional wet etch step is introduced.* ***e)*** *The mask is removed in BOE.* ***f)*** *SEM micrograph of a final mesa without fences showing smooth sample walls. The scale bar is 1 μm. [140]*

wet etch step. The displayed test pattern was generated by standard 2.5 kV e-beam lithography. After 100 nm dry etching into the substrate, the sample was treated with a solution of bromine in ethylene glycol for 60 s. The isotropic wet etch step increases the mesa height to 200 nm and leads to an underetching of the hardmask layer of approximately 100 nm without compromising its integrity. Additionally the mesa walls are now curved and not straight. The hard mask is then easily be dissolved in a solution of buffered oxide etch (BOE).
The main advantage of this combined etching process is the possibility to generate precise structures down to a few tens of nanometer and to subsequently cure the potentially altered sample walls. Using a pure wet etch process for mesa definition is desirable but usually lacks the necessary resolution and reproducibility for structures below 1 μm. In addition, for certain pattern like narrow gratings [154] or trenches with a high aspect ratio, a defined etch start as well as an etch stop cannot be guaranteed, thus leading to pattern irregularities. Reactive ion etching or chemically assisted ion beam etching could be suitable alternatives that still have to be evaluated for HgTe/HgCdTe heterostructures.

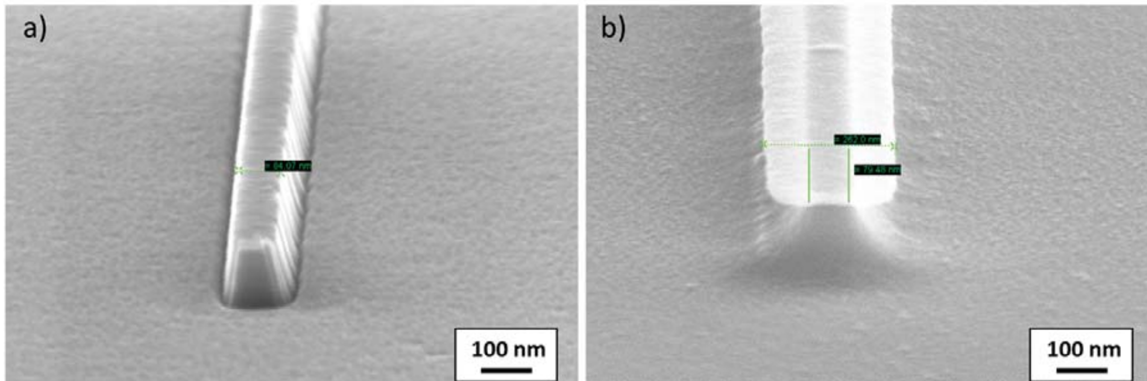

Figure 4.29.: *SEM micrographs of a* 80 nm *line pattern on a CdTe/HgCdTe wafer, structured using standard* 2.5 kV *e-beam lithography and a* 15 nm *hardmask. a) Pure* Ar^+ *ion milling. b) Two-step etching process combining* Ar^+ *ion milling and a bromine ethylene-glycol wet-etch similar to [140], before the hardmask removal. For the wet etch step the initial mask has to be larger than the final structure to achieve the same CD.*

4.3. Low energy e-beam lithography

Electron beam lithography (e-beam lithography) is a very versatile method to generate high precision nanostructures reproducible down to a few nanometer. However, the high energy electrons used for the resist exposure can also interact with the sample itself, leading to various elastic and inelastic scattering events. Examples are the generation of secondary electrons or x-ray radiation but most of the energy will excite phonons or in other words generate heat. There are several ways how high energy electrons can damage a sample or at least change its properties, as for example electron beam induced defect electromigration [141], ionization damage, deposition of hydrocarbons or local sample heating [142–144]. The energy dependent effects of electron irradiation, already reported for GaAs/AlGaAs 2DEG structures, affect the mobility and carrier concentration as confirmed by transport measurements [145]. Similar observations were reported in a photoluminescence study in GaAs/AlGaAs quantum wells [146, 147]. It should be noted that almost no damage was observed below 5 kV or above 15 kV[10] [145, 146]. The most likely damage for the HgTe/HgCdTe system originates

[10]scanning a 100×100 nm spot at 10 kV on a HgTe/HgCdTe substrate deposits enough energy to create a visible surface degradation while the same experiment for 2.5 kV or 30 kV does not.

from local heating. The maximum rise in temperature from an incident electron beam can be roughly estimated using the following equation

$$\Delta T = \frac{4.8 E_0 b_\mathrm{i}}{k d_0}, \tag{4.4}$$

where E_0 is the electron energy, b_i is the beam current, k the thermal conductivity of the specimen and d_0 the beam diameter [148, 149]. Using Eq. 4.4 and typical settings for e-beam writing like $E_0 = 30$ keV, $b_i = 1$ nA, the typical thermal conductivity of the substrate material CdTe of $k = 0.062$ Wcm^{-1}K^{-1} [150] and a beam diameter of 0.01 µm at the focus point, the calculated maximum temperature increase ΔT is approximately 232 K. HgTe, however, is already extremely sensitive to heating above 80°C. Changing the settings to $E_0 = 2.5$ keV and $b_\mathrm{i} = 0.1$ nA leads to an estimated maximum rise in temperature of only 2 K. Low energy electrons do not penetrate into the QW region, while high energy electrons usually dissipate most of their energy deeper in the substrate. The real increase in temperature, however, will be smaller than these calculated values, as HgTe/HgCdTe heterostructures consist of multiple layers of different carrier densities, that consequently exhibit different thermal conductivities.

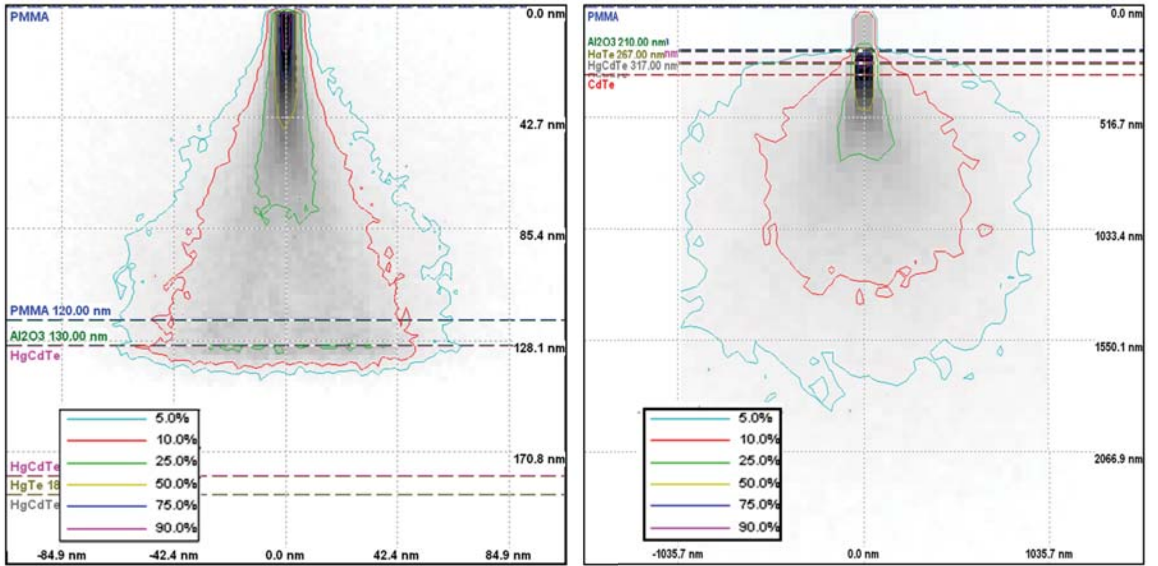

Figure 4.30.: *Energy distribution by position for a* 2.5 kV *electron beam and* 120 nm *PMMA (left) and for a* 30 kV *beam and* 200 nm *PMMA (right). Note the difference in spatial extent by an order of magnitude. The simulation was performed using the software CASINO [152].*

Thermocouple experiments done by Ref. [151] show a strong substrate dependence and also demonstrate the dependence of temperature rise on the exposure time, which is not accounted for in Eq. 4.4. Typical dwell times during PMMA exposure are in the order of a few 100 ns per spot, corresponding to an exposure dose in the range of a few (10 to 1000) $\mu C/cm^2$. For a typical exposure dose of 150 $\mu C/cm^2$ and E_0=15 keV, Ref. [151] reports a measured increase of temperature on a quartz substrate of approximately 63 K. Depending on the initial electron energy, the heat will be dissipated in a different interaction volume, as the penetration depth of the electrons increases with acceleration voltage. This is relevant for varying quantum well depths in heterostructures. In order to demonstrate the energy distribution by position in a typical HgTe/HgCdTe heterostructure, as to be expected from an incident 10 nm electron beam, we performed classical Monte Carlo Simulations using the software CASINO [152]. For that purpose the trajectories of 10^4 electrons were simulated for a 2.5 kV and 30 kV electron beam. The exemplary sample consists of 50 nm HgCdTe, 7 nm HgTe (QW), 50 nm HgCdTe and CdTe as substrate material. To simulate the e-beam writing conditions, we added a 10 nm Al_2O_3 sacrificial layer plus a 120 nm PMMA layer for 2.5 kV and a 200 nm PMMA layer for 30 kV onto the cap layer. The results are shown in Fig. 4.30. Dark colored areas display regions with high energy absorption. The colored lines indicate the amounts of energy not contained within the area. For the 2.5 kV beam between 75% to 90% of the energy is absorbed within the PMMA and sacrificial layer and only a small fraction of the electrons reaches the cap layer. Note that no electrons penetrate through the quantum well. For the 30 kV process most of the energy is dissipated within the actual layer stack, including the quantum well, and only partly absorbed by the covering PMMA resist, as visible from the lighter grey color. Compared to 2.5 kV, the penetration depth for a large fraction of electrons increases by at least an order of magnitude. As we cannot rule out the degradation of the sample during the beam writing process, low acceleration voltages reduce the possible heat load for the sensitive QW as much as possible.

Low-energy electron beam lithography has already been developed two decades ago [153] as a possible alternative to avoid the necessary proximity correction for high density patterning. Because of the scattering characteristics of the electrons at small acceleration voltages the proximity effect is significantly reduced. In addition, the necessary exposure dose is often an order of magnitude smaller than in a 30 kV or 50 kV process [153]. The disadvantage of low acceleration voltages lies in the limited reso-

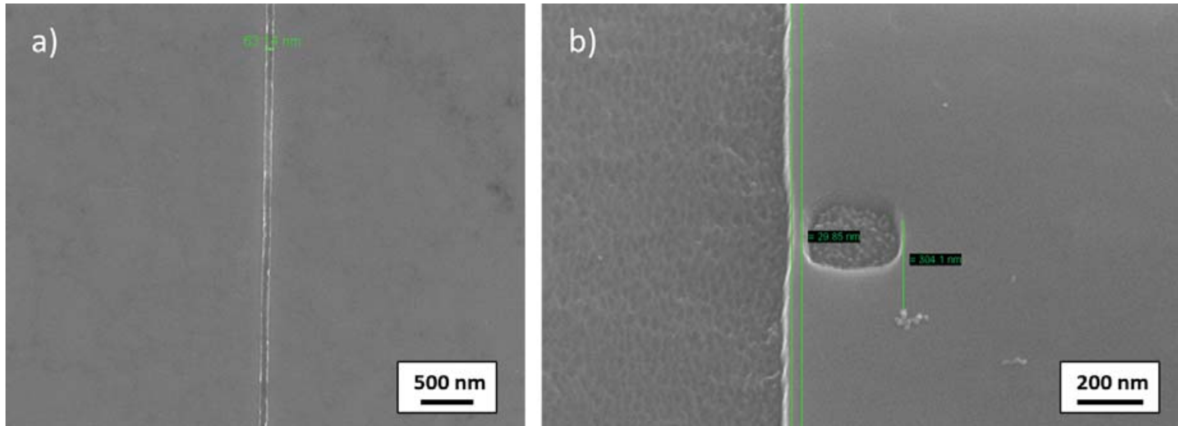

Figure 4.31.: *a) SEM micrograph of an evaporated* 15 nm *thick Ti line, structured on a FEI Nova NanoSEM 450 at* 2.5 kV, 30 μC/cm^2 *in* 120 nm *950k PMMA. b) SEM micrograph of an ion milled* 300 nm *hole, separated from the mesa edge by a* 30 nm *strip, structured on a Zeiss Leo1525 at* 2.5 kV, 50 μC/cm^2 *in* 120 nm *950k PMMA.*

lution caused by the strong scattering within the resist. In addition, despite the low necessary dose, exposure times increase because of the reduced beam current associated with lower acceleration voltages. Reference [153] demonstrates a resolution down to 30 nm in a 45 nm thick single layer 360K PMMA resist and a 70 nm 150K/360K double layer resist, both exposed at 2 kV. Thinner resist layers yield a better resolution but are less suitable for lift-off techniques or to serve as etch masks. In our experiments we used a 120 nm 950K single layer PMMA, exposed at 2.5 kV, using a Zeiss Leo 1525 equipped with a Raith Elphy Plus pattern generator. The process was also successfully transferred and evaluated on a FEI Nova NanoSEM 450. Typical exposure doses range between 30 μC/cm^2 and 60 μC/cm^2 depending on the desired feature. Despite the slightly larger acceleration voltage and the increased resist thickness compared to [153], we were able to generate 60 nm isolated features and 30 nm in proximity to larger exposed areas. Figure 4.31 a) shows an isolated 60 nm wide Ti line, Fig. 4.31 b) demonstrates a 300 nm etched hole structure separated by a 30 nm wide strip from the mesa edge. Both structures were written using a positive process. Note that no proximity correction was applied to generate these features. Although the resolution does not exceed the results of Ref. [153], the increased resist thickness allows to evaporate and lift-off metal layers up to a thickness of 90 nm. A possible application for features as small as 30 nm is the lithography of thin contact lines to HgTe nano wires.

In summary it can be stated that low energy lithography provides a more than sufficient resolution to generate precise etch masks, thin gate structures and contact lines while minimizing the risks of possible thermal sample damage. This process therefore reliably served as the standard e-beam lithography method for many successful HgTe experiments [14, 31, 123, 154, 155].

4.4. Airbridges

Motivation

Metallic air bridges, fabricated using e-beam lithography, offer various applications. Such structures have been used in the past e.g. as gatepost contacts for parallel QPCs on GaAs/AlGaAs 2DEGs [156] and as suspended gates on graphene [157], but also as switches in microelectromechanical systems (MEMS) [158, 159] and contacts in mm-wave applications [160]. As demonstrated by Hinz *et al.* [8] and confirmed in various of our measurements, HgTe/HgCdTe QW structures exhibit hysteresis effects[11] in the charge carrier density of the QW for large positive and negative gate voltages. These hysteresis effects are attributed to charging and discharging of states at the SiO_2/Si_3N_4 semiconductor interface. Comparable observations were made for various insulator materials such as Si_3N_4, SiO_2 and Al_2O_3. Using the example of a micro Hall bar, we tried to implement suspended air bridges as gate structures, rendering the use of additional insulating layers unnecessary and leaving the sample surface with its natural oxide. The feasibility and possible differences in transport measurements compared to classical topgates are studied.

Fabrication

Two different fabrication techniques are common to generate suspended metal bridges. The first and most conventional method involves the control of the electron dose during e-beam exposure, using multilayer resist systems with varying sensitivities to create the desired profile for the supporting pillars and the span [156, 157, 159, 161]. For this process a precise dose control and correction of the proximity effect is necessary. We chose the second approach [159, 162], controlling the electron energy and thus

[11]HgTe bulk layers, covered with the same insulators and classical topgates do not exhibit these hysteresis effects.

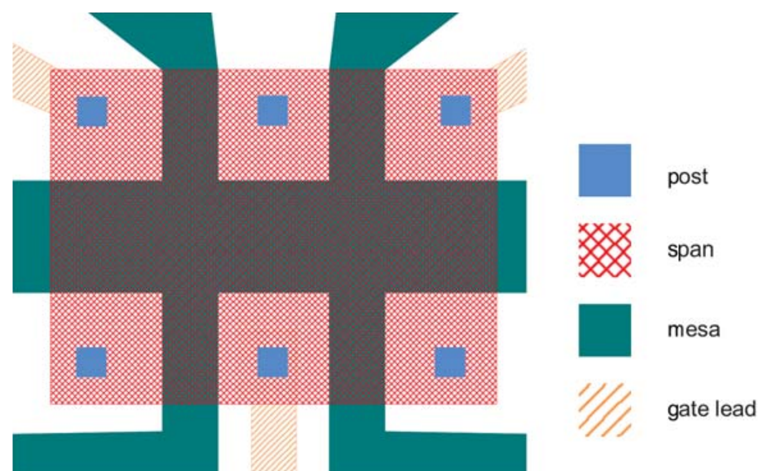

Figure 4.32.: *Schematic of the different e-beam exposure layers for a micro Hall bar with airbridge gate.*

the penetration depth into the resist by adapting the acceleration voltage. Adapting the process described in Ref. [162] for low temperature lithography, it is possible to prevent the underlying QW from damage due to high energy electron exposure. Unlike for graphene, the mesa height can be of several (10 to 100) nm making fabrication difficult as posts and bridge may be located on different levels.

The procedure is divided into several exposure steps to generate the Hall bar mesa, the gate leads, the conducting posts and the span. The different layers are schematically illustrated in Fig. 4.32. The pillars and the span can be exposed and metalized in a single e-beam writing/evaporation iteration or split into two exposure and deposition steps, if necessary[12]. First the Hall bar mesa is defined in either a positive or negative hard mask lithography process, as illustrated in Chapter 4.2.3 using 2.5 kV lithography and Ar^+ ion milling. In a second 2.5 kV exposure step, gate leads are defined within the etched areas, consisting of 5 nm Ti as adhesion promoter followed by 50 nm of Au. In order to guarantee a stable distance between gate span and mesa a flat resist surface is required. In order to level the sample topography and to gain the necessary resist height we apply four layers of 950K PMMA resist. The first two layers consist of 950K 3% dissolved in ethylene glycol, spun at 5000 rpm for 40 s. The low concentration supports the leveling of mesa and resist surface because of the reduced viscosity of the

[12]Dividing the process yields more precise gate spans but is significantly costlier and time consuming.

solution. The third and fourth layer consist of 950K 5% dissolved in ethylene glycol, spun at 6000 rpm for 40 s. The use of a higher concentration adds the necessary resist height. The layers are applied sequentially, each coating followed by a 2 min PAB at 80°C. The final bake is conducted at 70°C for 20 min to reduce the residual solvent concentration within the layer stack. Note that the exposure sensitivity is the same for all layers, thus acting as one thick layer of 950K during exposure.
The final resist height generated by this procedure is approximately 1.2 μm. The exact thickness can vary slightly depending on chip size and geometry. As it is crucial for the process, the exact PMMA height is measured prior to the exposure of posts and span. For this purpose we expose and develop a reference window ($\approx$ 80 μm $\times$ 80 μm) close to the actual structure in the etched part of the substrate. The acceleration voltage for this process is 30 kV and the dose 600 μC/cm^2. We develop 4 min in a mixture of AR-600-56 : IPA in a ratio of 1 : 1 and rinse 10 s with IPA and 120 s DI water afterwards. Under the premise that the reference window is exposed in the homogeneously coated part of the chip it can be assumed that deviations from the actual resist height at the device site are in the order of only a few nm. The resist height is determined by scanning over the exposed window with a stylus-profilometer. During the same exposure step it is reasonable to open global and local alignment marks as they are barely visible at the low acceleration voltages used to expose the span. The posts are also exposed at 30 kV but with a smaller aperture to retain a high depth of focus. The dose for theses structures is increased to 1000 μC/cm^2. This is necessary as the proximity effect becomes more pronounced for high acceleration voltages. Backscattered and secondary electrons add up to the total exposure dose. For very small columns and thick resist layers the initial dose therefore has to be higher to account for the missing proximity dose. The gate span is exposed with a dose of 500 μC/cm^2. The acceleration voltage depends on resist thickness, mesa height and desired spacing between gate and mesa and can be extracted from Fig. 4.33. There the measured depth into the PMMA layer is displayed as a function of electron energy and for different exposure doses. For example for a resist thickness of 1.2 μm, a mesa height of 100 nm and a desired gap between mesa and gate of 100 nm the electrons have to expose the resist down to a depth of 1000 nm, corresponding to an acceleration voltage of approximately 6.5 kV. The exposed resist is then developed as described for the reference window. To yield better results for small columns with a high aspect ratio, the development process can be enhanced by adding some agitation using short

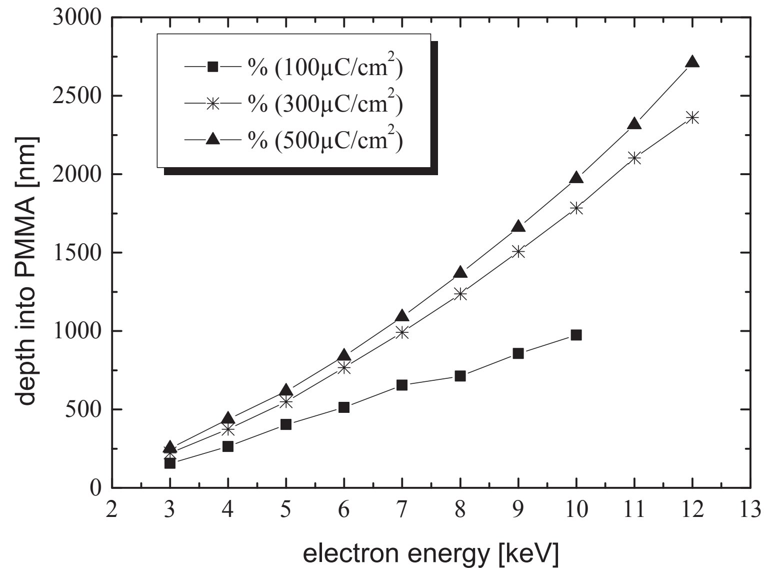

Figure 4.33.: *Measured depth into PMMA as a function of electron energy and different exposure doses. From Borzenko et al. [162].*

ultrasonic treatment. After the development the sample is exposed for a few seconds to an O_2 plasma to ensure the complete removal of organic residues at the bottom of the exposed pillars. This step significantly improves the contact between gate leads and posts. In a final fabrication step the metal for the gate structure is evaporated. After 5 nm of Ti as adhesion promoter we evaporate between (300 to 400) nm of Au. The minimum metal thickness depends on the sum of the mesa height and the desired gap to the gate, plus an overlap between post and span. The maximum metal thickness is limited by the difference of the total resist thickness and the sum of mesa height and gap. The residual resist and metal are removed in an acetone lift-off.
The final result is displayed in two SEM micrographs in Fig. 4.34. The yellow colored areas include gate leads, conducting posts and the span. Blue shaded areas depict the mesa. The distance between gate and mesa is clearly visible in these pictures.

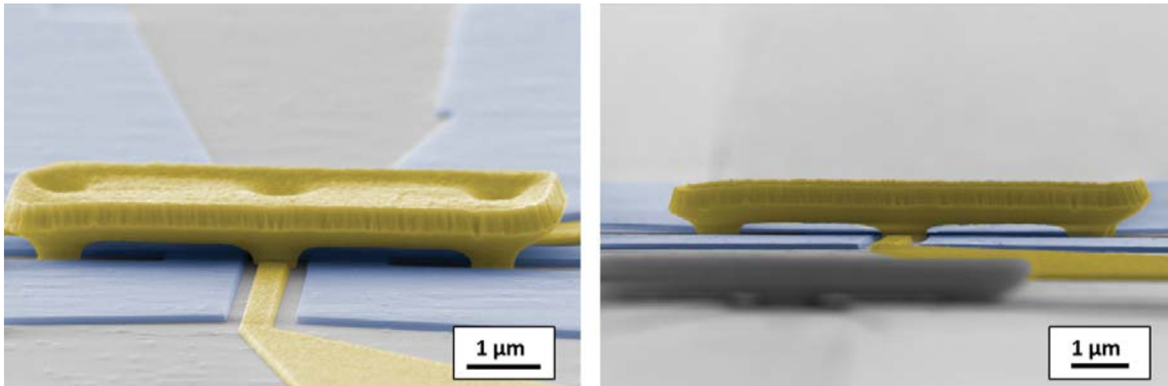

Figure 4.34.: *Colored SEM micrographs of an actual bridge over a micro Hall bar. Yellow areas mark gate leads, conducting posts and span, blue shaded areas depict parts of the underlying mesa. The distance between the mesa and the span is clearly visible.*

Measurements

The presented measurements were conducted on 2 µm wide and 3 µm long micro Hall bars. Figure 4.35 shows a measurement of the Hall resistance as a function of the magnetic field and for different gate voltages. Interestingly the observed carrier density strongly deviates from the values determined on a macroscopic Hall bar of the same wafer Q2391. While the reference structure exhibits n-conducting behavior and a corresponding density of $n = 3.38 \cdot 10^{11}$ cm^{-2} at 0 V, the micro Hall bar exhibits p-conduction[13] and an estimated charge carrier density of $n = -0.04 \cdot 10^{11}$ cm^{-2}. Increasing the applied airbridge gate voltage to positive values raises the density to $n = 1.17 \cdot 10^{11}$ cm^{-2}. Similar observations have been made for macroscopic Hall bars without any gate. It appears that the fabrication of an insulator and a gate directly onto a heterostructure results in an increased n-type carrier density. As a cause, the insulator deposition process itself can be ruled out as for both structures the lithography involves the deposition of a thin insulator as a sacrificial layer for the hard mask. Figure 4.36 shows the four terminal resistance R_{xx} as a function of applied gate voltage. After an initial measurement from 0 V to 2.2 V the curves stabilize at two different paths for up and down. A slight hysteresis can be observed between the curves. The measurement suggests a good gate response despite the rather large distance between gate and 2DEG and the low dielectric constant of liquid Helium of approximately 1.05 [163], compared to 3.9 for a pure SiO_2 [164] layer. Figure 4.37 shows three sequential measurements

[13]Negative carrier densities correspond to p-conduction, positive carrier densities to n-conduction.

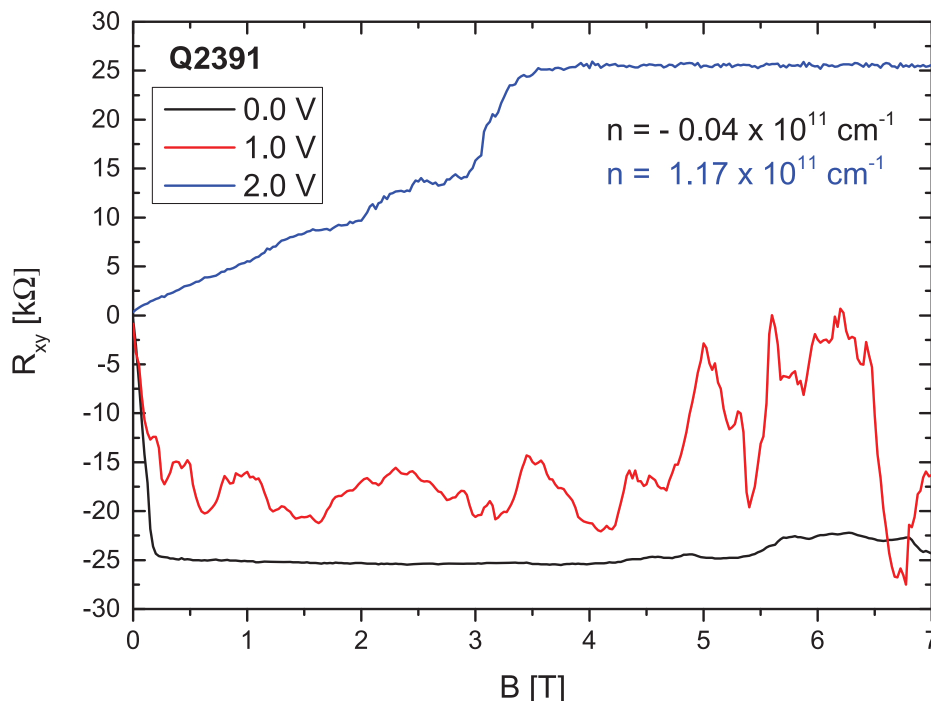

Figure 4.35.: *Hall resistance R_{xy} of a micro Hall bar at $T = 4\,\mathrm{K}$ and for different airbridge voltages, as a function of magnetic field B.*

of the same device. The blue curve in Fig. 4.37 displays the measurement from 2.2 V to 0 V in 1 mV steps. The black curve shows a measurement from 0 V to −2 V with an increased step size of 5 mV. The red curve displays the return measurement from −2 V to 2.2 V in 5 mV steps. The observed path difference strongly deviates from the hysteresis studied by Hinz *et al.* [8] on similar HgTe/HgCdTe heterostructures covered with SiO_2 and Si_3N_4 insulating layers. Similar observations were made on a comparable device on a different wafer Q2389. Figure 4.38 displays two sequential measurements of the longitudinal resistance R_{xx} as a function of airbridge voltage. Both resistance characteristics show a maximum in resistance within the applied gate voltage range. A slight deviation between both signatures is observed. It should be noted that for some structures a delayed gate influence on the 2DEG was observed. For these samples the measured contact resistances between gate lead and the conducting posts were in the order of several kΩ. The reason for this high resistance is most probably residual PMMA resist at the bottom of the developed openings for the conducting posts. A

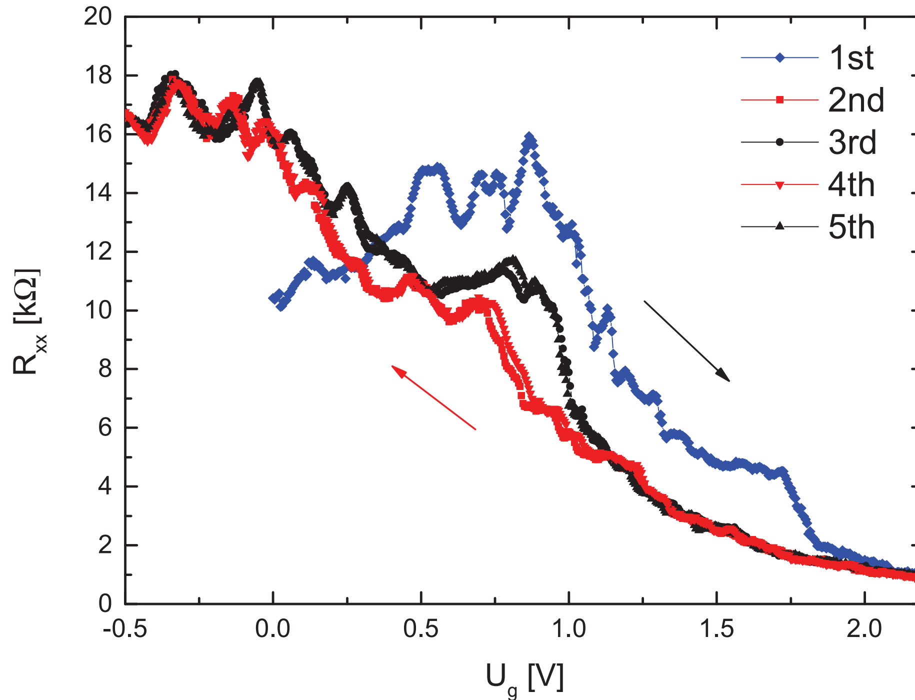

Figure 4.36.: *Four terminal resistance R_{xx} as a function of gate voltage in the range from -0.5 V to 2.2 V. After the initial measurement (blue) from 0 V to 2.2 V the curves stabilize at two different paths for up (black) and down (red).*

clean development of these openings is challenging due to their high aspect ratio. This organic contamination is then covered in the subsequent metal evaporation step and forms a highly resistive layer between lead and gate. However, the residue can be avoided with a short O_2-plasma ashing process prior to the evaporation. It should also be noted that the interface of Au and TiO_2 exhibits diode behavior [165], which could also be responsible for delayed charge balancing in case the evaporated Ti adhesion layer between lead and post is contaminated with an oxide.
In order to estimate the charging times for our gate electrodes we approximated the structure using a simple plate capacitor model. The capacitance of the electrode is calculated using the equation

$$C = \frac{\varepsilon_0 \cdot \varepsilon_\mathrm{r} \cdot A}{d}, \tag{4.5}$$

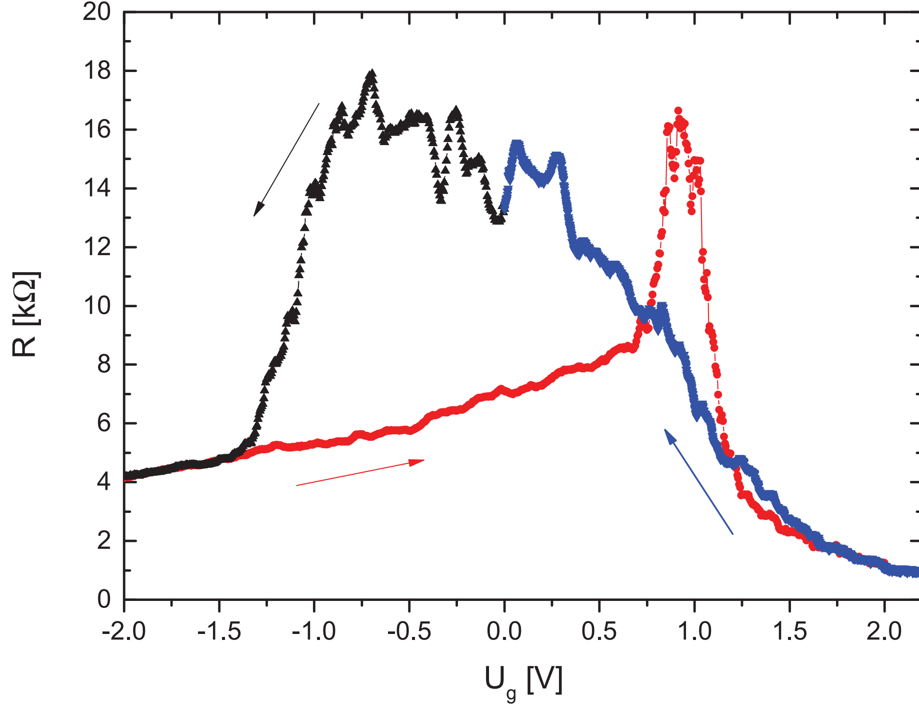

Figure 4.37.: *Four terminal resistance R_{xx} as a function of gate voltage. The measurement is divided into three separate measurements. blue: 2.2 V to 0 V in 1 mV steps, black: 0 V to −2 V in 5 mV steps, red: −2 V to 2.2 V in 5 mV steps. Arrows indicate the measurement direction.*

where $\varepsilon_0 \approx 8.854 \times 10^{-12}$ F/m is the vacuum permittivity, ε_r is the relative permittivity of the insulator, A is the gate area and d is the distance between the gate and the QW. In case of airbridges the space between the QW and the gate consists of a stack of two different dielectrics. The first dielectric is the space between the span and the cap layer, the second one is the cap layer itself. During the measurement the space between gate and cap layer is filled with He with a dielectric constant $\varepsilon_\mathrm{space}$ of approximately 1.0 over the whole temperature range [166]. According to Ref. [167], the static dielectric constant of $\mathrm{Hg}_{1-x}\mathrm{Cd}_x\mathrm{Te}$ is calculated as

$$\varepsilon_r = 20.5 - 15.6x + 5.7x^2. \tag{4.6}$$

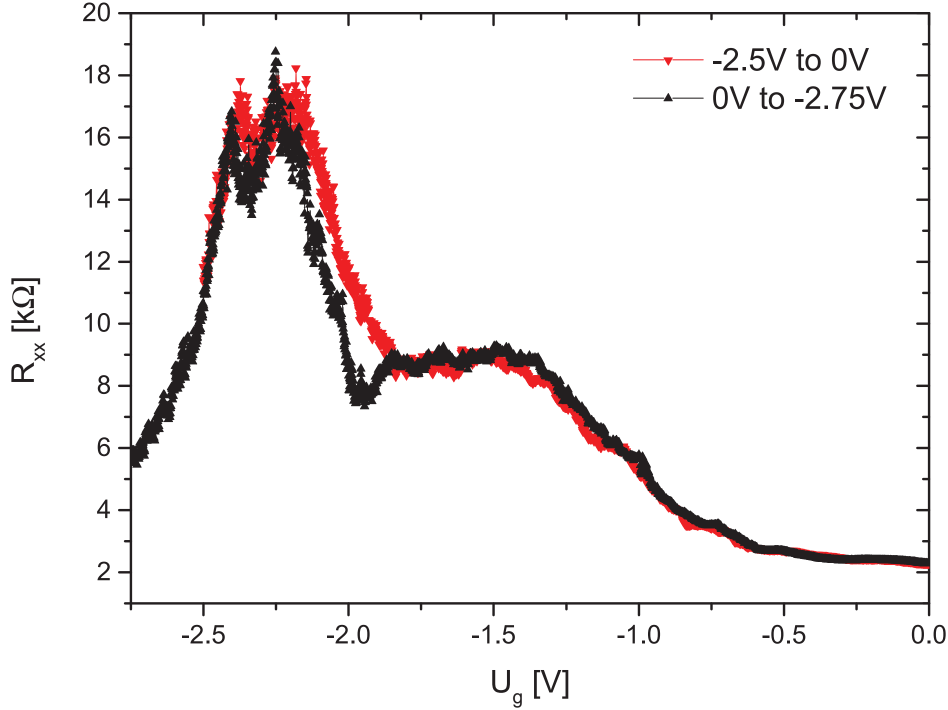

Figure 4.38.: *Two sequential measurements of the four terminal resistance R_{xx} as a function of gate voltage on a second device on a different wafer Q2389.*

For our barrier composition with $x = 0.7$ we obtain $\varepsilon_{\text{cap}} \approx 12.4$. The capacitor area A is approximately $(10 \times 10)\ \mu\text{m}^2$, and the distances are $d_{\text{space}} \approx 100$ nm and $d_{\text{cap}} = 25$ nm. The total gate capacitance is therefore in the order of a few femtofarad. The charging time of the gate depends on the resistance R of the gate lead and the capacitance C of the gate. The time dependent voltage $U(t)$ applied at the gate is calculated by

$$U(t) = U_0(1 - e^{-t/\tau}), \tag{4.7}$$

with the RC time constant $\tau = R \cdot C$ and the external source voltage U_0. Figure 4.39 exemplary shows calculations for $U(t)$ for different gate lead resistances R up to 1 MΩ, a source voltage U_0 of 0.1 V and a gate capacitance C of 8.67 fF. The graph demonstrates how the charging time depends on the gate contact resistance. Even for a highly resistive interface between the leads and the gate, with a theoretical resistance value in the order of gigaohm, the charging time to reach the applied gate voltage between each

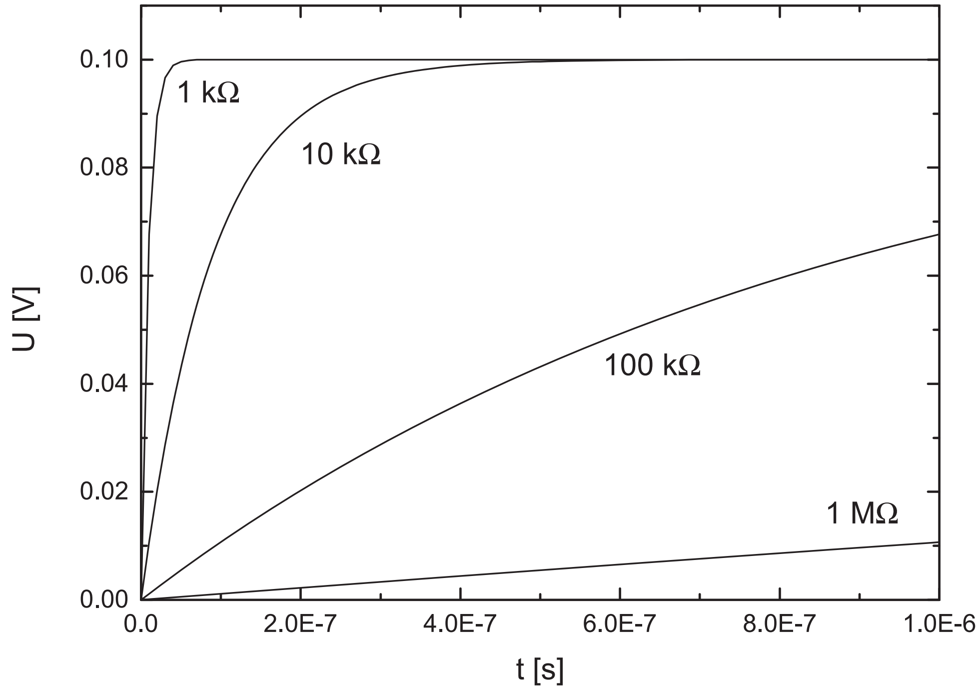

Figure 4.39.: *Charging of the gate from* 0.0 V *to* 0.1 V *as a function of time with an applied source voltage* U_0 *of* 0.1 V *and for different resistances.*

measurement step does not exceed a few milliseconds. Consequently slow charging of the gate cannot account for the delayed gate response observed in certain measurements.

A possible explanation for anomalous gate response could be the deflection of the bridge due to the electrostatic force between span and cap layer, which is building up during the gating. This effect is utilized in MEMS where airbridge cantilevers function as switches [168, 169]. A reduction of the space between gate and cap layer would lead to a significant increase of the gate capacitance of up to almost two orders of magnitude in the discussed example. Again, we can approximate the attractive force F that acts on the gate span using the plate capacitor model with two dielectrics, where

$$F = \frac{\varepsilon_0 \varepsilon_{\text{space}} \varepsilon_{\text{cap}}^2 U^2 A}{2(\varepsilon_{\text{cap}} d_{\text{space}} + \varepsilon_{\text{space}} d_{\text{cap}})^2}. \tag{4.8}$$

In our system the electrostatic force therefore may reach values up to 10^{-6} N within the applied voltage range, and is comparable to values observed e.g. in electrostatically actuated microswitches [169]. It may be possible that the span touches the surface of the heterostructure for larger gate voltages and recovers after the voltage is decreased again. Microswitches as presented in Ref. [169] are able to survive multiple switching cycles without degradation. No damage of our airbridge structures was observed after several gate voltage dependent measurements. However, the scenario of a bent gate span should be considered in future experiments.

Summary

Our measurements demonstrate the controllability of the carrier density in HgTe/HgCdTe QW structures by applying a voltage to airbridge gates and without the need of an additional insulating layer. Our measurements support the model by Hinz *et al.* [8] that the observed hysteresis in normal gated devices originates from charging at the interface between SiO_2/Si_3N_4 and the HgCdTe cap layer. However, our measurements exhibit a different hysteresis effect which should be studied further. It should be noted that the absence of the insulator also has an effect on the intrinsic carrier density. Nevertheless airbridges exhibit a good gate influence and pose an interesting alternative to classical gating especially for wafer with a high intrinsic electron density that so far prevented to observe the QSH effect within the hysteresis free gate voltage range.

5. Weak antilocalization

We study the weak antilocalization (WAL) effect on the magnetoresistance of narrow HgTe wires fabricated in quantum wells (QWs) with normal and inverted band ordering. To obtain these measurements we integrated several of the described low temperature and low energy lithography techniques of Chapter 4 into the fabrication process. The measurements benefit from the improved comparability of macroscopic and nano-devices. As the wire geometry is very susceptible to alterations of the mesa surface and sample walls, the developed hardmask lithography guarantees pristine separated structures and thus a stable gate influence. The results are published in *Phys. Rev. Lett.* **112**, 146803, (2014).

5.1. Introduction

Weak anti-localization (WAL) is a quantum transport effect that occurs in electronic systems with broken spin rotation symmetry. It is associated with spin precession along closed electron trajectories, which leads to a reduced backscattering and, in materials with sufficiently strong spin-orbit interaction (SOI), to an observable positive magnetoresistance [170]. While in semiconductors with a parabolic band dispersion, WAL results from the Rashba or Dresselhaus SOI (see e.g. [170, 171]), Suzuura and Ando suggested that the WAL may also occur in materials with a Dirac-like band dispersion, e.g. such as a two-dimensional (2D) honeycomb lattice [172]. In such systems, carrier backscattering is suppressed due to the topological Berry phase of carriers at the Fermi energy. However, in graphene, the first Dirac material to be extensively studied experimentally [173], the band-structure induced WAL effect is obscured by a competing weak localization (WL) effect (see e.g. Refs. [174, 175]) due to intervalley scattering [176]. In narrow graphene wires, this latter scattering mechanism is ubiquitous due to edge roughness, which explains the absence of WAL in recent transport measurements [177] and numerical simulations [178] for graphene nanoribbons. As topological

effects in transport physics are in the focus of current research, it is of great interest to examine the quasi-1D localization properties of other novel materials exhibiting a Dirac-like band structure. In this work we study quantum transport in nanowires fabricated from HgTe quantum wells. HgTe QWs with thicknesses d larger than a critical value d_c exhibit an inverted band structure, which gives rise to the quantum spin Hall insulator state, characterized by gapless one dimensional Dirac-like helical edge states, when the Fermi energy is in the bulk gap [13, 14], as described in detail in Chapter 2. Here, we are interested in the transport properties of the bulk conduction band states. HgTe QWs with a thickness close to d_c have a very small gap and the conduction band structure exhibits a Dirac-like dispersion, as found in band-structure calculations and verified by transport experiments [27, 179] and magneto-optical [180, 181] observations. The band structure of the 5 nm and the 7 nm HgTe QWs is deduced from $\mathbf{k}\cdot\mathbf{p}$ calculations based on a numerical code developed in previous studies (see e.g. [27]). The results of these calculations for the lowest-energy s-like, E1, and p-like, H1, subbands are shown in Fig. 5.1 (colored solid lines). The 5 nm QW has a normal band ordering with E1 energetically higher than H1, whereas the band structure of the 7 nm QW is inverted i.e., H1 and E1 have swapped their role as conduction and valence band. Insight into the band structure of the HgTe QWs can be gained from the four-band model derived in the vicinity of the $k = 0$ point by Bernevig, Hughes and Zhang (BHZ) [13]. We use the BHZ Hamiltonian in the following representation:

$$\hat{H} = s_z \boldsymbol{\sigma}(\mathcal{A}\mathbf{k} + \mathcal{M}_\mathbf{k}\mathbf{z}) + \mathcal{D}\mathbf{k}^2, \qquad \mathcal{M}_\mathbf{k} = \mathcal{M}(d) + \mathcal{B}\mathbf{k}^2. \tag{5.1}$$

In this equation the linear term (proportional to wave vector $\mathbf{k}$ and constant $\mathcal{A}$) describes the hybridization of the s-like, E1, and p-like, H1, QW subbands. The two subbands are represented by the pseudospin $\boldsymbol{\sigma}$, whose components σ_x, σ_y and σ_z are 2×2 Pauli matrices. The real spin degree of freedom enters through the Kramers partner states represented by Pauli matrix s_z. The effective Dirac mass $\mathcal{M}_\mathbf{k}$ arises from the band gap, $|\mathcal{M}_{\mathbf{k=0}}| = |\mathcal{M}(d)|$, which is determined by the nominal QW thickness d. The $\mathbf{k}$-dependent contribution to $\mathcal{M}_\mathbf{k}$ (i.e. the quadratic $\mathcal{B}\mathbf{k}^2$ term) and the parabolic background $\mathcal{D}\mathbf{k}^2$ account for the deviation of the realistic QW band dispersion from the simple massive Dirac spectrum. The eigenvalues of Hamiltonian (Eq. 5.1) are

$$E_s = \mathcal{D}\mathbf{k}^2 \pm \sqrt{\mathcal{A}^2\mathbf{k}^2 + (\mathcal{M} + \mathcal{B}\mathbf{k}^2)^2}, \tag{5.2}$$

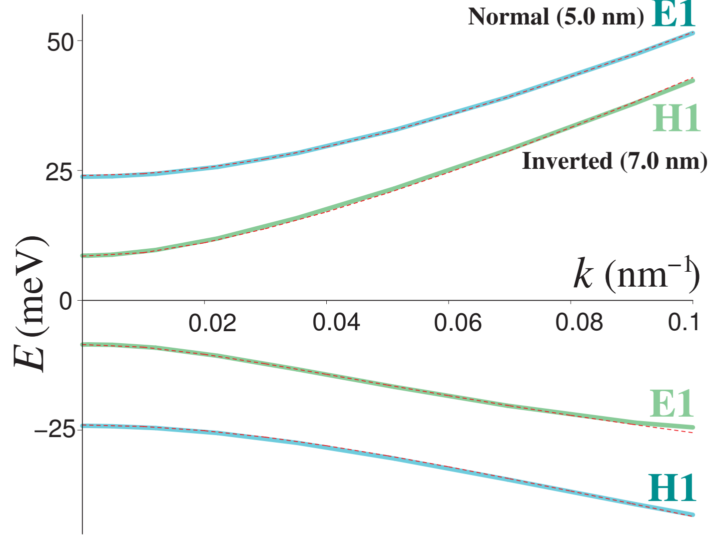

Figure 5.1.: *Energy, E, of the lowest s-like, E1, and p-like, H1, subbands versus wave number k for a 5 nm (normal) and a 7 nm (inverted) HgTe quantum well. The thick lines are obtained from $\mathbf{k}\cdot\mathbf{p}$ calculations, while the thin (dashed) lines are results of the Bernevig-Hughes-Zhang (BHZ) model, Eqs. (5.1) and (5.2).*

where $\pm$ corresponds to the conduction and valence bands, respectively. The energy bands are double degenerate with respect to the eigenvalues $s = \pm 1$ of s_z. Fitting the $\mathbf{k}\cdot\mathbf{p}$ calculations by Eq. (5.2) [see thin (red) dashed lines in Fig. 5.1], we obtain the BHZ parameters $\mathcal{M}$, $\mathcal{A}$, $\mathcal{B}$ and $\mathcal{D}$ listed in Tab. 5.1. The fits are satisfactory up to $k \approx 0.1$ nm^{-1}, which is the usual accuracy of the BHZ model. In contrast to graphene, HgTe QWs have only a single Dirac-like valley, so that intervalley scattering is absent, with obvious advantages for studying quantum interference effects of Dirac fermions. Therefore, in narrow wires on HgTe QWs a clear WAL effect is observable.

Table 5.1.: *Thickness d and band structure parameters $\mathcal{M}$, $\mathcal{A}$, $\mathcal{B}$ and $\mathcal{D}$ for the inverted and non-inverted HgTe QWs used in our experiment.*

d [nm]	$\mathcal{M}$ [meV]	$\mathcal{A}$ [eV · nm]	$\mathcal{B}$ [eV · nm^2]	$\mathcal{D}$ [eV · nm^2]
7	-8.5	0.34	0.5	0.87
5	24	0.365	0.5	0.5

5.2. Experiment

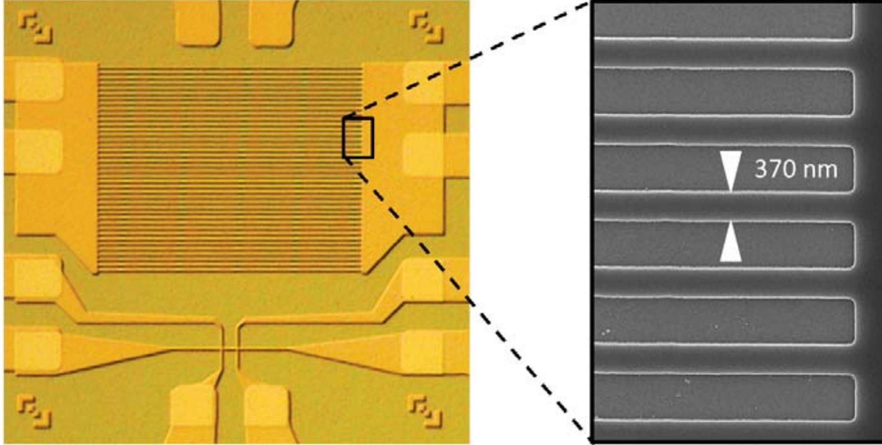

Figure 5.2.: *Micrograph of the sample mesa with 40 parallel* 50 µm *long wires with a width of approximately* 0.37 µm.

We present experimental results on samples fabricated on two different QW structures. The structures were grown by molecular beam epitaxy on insulating CdTe and CdZnTe substrates with nominal QW thicknesses of 5 nm ($< d_c$) and 7 nm ($> d_c$), respectively, thus exhibiting a normal and an inverted band ordering. The HgTe QWs are embedded between thick $Hg_{0.3}Cd_{0.7}Te$ barriers. The 7 nm QW sample is additionally doped with iodine in the bottom barrier at a distance of 70 nm. The layers have been patterned by low temperature and low energy optical and electron beam lithographical techniques into (30 × 10) µm^2 Hall bars (for characterization purposes) and into an array of 40 parallel wires for the quantum interference investigations. The comparability between optically and electron beam defined structures is ensured by using the non-invasive 2.5 kV lithography process described in Chapter 4.3. With this process, even for dense pattern like the wire array, no proximity correction was necessary to achieve a reliable lift-off and keep the correct wire dimensions. In order to get reliable results and extract the correct WAL signal it is crucial that all wires are perfectly separated from each other and have the exact same length and width. Furthermore the optimized hard mask process described in Chapter 4.2.3 ensures that the material properties like carrier density and mobility are not affected by the lithography. Additionally, the mesa design was optimized to ensure that the serial resistance was kept at a minimum for

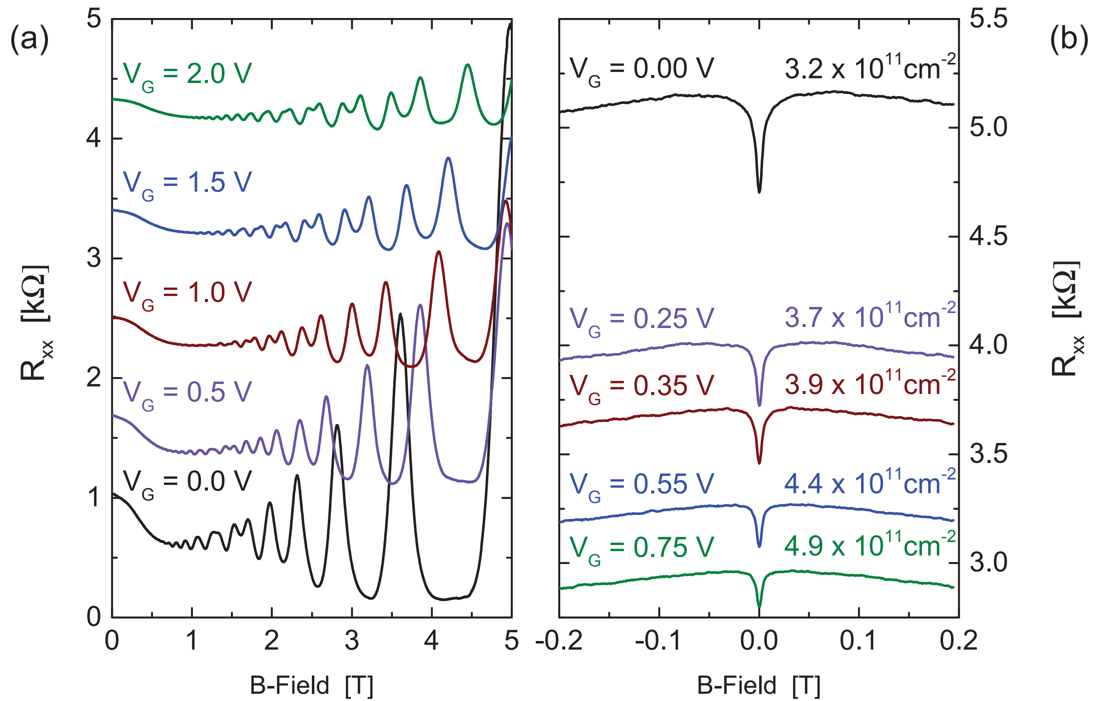

Figure 5.3.: *Magnetoresistance ($d = 7$ nm), $R_{xx}(B)$, of (a) a macroscopic Hall bar with (30×10) μm^2 and (b) 40 parallel wires with (50×0.37) μm^2 area for different gate voltages V_G. For clarity, the traces of Fig. 5.3 a) are displayed with an constant offset of 1 kΩ. The corresponding measured carrier densities are $n = 3.2$, 4.3, 5.4, 6.7, and 7.9×10^{11} cm^{-2} for the indicated gate voltage. For the multiple wire sample of Fig. 5.3 b), the carrier densities are indicated in the figure.*

all wires to minimize possible offsets. By implementing the newly developed AuGe contacting technique it was possible to add additional contacts and a single wire for reference purposes. The wires are 50 μm long and approximately 0.37 μm wide. A micrograph of the wire mesa is given in Fig. 5.2. All device structures are fitted with a Ti/Au gate electrode on a 50 nm thick SiO_2/Si_3N_4 multilayer gate insulator to control the carrier density and the structural inversion asymmetry and thus the Rashba SOI strength. Densities and mobility for the wires have been inferred from the Hall bar structures. By measuring a large number of identical wires in parallel, universal conductance fluctuations are averaged out while non-random quantum-interference effects like the WAL remain. All measurements, except the temperature dependence of the WAL, have been carried out in a ^{4}He cryostat fitted with a superconducting magnet at

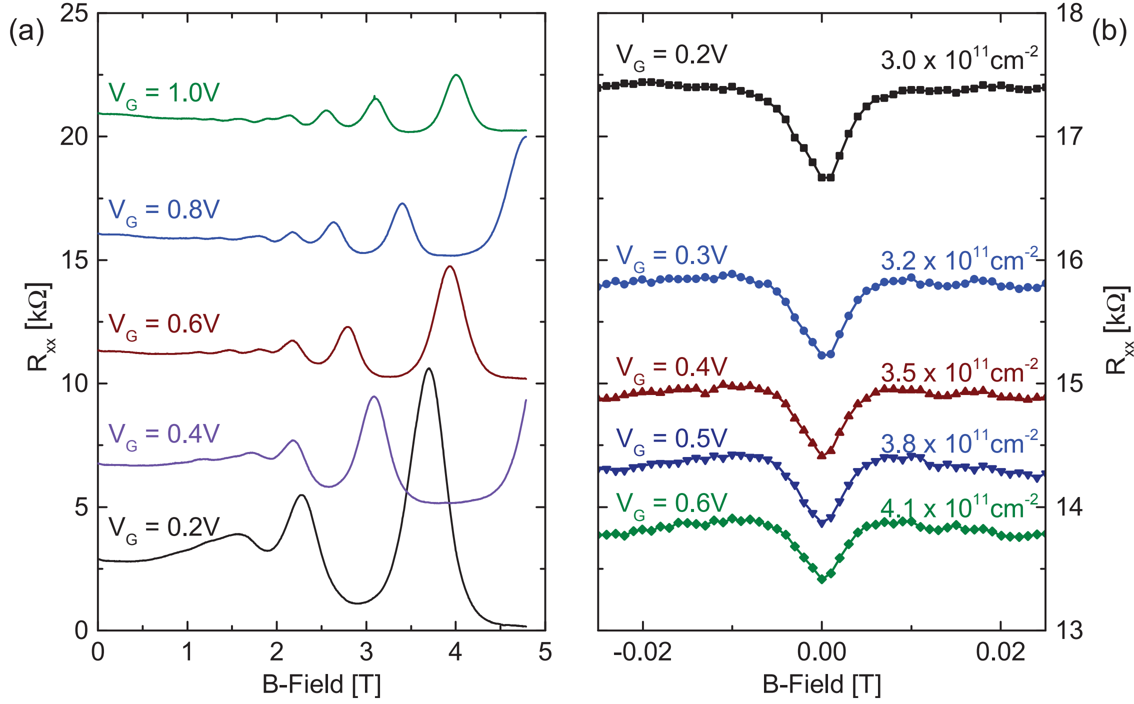

Figure 5.4.: *Magnetoresistance (d = 5 nm), $R_{xx}(B)$, of (a) a macroscopic Hall bar with 600×200 μm^2 and (b) 40 parallel wires with 50×0.37 μm^2 area for different gate voltages V_G. For clarity, the traces of Fig. 5.4 a) are displayed with offsets of 5 kΩ. The corresponding measured carrier densities are $n = 1.4$, 1.9, 2.5, 3.1, and 3.7×10^{11} cm^{-2} for V_G = 0.2, 0.4, 0.6, 0.8 and 1.0 V. For the multiple wire sample, Fig. 5.4 b) the carrier densities inferred from comparable Hall bars are indicated in the figure.*

a base temperature of 1.8 K. Figure 5.3 shows magnetotransport data for the 7 nm QW on a macroscopic Hall bar (a) and the wire sample (b) for five different gate voltages. The first observation is that the wire sample exhibits a sharp resistance dip around $B = 0$ on a smoothly varying parabolic background which we ascribe to the electron-electron correction to the conductivity. The peak height appears to be approximately constant in the presented gate-voltage range (Fig. 5.3 b). The latter is remarkable, since from the oscillations of the magnetoresistance (Fig. 5.3 a) one infers that in this gate-voltage range the Rashba SOI strength is very small, and hardly any beating pattern is observed. From a $\mathbf{k} \cdot \mathbf{p}$-band structure calculation we find the Rashba splitting varies between 1.5 ± 0.5 meV (V_G = 0V) and 0.0 ± 0.5 meV (V_G = 1V) for this parameter range. For a parabolic dispersion, a vanishing Rashba splitting would also

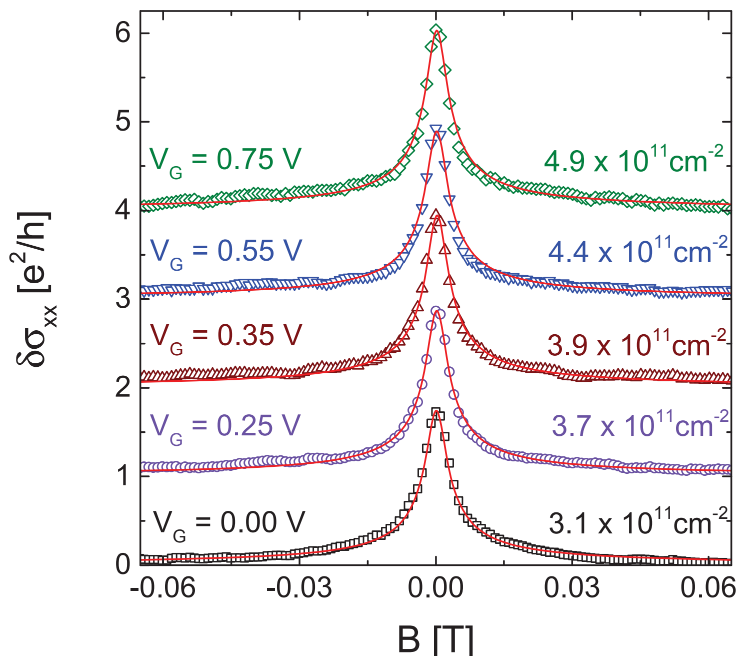

Figure 5.5.: *WAL contribution to the magnetoconductivity, $\delta\sigma_{xx}(B)$, for wires of the 7 nm (inverted) QW at different gate voltages V_g. The thin (red) lines are fits based on Eqs. (5.4) - (5.6). Subsequent curves are shifted by e^2/h for clarity.*

lead to a vanishing WAL signal. Here, however, we observe a strong, nearly unchanged, WAL amplitude over the entire density range. This WAL signal, which is obviously not related to the Rashba spin-orbit splitting, is the prime observation. Similar behavior, but a much smaller WAL amplitude is observed for the 5 nm QW. Figure 5.4 shows the magnetotransport data of the non-inverted 5 nm-wide QW on a macroscopic Hall bar (a) and a multiple-wire sample (b) for five different gate voltages. Similar to the 7 nm QW data (Fig. 5.3) a resistance dip is observable around $B = 0$. The peak height is approximately constant in the presented gate-voltage range Fig. 5.4 b). In order to compare the WAL effect on the normal (5 nm) and inverted (7 nm) QW, we have measured the WAL signal in both samples for similar carrier densities. The WAL signal, $\delta\sigma_{xx}$, is extracted from the magnetoconductance by subtracting the smooth parabolic background and taking the device geometry into account:

$$\delta\sigma_{xx} = \delta G_{xx}\frac{l}{w}\frac{1}{N}, \tag{5.3}$$

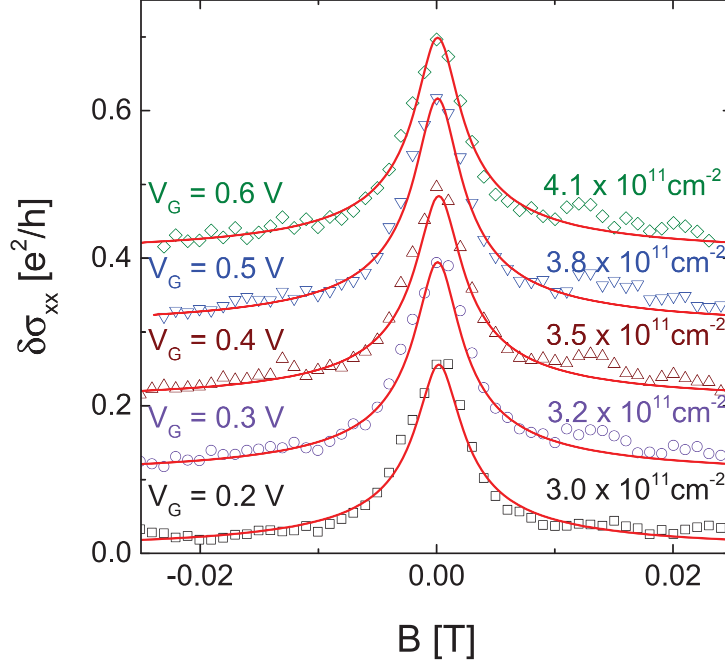

Figure 5.6.: *WAL contribution to the magnetoconductivity, $\delta\sigma_{xx}(B)$, for wires of* 5 nm *(normal) QW at different gate voltages V_g. The thin (red) lines are fits based on Eqs. (5.4) - (5.6). Subsequent curves are shifted by $0.1e^2/h$ for clarity.*

with l, w and N the wire length, width and number of wires, respectively. The results are shown in Fig. 5.5 for the inverted and in Fig 5.6 for the normal QW. The magnitude of the WAL peak is found between 1.8 and 2 e^2/h for the inverted QW and, remarkably, one order of magnitude smaller for the normal QW. For a better comparison we enlarged the conductivity scale for the normal QW (Fig 5.6). In both cases, the WAL features display a very similar line shape. For further analysis we require the relevant phase coherence length for the samples under investigation. A convenient way to obtain this quantity is to measure the temperature dependence of the WAL peak. The results are plotted in Fig. 5.7 for five different temperatures, up to 16 K, and three different gate voltages.

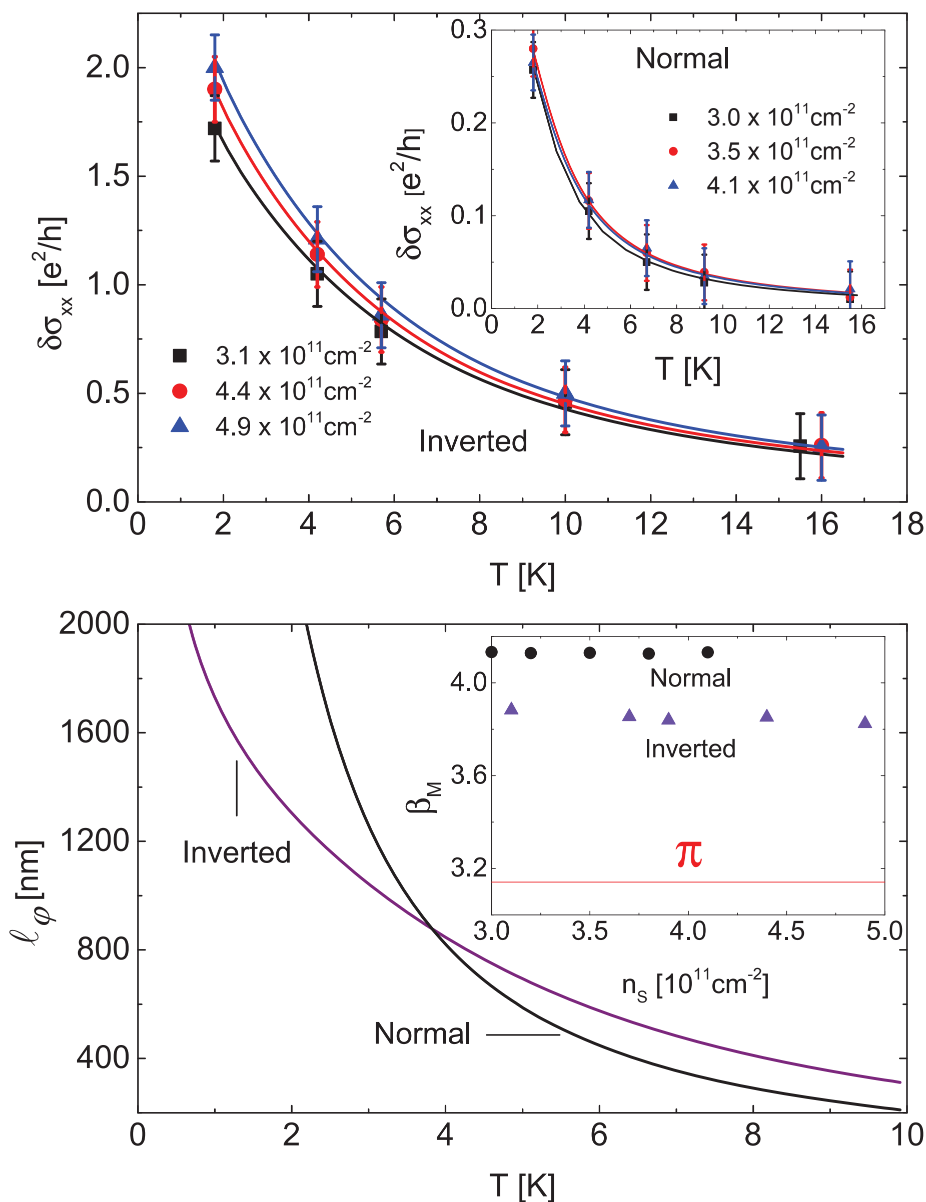

Figure 5.7.: *(a) Temperature dependence of the conductivity $\delta\sigma_{xx}(T)$ for wires of the 7 nm (inverted) QW and 5 nm (normal) QW (inset) at different gate voltages. The solid lines are fits based on Eqs. (5.4) - (5.6). (b) Extracted dephasing length for wires of the inverted and normal QW at $V_g = 0$. Inset: Extracted Berry phase, β_M, versus carrier density n_s for inverted and normal samples.*

5.3. Model

Since the magnitude of the WAL presented here is several times larger than in the corresponding 2D systems [182, 183], we attribute the observed pronounced WAL to the quasi-1D diffusive character of the transport, i.e. the width of the sample, w, is significantly smaller than the phase coherence length, ℓ_φ. We verify this conjecture by comparing the measurements with theoretical results for the quantum-interference correction to the classical (Drude) conductivity, $\delta\sigma_{xx}$, which is different for different dimensions. We derive $\delta\sigma_{xx}$ for the quasi-1D diffusive wires using the four-band Bernevig-Hughes-Zhang (BHZ) model for HgTe QWs [13] and the approach of Ref. [184], as outlined in Ref. [154]. The parameters $\mathcal{M}$, $\mathcal{A}$, $\mathcal{B}$, and $\mathcal{D}$ of the BHZ model are inferred from fitting the band structure, while the carrier densities are deduced from appropriate Hall measurements (see Tab. 5.1, Tab. 5.2 and Tab. 5.3). The conductivity

Table 5.2.: *Gate-voltage V_g dependent carrier density n , Fermi energy E_F and fitting parameters c_1 and c_2 for the 7 nm (inverted) QW. The experimentally encountered mobilities varies between* 30000 and 60000 $\mathrm{cm}^2/\mathrm{Vs}$ *for the normal and inverted samples.*

V_g [V]	n [$\times 10^{11}$]	c_1 [$\times 10^7$ nm^{-2}K$^{-2/3}$]	c_2 [$\times 10^7$ nm^{-2}K^{-3}]	E_F [meV]
0.75	4.9	3.25	0.09	58.5
0.55	4.4	3.25	0.08	48
0.35	3.9	3.25	0.08	39
0.25	3.7	3.25	0.08	34
0	3.1	3.25	0.07	22.2

Table 5.3.: *Gate-voltage V_g dependent carrier density n , Fermi energy E_F and fitting parameters c_1 and c_2 for the 5 nm (normal) QW.*

V_g [V]	n [$\times 10^{11}$]	c_1 [$\times 10^7$ nm^{-2}K$^{-2/3}$]	c_2 [$\times 10^7$ nm^{-2}K^{-3}]	E_F [meV]
0.6	4.1	0.05	0.23	131.0
0.5	3.8	0.05	0.23	128.0
0.4	3.5	0.05	0.23	123.9
0.3	3.2	0.05	0.23	120.4
0.2	3.0	0.05	0.23	116.2

correction is then given by

$$\delta\sigma_{xx} = \frac{2\frac{e^2}{h}\,(1 + C_M)}{w\sqrt{\ell_\varphi^{-2} + \ell_B^{-2} + \ell_M^{-2}}}, \tag{5.4}$$

where the factor of 2 accounts for independent contributions of the Kramers-partner blocks in the BHZ Hamiltonian, ℓ_φ, ℓ_B and ℓ_M are the characteristic length-scales for transport in the diffusive quantum interference regime:

$$\ell_\varphi = (c_1 T^{2/3} + c_2 T^3)^{-1/2}, \;\; \ell_B = \sqrt{3}\hbar/(w|eB|), \tag{5.5}$$

$$\ell_M = \frac{\ell}{\sqrt{2}|1 - \beta_M/\pi|}, \;\; C_M \approx -\frac{19}{2}\left(1 - \frac{\beta_M}{\pi}\right)^2, \tag{5.6}$$

$$\beta_M = \pi\left(1 + \frac{\mathcal{M} + \mathcal{B}k_{_F}^2}{E_\mathrm{F} - \mathcal{D}k_{_F}^2}\right). \tag{5.7}$$

In Eq. (5.5), ℓ_φ represents the dephasing length due to electron-electron and electron-phonon interactions with respective contribution $\propto T^{2/3}$ and $\propto T^3$ for quasi-1D diffusive wires (see, e.g., Ref. [185]), and proportionality constants c_1 and c_2. The length ℓ_B is the characteristic length scale for time-reversal symmetry breaking in a magnetic field [186], whereas ℓ_M and C_M in Eq. (5.6) are associated with the band Berry phase β_M controlling the rate of 180°-backscattering. β_M deviates from the universal value of π, which characterizes gapless Dirac-cones [172], because of the finite band gap $\mathcal{M}$ and the quadratic correction to the dispersion $\mathcal{B}k_{_F}^2 > 0$. E_F and $k_{_F} = \sqrt{2\pi n}$ are the Fermi energy and momentum, and $\mathcal{D}k_{_F}^2 > 0$ is the parabolic part of the QW energy spectrum [154]. ℓ in Eq. (5.6) is determined by the carrier mobility and density as

$$\ell = (h/e)\mu\sqrt{n/(2\pi)}. \tag{5.8}$$

It should be noted that Eqs. (5.4) and (5.6) are valid for weak deviations of

$$(1 - \beta_M/\pi)^2 = (\mathcal{M} + \mathcal{B}k_{_F}^2)^2/(E_\mathrm{F} - \mathcal{D}k_{_F}^2)^2 \ll 1. \tag{5.9}$$

We use Eq. (5.4) to fit the measured magnetic-field and temperature dependence of the WAL for both the normal and the inverted QW. c_1 and c_2 are determined by simultaneously fitting the magnetoconductivity data of Figs. 5.5 and 5.6 and the temperature dependence of the WAL peaks presented in Fig. 5.7 a) (see also Tab. 5.2). The fits are

plotted with the experimental data in Figs. 5.5 and 5.6.

5.4. Discussion

From the quality of the fits it is evident that the quasi-1D diffusive transport model represents the experimental data remarkably well. Additionally, the temperature-dependent dephasing length $\ell_\varphi(T)$ can be extracted, which is shown in Fig. 5.7 b) for both inverted and normal QWs. At the lowest experimental temperature, $T = 1.8$ K, ℓ_φ is well over 1200 nm for both samples, which significantly exceeds the width, $w = 370$ nm, of the wires and adds to the justification of the conjecture that the observed WAL effect is quasi-1D. Comparable dephasing lengths were reported for narrow $Ga_xIn_{1-x}As/InP$ wires [187]. We now turn to the observed difference in the WAL amplitude between the inverted and normal QWs (cf. Figs. 5.5 and 5.6). The large value of $\ell_\varphi(T)$ for the normal QW rules out that strong dephasing can explain the less pronounced WAL. Moreover, magnetotransport experiments on single wires displayed in Figs. 5.8 and 5.9 show examples of universal conductance fluctuations that are equally pronounced in both types of samples, which is another clear evidence for similar phase-coherent transport properties. In quasi ballistic wires, the WAL amplitude can also be affected by multiple boundary scattering due to partial magnetic flux cancellation [193]. This occurs when the 1D mean-free path, ℓ_{1D}, is larger than width w. From the zero field conductivities of the wires and Hall bars we estimate ℓ_{1D} to be about 100 nm and 50 nm for the inverted and normal QW structure, respectively, over the entire gate-voltage range. Since for both samples ℓ_{1D} is smaller than the width w of the wires, boundary scattering can hardly account for the experimental observation either[1]. Hence, we conclude that the weaker WAL in wires with a normal band order is related to the specifics of the band structure that are encoded in the Berry phase, β_M. The inset in Fig. 5.7 b) shows the Berry phase β_M extracted from fitting the experimental data for the inverted and normal QW to Eqs. 5.4, 5.5 and 5.6. For both QWs, β_M deviates from π because of the non-zero total gap $\mathcal{M} + \mathcal{B}k_F^2$ in both wells. Interestingly, the deviation from π is stronger for the normal QW. For a normal band structure, such a non-zero, positive deviation is expected because the

[1] The well-known Dirac-fermion confinement model of M.V. Berry and R.J. Mondragon, Proc. R. Soc. Lond. A **412**, 53 (1987), is not valid for n-type HgTe nanowires (with the Fermi level positioned deep in the conduction band) because of non-negligible quadratic corrections to the linear Dirac dispersion.

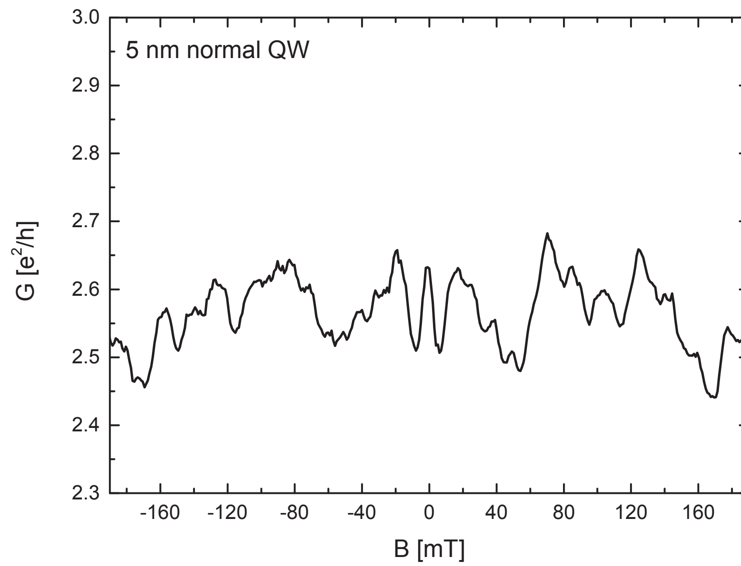

Figure 5.8.: *Conductance as a function of magnetic field showing universal conductance fluctuations, measured at* $T = 1.8\,\mathrm{K}$ *on a single wire structured from material with a normal QW.*

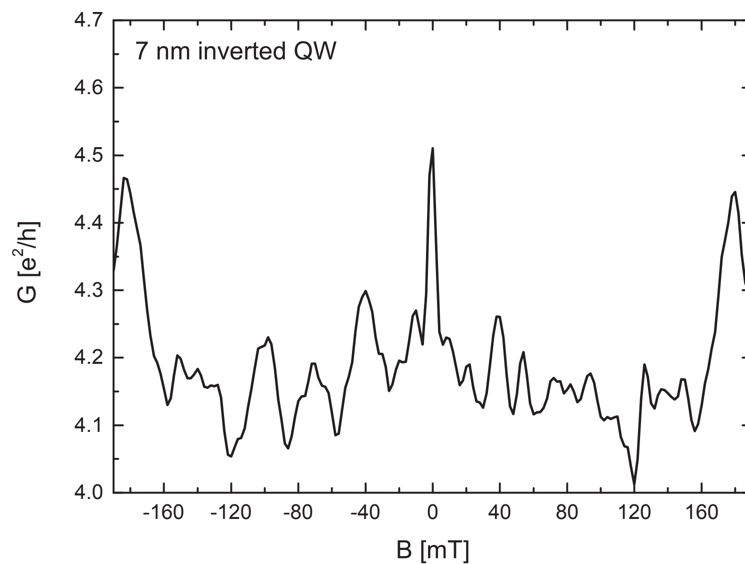

Figure 5.9.: *Conductance as a function of magnetic field showing universal conductance fluctuations, measured at* $T = 1.8\,\mathrm{K}$ *on a single wire structured from material with an inverted QW.*

terms $\mathcal{M}$ and $\mathcal{B}k_F^2$ in Eq. (4) are both positive and thus can never cancel each other, whereas a partial or complete cancellation of both terms occurs for the inverted QW because of the negative gap parameter, $\mathcal{M} < 0$. Consequently, normal QWs may show enhanced backscattering and a tendency to WL, which is accounted for by the negative subleading correction C_M in Eq. 5.4, reducing the WAL effect. Formally, the subleading correction C_M in Eqs. 5.4 and 5.6 reflects the axial spin-rotation symmetry of the BHZ model. Depending on the parameters of the BHZ model, the Berry phase β_M now has a value between π and 2π, which results in a reduced WAL compared with the simplectic case where $\beta_M = \pi$ and $\delta\sigma_{xx} = (2e^2/h)(\ell_\varphi/w)$. In agreement with our analytical results, a weaker WAL for the normal band gap QW structures has been also found in numerical studies for HgTe QWs within the BHZ model [188]. It is worth noting that the spin-rotation symmetry of the BHZ model can be broken by the SOI arising from bulk or/and structural inversion asymmetry [189]. Strong SOI-induced spin mixing may in general obscure a manifestation of Berry phase effects related to the Dirac band structure [188, 190]. However, in the present experiments, the Rashba SOI is adjusted to zero or, at least, to be very weak. As to the bulk-inversion asymmetry, it is most probably also negligible because the magnetoresistance data do not reveal any corresponding signatures. This implies that calculations based on the BHZ model should give a valid description of our data, as is also evidenced by the quality of the fits in Figs. 5.5 and 5.6. In conclusion, the observed WAL effect reveals a direct link between quantum transport in quasi-1D HgTe QW structures and the Berry phase of their single-valley energy bands. In this respect, the HgTe nanowires are distinct both from graphene nanoribbons, where the edge roughness generates intervalley scattering, and from low-dimensional semiconductors with SOI-split parabolic bands, e.g., InAs nanowires [191] and $\mathrm{Ga}_x\mathrm{In}_{1-x}\mathrm{As/InP}$ nanowires [187]. It is well-known that the conventional low-dimensional semiconductors show a crossover to the WL with an increasing SOI-induced spin-relaxation length ℓ_{SO} [192]. The absence of such a crossover in our measurements points to the dominant role of the band Berry phases yielding robust WAL regardless of the presence or absence of the structural- or bulk-inversion SOI effects.

6. Summary

Topological insulators belong to a new quantum state of matter that is currently one of the most recognized research fields in condensed matter physics. Strained bulk HgTe and HgTe/HgCdTe quantum well structures are currently one of few topological insulator material systems suitable to be studied in transport experiments. In addition HgTe quantum wells provide excellent requirements for the conduction of spintronic experiments. A fundamental requirement for most experiments, however, is to reliably pattern these heterostructures into advanced nano-devices. Nano-lithography on this material system proves to be challenging because of inherent temperature limitations, its high reactivity with various metals and due to its properties as a topological insulator. The current work gives an insight into why many established semiconductor lithography processes cannot be easily transferred to HgTe while providing alternative solutions. The presented developments include novel ohmic contacts, the prevention of metal sidewalls and redeposition fences in combination with low temperature (80 °C) lithography and an adapted hardmask lithography process utilizing a sacrificial layer. In addition we demonstrate high resolution low energy (2.5 kV) electron beam lithography and present an alternative airbridge gating technique. The feasibility of nano-structures on HgTe quantum wells is exemplarily verified in two separate transport experiments. We are first to realize physically etched quantum point contacts in HgTe/HgCdTe high mobility 2DEGs and to prove their controllability via external top-gate electrodes. So far quantum point contacts have not been reported in TI materials. However, these constrictions are part of many proposals to probe the nature of the helical quantum spin Hall edge channels and are suggested as injector and detector devices for spin polarized currents. To confirm their functionality we performed four-terminal measurements of the point contact conductance as a function of external gate voltage. Our measurements clearly exhibit quantized conductance steps in $2e^2/h$, which is a fundamental characteristic of quantum point contacts. Furthermore we conducted measurements on the formation and control of collimated electron

beams, a key feature to realize an all electrical spin-optic device. In a second study several of the newly developed lithography techniques were implemented to produce arrays of nano-wires on inverted and non-inverted HgTe quantum well samples. These devices were used in order to probe and compare the weak antilocalization (WAL) in these structures as a function of magnetic field and temperature. Our measurements reveal that the WAL is almost an order of magnitude larger in inverted samples. This observation is attributed to the Dirac-like dispersion of the energy bands in HgTe quantum wells. The described lithography has already been successfully implemented and adapted in several published studies. All processes have been optimized to guarantee a minimum effect on the heterostructure's properties and the sample surface, which is especially important for probing the topological surface states of strained HgTe bulk layers. Our developments therefore serve as a base for continuous progress to further establish HgTe as a topological insulator and give access to new experiments.

7. Zusammenfassung

Topologische Isolatoren (TIs) beschreiben einen neuartigen Quanten-Aggregatszustand, der derzeit eines der meist beachteten Forschungsfelder in der Festkörperphysik darstellt. Verspannt gewachsene HgTe Schichten, sowie HgTe/HgCdTe Quantentrogstrukturen sind als eines der wenigen TI-Materialsysteme geeignet, um in Transportexperimenten untersucht zu werden. Darüber hinaus bieten HgTe Quantentröge hervorragende Voraussetzungen zur Durchführung von Spintronik-Experimenten. Eine grundlegende Voraussetzung für die meisten Versuche ist die zuverlässige Herstellung komplexer Nanostrukturen in diesen Schichtsystemen. Aufgrund der intrinsischen Temperaturgrenzen, der hohen Reaktivität mit verschiedensten Metallen und nicht zuletzt seiner Eigenschaften als topologischer Isolator, stellt Nanolithographie auf HgTe eine Herausforderung dar. Die vorliegende Arbeit zeigt auf, weshalb viele der in der Halbleitertechnik etablierten Lithographieprozesse nicht einfach auf HgTe übertragbar sind und bietet stattdessen alternative Lösungen. Die vorgestellten Entwicklungen befassen sich unter anderem mit der Herstellung ohmscher Kontakte, der Vermeidung metallischer Seitenwände und Ätzresiduen in Kombination mit Niedertemperatur-Lithographie ($\leq$80 °C) und einem angepassten Hartmasken-Lithographieprozess. Zusätzlich demonstrieren wir hochauflösende Niederenergie-Elektronenstrahllithographie (2.5 kV) und die Strukturierung freitragender Gate-Elektroden. Die Realisierbarkeit von Nanostrukturen in HgTe Quantentrögen wurde anhand zweier unabhängiger Transportexperimente verifiziert. Wir präsentieren die erste Umsetzung physikalisch geätzter Quantenpunktkontakte in hochbeweglichen HgTe/HgCdTe 2DEGs und weisen deren Kontrollierbarkeit mittels externer Topgate-Elektroden nach. Bisher wurden experimentell noch keine Quantenpunktkontakte in TI-Materialien realisiert. Um deren Funktionalität zu bestätigen, wurden Messungen des Punktkontaktleitwerts als Funktion der externen Gate-Spannung durchgeführt. Die Messungen zeigen deutlich quantisierte Leitwertstufen in Abständen von $2e^2/h$, ein Charakteristikum von QPCs. Darüber hinaus wurden Untersuchungen zur Erzeugung und Kontrolle kollimierter Elektro-

nenstrahlen durchgeführt, einer Schlüsselvoraussetzung zur Umsetzung spinoptischer Bauteile. Für die zweite Studie wurden mehrere der beschriebenen Lithographie-Techniken angewandt, um präzise Anordnungen aus Nanodrähten aus invertierten sowie nicht invertierten Quantentrögen zu erstellen. Mit diesen Proben wurde der Effekt der schwachen Antilokalisierung in Abhängigkeit von Magnetfeld und Temperatur untersucht. Unsere Messungen zeigen, dass die schwache Antilokalisierung in invertierten Proben um fast eine Größenordnung höher ist. Diese Beobachtung kann wiederum der Dirac-artigen Dispersion der Energiebänder in HgTe Quantentrögen zugeschrieben werden. Alle Lithographieprozesse wurden optimiert, um Einflüsse auf die Materialeigenschaften sowie die Probenoberfläche zu minimieren. Dies ist besonders für die Untersuchung der topologischen Oberflächenzustände verspannt gewachsener HgTe-Schichten relevant. Die vorgestellten Entwicklungen dienen dabei als Grundlage, um HgTe weiter als topologischen Isolator zu etablieren und gewähren Zugang zu neuen Experimenten. Die in dieser Arbeit beschriebene Lithographie fand bereits mehrfach Anwendung in verschiedenen veröffentlichten Studien.

A. List of substrates

Table A.1.: *List of substrates with their detailed layer sequence and thicknesses d from top (left) to bottom (right). Doping is indicated with y (yes) or n (no).*

Wafer	cap	doping	spacer	QW	spacer	doping	buffer	n (4 K)	μ (4 K)
	d	d	d	d	d	d	d	$\cdot 10^{11}$	$\cdot 10^{3}$
	nm	y/n, nm	nm	nm	nm	y/n, nm	nm	cm^{-2}	cm^2/Vs
Q2151	25	y, 9	10	12	10	n, 9	25	46.6	10
Q2190	25	y, 9	20	8	20	n, 9	100	13.6	338
Q2226	25	y, 9	10	8	10	y, 9	100	8.8	363
Q2317	25	y, 9	40	9	-	-	100	9.2	32
Q2320	25	y, 9	40	8.5	-	-	100	4.6	59
Q2334	15	-	-	8	40	y, 9	100	5.7	230
Q2382	25	y, 9	50	12	50	y, 9	100	3.1	229
Q2386	15	-	-	6.5	100	y, 9	100	2.9	279
Q2388	25	y, 9	80	7	80	y, 9	100	2.1	25
Q2389	25	-	-	7	70	y, 9	100	3.1	127
Q2391	25	-	-	7	70	y, 9	100	3.4	151

B. Acronyms

2DEG	two-dimensional electron gas
AC	alternating current
AFM	atomic force microscope
ALD	atomic layer deposition
BHZ	Bernevig Hughes Zhang
CAR	chemically amplified resist
CBO	conduction band offset
CD	critical dimension
CVD	chemical vapor deposition
DC	direct current
DI	de-ionized
DMSO	dimethyl sulfoxide
DUT	device under test
EB-PVD	electron beam physical vapor deposition
FIB	focused ion beam
IBE	ion beam etching
IPA	iso-propyl alcohol
IC	integrated circuit
MBE	molecular beam epitaxy
MEMS	micro-electromechanical systems
MIBK	methyl isobutyl ketone
MIM	microwave impedance microscopy
MOS-FET	metal oxide semiconductor field effect transistor
NEP	N-ethyl pyrolidone
NMP	N-methyl pyrolidone
NLR	non-local resistance
PAB	post apply bake

PEB	post exposure bake
PE-CVD	plasma enhanced chemical vapor deposition
PES	photo electron spectroscopy
PMMA	poly(methyl methacrylate)
QH	quantum Hall
QHE	quantum Hall effect
QSH	quantum spin Hall
QSHE	quantum spin Hall effect
QPC	quantum point contact
QW	quantum well
RIE	reactive ion etching
SEM	scanning electron microscope
SHE	spin Hall effect
SdH	Shubnikov de Haas
SO	spin orbit
SOI	spin orbit interaction
spinFET	spin field effect transistor
SQUID	superconducting quantum interference device
TKNN	Thouless, Kohmoto, Nightingale and den Nijs
TMA	trimethylaluminum
TMAH	tetra methyl ammonium hydroxide
TI	topological insulator
UHV	ultra high vacuum
VBO	valence band offset
WAL	weak antilocalization
WL	weak localization
XPS	x-ray photoelectron spectroscopy

C. Publications

- E. Y. Ma, M. R. Calvo, J. Wang, B. Lian, **M. Mühlbauer**, C. Brüne, Y-T. Cui, K. Lai, W. Kundhikanjana, Y. Yang, M. Baenninger, M. König, C. Ames, H. Buhmann, P. Leubner, L. W. Molenkamp, S-C. Zhang, D. Goldhaber-Gordon, M. A. Kelly and Z-X. Shen, "Unexpected edge conduction in mercury telluride quantum wells under broken time-reversal symmetry", *Nature Communications* **6**, 7252, (2015).

- **M. Mühlbauer**, A. Budewitz, B. Büttner, G. Tkachov, E. M. Hankiewicz, C. Brüne, H. Buhmann, and L. W. Molenkamp, "One-dimensional weak anti-localization due to band Berry phase in HgTe wires", *Physical Review Letters* **112**, 146803, (2014).

- S. Hart, H. Ren, T. Wagner, P. Leubner, **M. Mühlbauer**, C. Brüne, H. Buhmann, L. W. Molenkamp and A. Yacoby, "Induced superconductivity in the quantum spin Hall edge", *Nature Physics* **10**, 638–643 (2014).

- A. Shuvaev, A Pimenov, G. V. Astakhov, **M. Mühlbauer**, C. Brüne, H. Buhmann, L. W. Molenkamp, "Room temperature electrically tunable broadband terahertz Faraday effect", *Applied Physics Letters* **102**, 241902 (2013).

- M. Baenninger, M. König, A. G. F. Garcia, **M. Mühlbauer**, C. Ames, P. Leubner, C. Brüne, H. Buhmann, L. W. Molenkamp, and D. Goldhaber-Gordon, "Fabrication of samples for scanning probe experiments on quantum spin Hall effect in HgTe quantum wells", *Journal of Applied Physics* **112**, 103713 (2012).

List of Figures

2.1. Examples for electronic band structures for a trivial insulator a) with an even number of band crossings with the Fermi energy E_F and a topological insulator b) with an odd number of crossings. Picture adapted from Ref. [9]. 4

2.2. Illustration of the relativistic corrections of the Hamiltonian for CdTe (a) and HgTe (b). Adapted from Ref. [24]. 6

2.3. Bandstructures around $k = 0$ for HgTe and $Hg_{0.32}Cd_{0.68}Te$ calculated using the $\mathbf{k} \cdot \mathbf{p}$ method. Equal bands are coded in the same color. VBO indicates the valence band offset, CBO the conduction band offset. Adapted from Ref. [22]. 7

2.4. Illustration for the subband ordering in type-III $HgTe/Hg_{0.32}Cd_{0.68}Te$ heterostructures for a QW below and above the critical thickness d_c. Wider wells result in a descent of electron-subbands E1/E2 and a simultaneous rise of the hole-subbands H1/H2. For better visualization the Γ_8 well is displayed slightly wider than the Γ_6. 7

2.5. a) Subband dispersion for a 4 nm QW. b) Subband ordering of electron (E1/E2) and light hole/heavy hole bands (L1/H1-H6) as a function of QW thickness. The critical thickness d_c at 6.3 nm separates the non-inverted (red) from the inverted region (blue). c) Subband dispersion for a 15 nm QW. Adapted from Ref. [22]. 8

2.6. Longitudinal resistance of Hall bar structures as a function of gate voltage for non-inverted (I) and inverted QWs (II-IV). The inset shows a sketch of the six-terminal sample geometry [14]. 10

2.7. Sketch for the lowest states in valence- (blue) and conduction band (red) for a normal a) and an inverted bandstructure b) for a sample with width w. Because of the boundary conditions this leads to a crossing at the sample edge only for inverted structures (inset), forming the QSH channels [123] 11
2.8. Two- and four-terminal measurements on a six-terminal device as a function of gate voltage for various contact configurations. Dotted lines indicate the expected values as calculated from the Landauer-Büttiker formalism [31]. 12
2.9. Illustration of the difference between QH and QSH edge channel transport for two and three terminals. In both cases μ_{left} is the higher chemical potential and drives the current to the right. The line thickness corresponds to the occupancy of the states. In the QH conductor the current flows on one side (B), while in the TI the transport is equal on both sides (A). Adding an extra terminal μ_{probe} in the QH state changes nothing (D), in the TI however (C), conductance is cut by half a conductance quantum, because of the current flowing back. Adapted from Ref. [33]. 13
2.10. Schematic of two complementary measurements for probing the spin polarization of the QSH edge states. **a)** Current is injected into the metallic branch (green). Because of the intrinsic SHE, different spins accumulate at opposite sample edges. At the interconnection, the spins are only allowed to populate the matching channel, leading to a detectable voltage at contacts 1 and 2. **b)** Current is injected into the QSH branch. Different spins propagate at opposite sample edges, thus injecting a spin current into the metallic region. This again leads to a detectable voltage because of the inverse SHE [35]. 14
2.11. **a)** Illustration of the measurement. The current (blue) induces a magnetic field (red) that can be picked up with the SQUID. **b)** Transport configuration of the Hall bar. **c)** Two-terminal resistance versus gate voltage. **d, e)** Flux images at gate voltages as indicated in c). In d) white dashed lines indicate the Hall bar mesa, the black stripe indicates a scale of 20 µm. **f, g)** X-component, **h, i)** y-component of the current density, obtained from the current inversion of the flux images from d) and e). From Ref. [36]. 15

3.1. Illustration of the saddle potential with cross sections in x and y direction. Grey shaded areas indicate potential barriers for electrons. 19

3.2. Calculation of the single channel transmission probability T_{nn} and the total conductance $T = \sum_{nn} T_{nn}$ as a function of $(E - V_0)/\hbar\omega_x$ for a ratio of $\omega_y/\omega_x = 3$, adapted from Ref. [66]. 20

3.3. Conductance of an adiabatic constriction as a function of $(E - V_0)/\hbar\omega_x$ for different ratios of ω_y/ω_x. From Ref. [66]. 21

3.4. Calculation of conductance g for different aspect ratios a = L/W for abrupt transitions. Adapted from Ref. [75]. 22

3.5. Illustration of the collimation effect for an abrupt potential barrier of height E_c **a)** and a horn shaped structure **b)**. Different electron trajectories are outlined. For both cases electrons approaching at an angle α (red dashed lines) are reflected. Shaded areas indicate the potential barrier, W_{min} and W_{max} denote the minimal and maximal constriction width. Adapted from Ref. [78]. 23

3.6. **a)** Plot of the collector voltage V_c divided by the injector current I_i versus magnetic field. The solid line shows the experimental data, dots show simulation results, dashed lines show the expected signal without collimation **b)** Calculation of the adiabatic angular distribution at $B =$ 0 T for a collimation factor $f = 1.85$ (dotted line) and without collimation $f = 1$ (dashed line). The solid line shows a simulation for a conical potential. Adapted from Ref. [81]. 26

3.7. Colored SEM micrograph of a typical GaAs/AlGaAs split gate QPC structure. White dashed lines schematically indicate the potential formed around the yellow gate electrodes. Blue areas indicate the 2DEG area, grey areas depict depleted regions. Electrons cannot pass this barrier except for tunneling and will therefore be reflected (dashed black line). QSH edge channels (marked in red an blue) however, are bound to the physical sample edge and are not influenced by the gate as they continue to exist in the band gap. 28

3.8. Direct and indirect band gap for undoped CdTe and CdZnTe (001) substrates as a function of quantum well width d_{HgTe}. 29

3.9. Colored SEM micrograph of a typical etched HgTe/HgCdTe QPC with a width of 200 nm and a length of 80 nm. For better illustration the 2DEG area is marked in blue and the topgate electrode is colored in yellow. Both are separated by a 30 nm insulating SiO_2/Si_3N_4 lattice grown in a PE-CVD process. The grainy structure on the surface has its origin in the low growth temperature of the insulator at 80°C. The typical four-terminal measurement configuration is illustrated schematically. Current is passed from terminal 2 to 3 while the voltage drop over the constriction is monitored between terminal 1 and 4. 30

3.10. **QPC-01:** AC four-terminal resistance measurements of an etched QPC, varying the applied topgate voltage form 0 V to −0.5 V (red triangles) and back (black squares). The measurement was performed at 4.2 K. Dashed lines indicate the expected theoretical quantization values. Solid lines indicate the quantization values shifted by an offset of 1.3 kΩ to demonstrate the good agreement with steps appearing in the measurement, especially for higher mode occupation numbers N. The lower graph shows the conductance plot including the offset of 1.3 kΩ. Note that the resistance value approaches $2e^2/h$ for −0.5 V, which is an indication of the remaining QSH edge channels. 32

3.11. **QPC-02:** Four-terminal DC resistance measurement of an etched QPC, as a function of topgate voltage from −1.4 V to −2.5 V. The measurement was conducted at 4.2 K. Dashed lines indicate the theoretical quantization values. Solid lines indicate quantization values shifted by an offset of 500 Ω to demonstrate the good agreement with steps appearing in the measurement. The lower graph shows the same measurements as conductance plot including the offset. Note the decrease in conductance in steps of $2\mathrm{e}^2/\mathrm{h}$ as expected from theory. 33

3.12. Hall resistance R_{xy} (red) and longitudinal resistance R_{xx} (black) of a macroscopic Hall bar at T = 4 K as a function of magnetic field B. . . 36

3.13. **a)** Non-local resistance (NLR) signal for structures with lead widths of 1.0 µm (structure A) and 0.45 µm (structure B), adapted from Ref. [87]. **b)** For comparison the NLR of two identical dry etched 290 nm wide ungated QPCs, separated by a distance of 930 nm. 37

3.14. Non-local resistance measurement (collimation signal) of two 290 nm wide QPCs in a distance of 930 nm for different topgate voltages of QPC A and B as a function of applied external magnetic field B. 39
3.15. **Upper graph:** Simultaneous measurement of the four-terminal injector QPC resistance (red squares) and the non-local collimation resistance at $B = 0$ T (black triangles) as a function of injector gate voltage. **Lower graph:** The collimation factor f as a function of injector QPC resistance. A linear dependence is expected from the adiabatic theory. . . . 41
3.16. The angular distribution as a result of the adiabatic approximation for collimation factors $f = 1.12$ (black), $f = 1.30$ (red) and $f = 1.65$ (blue). The dashed line in the left graph indicates the distribution without collimation. The angular distribution of the transmitted electrons is schematically illustrated in a SEM micrograph of an actual structure on the right. 42
3.17. Schematic of an optical polarizer a) and a spin polarizer b) as proposed by Khodas *et al.* [89]. In classical optics the splitting of different polarization directions (in plane, red and out of plane, blue) happens at the interface of a birefringent material. Analogue the separation of electrons of different polarization (spin up, blue and spin down, red) happens at the interface between two regions of variable spin orbit interaction strength. 45
3.18. a) Schematic illustration of the dispersion relation with (red and blue) and without (black) Rashba spin orbit coupling. b) Topview of the dispersion relation in the k_x and k_z plane at the Fermi surface. The momentum of the incoming beam from a region without spin orbit coupling "N" (black) parallel to the scattering interface is conserved while the perpendicular momentum changes depending on the chirality of the electrons (red and blue) in a region with spin orbit interaction "SO". . 46
3.19. The angle of refraction for the two polarization modes as a function of the angle of incidence. φ^c is the angle for total internal reflection for (+)-mode. θ^c determines the aperture for (-)-mode. θ^s defines the angle of separation between modes of different chirality. Other angles are related to the spin filtration and are explained in the text. With $\alpha = 0.1$ and B(x) = const. From Ref. [89]. 47

3.20. Hall resistance R_{xy} (red) and longitudinal (SdH) resistance R_{xx} (black) of a macroscopic Hall bar at T = 4 K as a function of magnetic field B. 48
3.21. Shubnikov de Haas (SdH) oscillations at T = 4 K as a function of magnetic field B at increasing positive gate voltages. Note that the observable beating at U = 0 V gradually diminishes with increased gate voltage. For clarity the traces are displayed with a constant offset of 300 Ω. 49
3.22. Colored SEM micrograph. The 2DEG is marked in blue, gates are marked in yellow. Two QPCs are separated by a thin gate stripe. The ungated areas exhibit spin orbit coupling (SO) while in the gated area the spin orbit coupling can be adjusted to larger, or smaller values (N). 50
3.23. Non-local resistance measured as a function of magnetic field B and different positive splitter voltages. Electrons are injected via one point contact to interfere with the splitter gate. Increasing the voltage up to 3 V continuously increases the detected signal at the second QPC. Measurement curves are displayed with a constant offset of 25 Ω for better visualization. 51
3.24. Non-local resistance measured as a function of magnetic field and different negative splitter gate voltage. Electrons are injected via one point contact to interfere with the splitter gate. Decreasing the splitter voltage down to −1.4 V continuously reduces the detected signal at the second QPC. The observed drop suggests a downgrade in electron transmission because of increased scattering. Measurement curves are displayed with a constant offset of −25 Ω for better visualization. 52
3.25. Calculation of the carrier density plotted against the applied gate voltage for a reference Hall bar. To obtain this graph the Hall resistance was measured at a constant magnetic field of $B = 1$ T in a gate voltage range between −1.5 V and +2 V. 53
3.26. Calculation of refracted angles θ_2 as a function of electron density in the splitter gate region, based on a 2DEG density of $n_1 = 5.7 \cdot 10^{11}$ cm^{-2} and an incident angle θ_1 of 45°. 55
3.27. Schematic multi-QPC setup for two angles of incidence θ_1, 60 ° (a) and 90 ° (b). Depending on the applied splitter voltage, the detected signal will either be received in terminal B or terminal C. 56

4.1. Optical microscope picture of a macro Hall bar structure with topgate as used by Ref. [14] prior to thermal bonding. Arrows indicate the device dimensions. 60
4.2. Composite photograph at 500x showing growth of an intermetallic compound at 100°C (blue). Clockwise: 72 hours, 1 to 5 o clock; 144 hours, 5 to 9 o clock; and 240 hours, 9 to 1 o clock. Adapted from Ref. [103] and colored for better visualization. 62
4.3. Optical microscope picture of a typical indium bonded chip with optical mesa and gate leads including bondpads and Au wires. The different shapes and sizes of the indium contacts (black) are visible. Bubbles appearing around the contacts are due to outgasing beneath the insulator during the In soldering. 63
4.4. Schematic picture of a typical HgTe/HgCdTe heterostructure with the correct aspect ratio of all MBE layers a) and a detailed description b). 64
4.5. **a)** Schematic picture of a section of the test structure. Green parts indicate the dry etched mesa area, orange parts symbolize the evaporated metal and dashed lines show the actual overlap between mesa and metal, the contact area A. Different contact sizes A1 and A2 can be achieved by repeated exposure using the hexagonal aperture. Note that the contact width W is defined through the etched mesa and kept constant at 150 μm. The contact resistance is measured in a three terminal configuration. Current is passed from contact 1 to contact 2, while the voltage drop is measured between 1 and 3. **b)** Schematic cross section of metal and mesa. The position of the QW is indicated in red. **c)** Optical microscope picture of an actual test sample. The dashed white line indicates the mesa perimeter. 65
4.6. Three terminal resistance measurement of evaporated In contacts at $T = 2$ K, plotted against the contact area. The error bars are estimated from the technological uncertainty in identifying the actual contact area. Dry etched contacts with a thinner cap layer are marked as red diamonds. 67
4.7. Three terminal resistance measurements of evaporated In contacts at T = 2 K, plotted against the contact area. 68
4.8. Three terminal resistance measurements of evaporated In contacts at T = 2 K, plotted against the cap layer thickness d_{cap}. 70

4.9. Three terminal resistance measurements of evaporated In contacts at T = 2 K, plotted against the contact area. 70

4.10. **a)** SEM micrographs of a ripped off Au bonding wire on evaporated In. **b)** Closeup of the bonding area. 71

4.11. SEM image of a cross-section through an evaporated ohmic contact at the mesa edge prepared by standard FIB techniques. Insets show magnified pictures of the metal/CdTe interface (left) and the metal/HgCdTe interface (right). While the layer structure of the evaporated metal (AuGe/Ti/Au) is still visible on CdTe, strong clustering can be observed for the HgCdTe interface. 72

4.12. Resistance measurement for different AuGe contacts on Q2151. 73

4.13. **a)** Current pattern for a horizontal diffusion layer as adapted from Ref. [98]. For higher sheet resistance the current will be forced to the leading edge x of the contact area. **b)** Equivalent picture for HgTe/HgCdTe heterostructures. Metal diffusion is not uniform over the whole contact area, leading to variations in the sheet resistance. 74

4.14. Resistance of AuGe ohmics on Q2320 for different cap layer thicknesses. A decrease of resistance for thinner cap layers can be observed. 76

4.15. DC I-V curves for different metals on cleaned HgTe/HgCdTe with a barrier thickness of 105 nm measured at $T = 4$ K. Linear behavior is observed within the common excitation voltage range. 76

4.16. Comparison of old mask layout for contacting e-beam structures (left) to the new design with extended bondpads (right). The number of ohmics is increased from 6 to 12 and the number of gates from 2 to 6. The scale bar applies to both designs. Further miniaturization is still possible. . . 77

4.17. Colored SEM micrograph of two sidewall examples after evaporation of 100 nm Au onto a positive photoresist and lift-off in acetone. The structure height resembles the initial photoresist thickness. 79

4.18. SEM micrographs of resist structures of nominal identical shape obtained from a positive and negative lithography process, respectively. a) Positive resist profile AZ ECI 3012 b) Negative resist profile AR-N 4340. 80

4.19. a) SEM micrograph of 200 nm Au evaporated on a 1.3 μm thick layer of AR-N-4340. Because of the strong undercut the formation of sidewalls is inhibited b) 200 nm Au on HgCdTe after lift-off. No metal sidewalls can be observed. 81

4.20. SEM pictures of a cleaved HgTe/CdTe wafer covered with an etch shield patterned in photoresist (Shipley Microposit S1813) before (left) and after Ar^+ ion milling (right). The resist walls have an angle of roughly 80°, the resist thickness is approximately 1 μm. Dotted green lines are a guide to the eye for the interface between the HgTe layer and the underlying CdTe substrate. A slight color difference is visible. 83

4.21. Two-dimensional AFM scan of a dry-etched stripe array after the removal of the resist etch mask. The profile linescan (red) clearly shows fences at the mesa edges of approximately 25 nm compared to a total etch depth of 100 nm. 84

4.22. SEM micrographs of Ti remains on a HgCdTe substrate after treatment with HF. a) Still visible pattern after HF treatment b) Closeup of a Hall bar lead c) Transition between Ti exposed area (above) and not exposed part (below) d) Side view of the same area, clearly showing the surface roughness in the former Ti area. Oval structures show growth defects within the MBE layer structure. 87

4.23. Illustration of the metal-dielectric interface. Two energy barriers prevent the thermal diffusion of Ti into the dielectric, E_m is the energy necessary to leave the metal matrix, E_i is the energetic barrier resulting from the interface oxide. Adapted from Ref. [136]. 88

4.24. Schematic concept of the etch shield and mesa fabrication including a SiO_2 sacrificial layer. After deposition of the oxide on the clean substrate, the Ti shield can be structured with standard e-beam or optical lithography. The unnecessary oxide is removed in an isotropic dry etching step, using a combined CHF_3 and O_2 plasma. The mesa is defined using Ar^+ IBE. In a final step the sacrificial layer is dissolved in BOE, lifting the Ti layer. 89

4.25. a) Ti etch shield with underlying SiO_2 sacrificial layer after IBE, without RIE removal of the uncovered SiO_2 b) IBE result with previous RIE step, leading to an obvious improvement. No fencing is observed. c) Array of 16 teststructures, after IBE and subsequent etch shield removal in BOE d) Closeup of one structure revealing the stability of the Ti/TiO2 shield. Only the sacrificial layer was completely dissolved. 90

4.26. Schematic concept of a negative lithography process utilizing an Al_2O_3 etch shield grown by ALD. The layer can be patterned using e.g. PMMA as a protective layer. The unnecessary oxide is removed in an isotropic wet etching step, using a solution of TMAH. The mesa is defined using Ar^+ IBE. In a final step the hardmask is dissolved in TMAH or BOE. . 92

4.27. Two-dimensional AFM scan of a dry-etched stripe array after the removal of a 10 nm ALD hardmask. The profile linescan (red) shows no fences at the mesa edges. The surface roughness originates from growth defects in the test material and is not connected to the lithography. . . 93

4.28. **a)** After growth of the Al_2O_3 sacrificial layer, the Ti mask can be patterned using standard optical or e-beam lithography and e-beam evaporation. **b)** The final hardmask is defined in a 40 s dip in a solution of TMAH (Developer CD26). **c)** The Mesa is defined in an Ar^+ ion milling step. **d)** An additional wet etch step is introduced. **e)** The mask is removed in BOE. **f)** SEM micrograph of a final mesa without fences showing smooth sample walls. The scale bar is 1 µm. [140] 95

4.29. SEM micrographs of a 80 nm line pattern on a CdTe/HgCdTe wafer, structured using standard 2.5 kV e-beam lithography and a 15 nm hardmask. a) Pure Ar^+ ion milling. b) Two-step etching process combining Ar^+ ion milling and a bromine ethylene-glycol wet-etch similar to [140], before the hardmask removal. For the wet etch step the initial mask has to be larger than the final structure to achieve the same CD. 96

4.30. Energy distribution by position for a 2.5 kV electron beam and 120 nm PMMA (left) and for a 30 kV beam and 200 nm PMMA (right). Note the difference in spatial extent by an order of magnitude. The simulation was performed using the software CASINO [152]. 97

4.31. a) SEM micrograph of an evaporated 15 nm thick Ti line, structured on a FEI Nova NanoSEM 450 at 2.5 kV, 30 μC/cm^2 in 120 nm 950k PMMA. b) SEM micrograph of an ion milled 300 nm hole, separated from the mesa edge by a 30 nm strip, structured on a Zeiss Leo1525 at 2.5 kV, 50 μC/cm^2 in 120 nm 950k PMMA. 99

4.32. Schematic of the different e-beam exposure layers for a micro Hall bar with airbridge gate. 101

4.33. Measured depth into PMMA as a function of electron energy and different exposure doses. From Borzenko *et al.* [162]. 103

4.34. Colored SEM micrographs of an actual bridge over a micro Hall bar. Yellow areas mark gate leads, conducting posts and span, blue shaded areas depict parts of the underlying mesa. The distance between the mesa and the span is clearly visible. 104

4.35. Hall resistance R_{xy} of a micro Hall bar at T = 4 K and for different airbridge voltages, as a function of magnetic field B. 105

4.36. Four terminal resistance R_{xx} as a function of gate voltage in the range from −0.5 V to 2.2 V. After the initial measurement (blue) from 0 V to 2.2 V the curves stabilize at two different paths for up (black) and down (red). 106

4.37. Four terminal resistance R_{xx} as a function of gate voltage. The measurement is divided into three separate measurements. blue: 2.2 V to 0 V in 1 mV steps, black: 0 V to −2 V in 5 mV steps, red: −2 V to 2.2 V in 5 mV steps. Arrows indicate the measurement direction. . . . 107

4.38. Two sequential measurements of the four terminal resistance R_{xx} as a function of gate voltage on a second device on a different wafer Q2389. 108

4.39. Charging of the gate from 0.0 V to 0.1 V as a function of time with an applied source voltage U_0 of 0.1 V and for different resistances. 109

5.1. Energy, E, of the lowest s-like, E1, and p-like, H1, subbands versus wave number k for a 5 nm (normal) and a 7 nm (inverted) HgTe quantum well. The thick lines are obtained from $\mathbf{k} \cdot \mathbf{p}$ calculations, while the thin (dashed) lines are results of the Bernevig-Hughes-Zhang (BHZ) model, Eqs. (5.1) and (5.2). 113

5.2. Micrograph of the sample mesa with 40 parallel 50 µm long wires with a width of approximately 0.37 µm. 114
5.3. Magnetoresistance (d = 7 nm), $R_{xx}(B)$, of (a) a macroscopic Hall bar with (30×10) µm^2 and (b) 40 parallel wires with (50×0.37) µm^2 area for different gate voltages V_G. For clarity, the traces of Fig. 5.3 a) are displayed with an constant offset of 1 kΩ. The corresponding measured carrier densities are $n = 3.2$, 4.3, 5.4, 6.7, and 7.9×10^{11} cm^{-2} for the indicated gate voltage. For the multiple wire sample of Fig. 5.3 b), the carrier densities are indicated in the figure. 115
5.4. Magnetoresistance (d = 5 nm), $R_{xx}(B)$, of (a) a macroscopic Hall bar with 600×200 µm^2 and (b) 40 parallel wires with 50×0.37 µm^2 area for different gate voltages V_G. For clarity, the traces of Fig. 5.4 a) are displayed with offsets of 5 kΩ. The corresponding measured carrier densities are $n = 1.4$, 1.9, 2.5, 3.1, and 3.7×10^{11} cm^{-2} for $V_G =$ 0.2, 0.4, 0.6, 0.8 and 1.0 V. For the multiple wire sample, Fig. 5.4 b) the carrier densities inferred from comparable Hall bars are indicated in the figure. 116
5.5. WAL contribution to the magnetoconductivity, $\delta\sigma_{xx}(B)$, for wires of the 7 nm (inverted) QW at different gate voltages V_g. The thin (red) lines are fits based on Eqs. (5.4) - (5.6). Subsequent curves are shifted by e^2/h for clarity. 117
5.6. WAL contribution to the magnetoconductivity, $\delta\sigma_{xx}(B)$, for wires of 5 nm (normal) QW at different gate voltages V_g. The thin (red) lines are fits based on Eqs. (5.4) - (5.6). Subsequent curves are shifted by $0.1e^2/h$ for clarity. 118
5.7. (a) Temperature dependence of the conductivity $\delta\sigma_{xx}(T)$ for wires of the 7 nm (inverted) QW and 5 nm (normal) QW (inset) at different gate voltages. The solid lines are fits based on Eqs. (5.4) - (5.6). (b) Extracted dephasing length for wires of the inverted and normal QW at $V_g = 0$. Inset: Extracted Berry phase, β_M, versus carrier density n_s for inverted and normal samples. 119
5.8. Conductance as a function of magnetic field showing universal conductance fluctuations, measured at $T = 1.8$ K on a single wire structured from material with a normal QW. 123

5.9. Conductance as a function of magnetic field showing universal conductance fluctuations, measured at $T = 1.8$ K on a single wire structured from material with an inverted QW. 123

List of Tables

4.1. Tested metals and corresponding melting temperatures. 66

5.1. Thickness d and band structure parameters $\mathcal{M}$, $\mathcal{A}$, $\mathcal{B}$ and $\mathcal{D}$ for the inverted and non-inverted HgTe QWs used in our experiment. 113

5.2. Gate-voltage V_g dependent carrier density n , Fermi energy E_{F} and fitting parameters c_1 and c_2 for the 7 nm (inverted) QW. The experimentally encountered mobilities varies between 30000 and 60000 cm^2/Vs for the normal and inverted samples. 120

5.3. Gate-voltage V_g dependent carrier density n , Fermi energy E_{F} and fitting parameters c_1 and c_2 for the 5 nm (normal) QW. 120

A.1. List of substrates with their detailed layer sequence and thicknesses d from top (left) to bottom (right). Doping is indicated with y (yes) or n (no). 129

Bibliography

[1] "The Transistor". Nobelprize.org. Nobel Media AB 2014. Web. 22 May 2015. http://www.nobelprize.org/educational/physics/transistor/function/first-transistor.html

[2] I. M. Ross, *Proceedings of the IEEE* **86**, No. 1, (1998).

[3] M. Riordan, *The Lost History of the Transistor*, IEEE Spectrum, (2004).

[4] http://newsroom.intel.com/docs/DOC-5073, Web. 23 May 2015.

[5] L. R. Harriott, *Materials Today* **Vol. 2**, Issue 2 ,(1999).

[6] R. Ghodssi and P. Lin, *MEMS Materials and Processes Handbook*, Springer Science + Business Media, LLC (2011).

[7] S. Datta and B. Das, *Appl. Phys. Lett.* **56**, 665, (1990).

[8] J. Hinz, H. Buhmann, M. Schäfer, V. Hock, C. R. Becker and L. W. Molenkamp, *Semicond. Sci. Technol.* **21**, 501, (2006).

[9] M. Z. Hasan and C. L. Kane, *Rev. Mod. Phys.* **82**, 3045, (2010).

[10] L. Fu and C. L. Kane, *Phys. Rev. Lett.* **100**, 096407, (2008).

[11] C. Nayak, S. H. Simon, A. Stern, M. Freedman, S. Das Sarma, *Rev. Mod. Phys.* **80**, 1083, (2008).

[12] C. L. Kane and E. J. Mele, *Phys. Rev. Lett.* **95**, 226801, (2005).

[13] B. A. Bernevig, T. L. Hughes, S-C. Zhang, *Science* **314**, 1757, (2006).

[14] M. König, S. Wiedmann, C. Brüne, A. Roth, H. Buhmann, L. W. Molenkamp, X-L. Qi, S. C. Zhang, *Science* **318**, 766, (2007).

[15] J. E. Moore and L. Balents, *Phys. Rev. B* **75**, 121306(R) (2007)

[16] D. J. Thouless, M. Kohmoto, M. P. Nightingale, and M. den Nijs, *Phys. Rev. Lett.* **49**, 405, (1982).

[17] C. L. Kane and E. J. Mele, *Phys. Rev. Lett.* **95**, 146802, (2005).

[18] S. Murakami, *New Journal of Physics* **13**, 105007, (2011).

[19] C. Brüne, C.X. Liu, E. G. Novik, E. M. Hankiewicz, H. Buhmann, Y. L. Chen, X. L. Qi, Z. X. Shen, S. C. Zhang and L. W. Molenkamp, *Phys.Rev. Lett.* **106**, 126803, (2011).

[20] L. Fu and C. L. Kane, *Phys. Rev. B* **76**, 045302 (2007).

[21] M. Cardona, N. E. Christensen und G. Fasol, *Phys. Rev. B* **38**, 1806, (1988).

[22] A. Pfeuffer-Jeschke, *Bandstruktur und Laudau-Niveaus quecksilberhaltiger II-VI-Heterostrukturen*, Dissertation, (2000).

[23] E. O. Kane, *J. Phys. C: Solid State Phys.* **1**, 249, (1957).

[24] J. Chu and A. Sher, *Physics and Properties of Narrow Gap Semiconductors*, Springer-Verlag New York, (2008).

[25] M. H. Weiler, *Semiconductors and Semimetals* **Vol. 16**, 119, (1981).

[26] J. P. Laurenti,J. Camassel, A.Bouhemadou, B. Toulouse, R. Legros and A. Lusson, *J. Appl. Phys.* **67**, 6454, (1990).

[27] B. Büttner, C. X. Liu, G. Tkachov, E. G. Novik, C. Brüne, H. Buhmann, E. M. Hankiewicz, P. Recher, B. Trauzettel, S. C. Zhang and L. W. Molenkamp, *Nature Physics* **7**, 418, (2011).

[28] M. Büttiker, *Phys. Rev. B* **38**, 9375, (1988).

[29] C. Wu, B. A. Bernevig and S-C. Zhang, *Phys. Rev. Lett.* **96**, 106401, (2006).

[30] C. Xu and J. E. Moore, *Phys. Rev. B* **73**, 045322, (2006).

[31] A. Roth, C. Brüne, H. Buhmann, L. W. Molenkamp, J. Maciejko, X-L. Qi, S-C. Zhang, *Science* **325**, 294, (2009).

[32] M. Büttiker, *Phys. Rev. Lett.* **57**, 1761, (1986).

[33] M. Büttiker, *Science* **325**, 278, (2009).

[34] E. M. Hankiewicz, L. W. Molenkamp, T. Jungwirth, and J. Sinova, *Phys. Rev. B* **70**, 241301(R), (2004).

[35] C. Bruene, A . Roth, E. G. Novik, M. König, H. Buhmann, E. M. Hankiewicz, W. Hanke, J. Sinova and L. W. Molenkamp, *Nature Physics* **6**, 488, (2010).

[36] K. C. Nowack, E. M. Spanton, M. Baenninger, M. König, J. R. Kirtley, B. Kalisky, C. Ames, P. Leubner, C. Brüne, H. Buhmann, L. W. Molenkamp, D. Goldhaber-Gordon and K. A. Moler, *arXiv* **1212.2203v2**, (2012).

[37] M. Baenninger, M. König, A. G. F. Garcia, M. Mühlbauer, C. Ames, P. Leubner, C. Brüne, H. Buhmann, L. W. Molenkamp, and D. Goldhaber-Gordon, *J. Appl. Phys.* **112**, 103713, (2012).

[38] M. König, M. Baenninger, A. G. F. Garcia, N. Harjee, B. L. Pruitt, C. Ames, P. Leubner, C. Brüne, H. Buhmann, L. W. Molenkamp, D. Goldhaber-Gordon, *Phys. Rev. X* **3**, 021003, (2013).

[39] H. van Houten and C. W. J. Beenakker, *Semiconductors and Semimetals* **Vol. 35**, 9, (1992).

[40] J. C. Y. Teo and C. L. Kane, *Phys. Rev. B* 79, 235321, (2009).

[41] C-Y. Hou, E-A. Kim, and C. Chamon, *Phys. Rev. Lett.* **102**, 076602, (2009).

[42] A. Ström and H. Johannesson, *Phys. Rev. Lett.* **102**, 096806, (2009).

[43] P. Virtanen and P. Recher, *Phys. Rev. B* **83**, 115332, (2011).

[44] F. Dolcini, *Phys. Rev. B* **85**, 033306, (2012).

[45] J.-R. Souquet and P. Simon, *Phys. Rev. B* **86**, 161410(R), (2012).

[46] T. L. Schmidt, *Phys. Rev. Lett.* **107**, 096602, (2011).

[47] G. Dolcetto, S. Barbarino, D. Ferraro, N. Magnoli and M. Sassetti, *Phys. Rev. B* **85**, 195138, (2012).

[48] J. M. Edge,J. Li, P. Delplace and M. Büttiker, *arXiv* 1304.2656v1, (2013).

[49] B. A. Bernevig and S. Zhang, *IBM J. Res. Dev.* **50**, 141, (2006).

[50] V. Krueckl and K. Richter, *Phys. Rev. Lett.* **107**, 086803, (2011).

[51] Y. A. Bychkov and E. I. Rashba, *J. Phys. C* **17**, 6039, (1984).

[52] Y. S. Gui, C. R. Becker, N. Dai, J. Liu, Z. J. Qiu, E. G. Novik, M. Schäfer, X. Z. Shu, J. H. Chu, H. Buhmann, and L. W. Molenkamp, *Phys. Rev. B* **70**, 115328, (2004).

[53] E. G. Novik, A. Pfeuffer-Jeschke, T. Jungwirth, V. Latussek, C. R. Becker, G. Landwehr, H. Buhmann and L. W. Molenkamp, *Phys. Rev. B* **72**, 035321, (2005).

[54] F. Dolcini, *Phys. Rev. B* **83**, 165304, (2011).

[55] L. B. Zhang, F. Cheng, F. Zhai, and Kai Chang, *Phys. Rev. B* **83**, 081402(R), (2011).

[56] Y. Li, M. B. A. Jalil, S. G. Tan, and G. Zhou, *J. Appl. Phys.* **112**, 063710, (2012).

[57] B. Zhou, H-Z. Lu, R-L. Chu, S-Q. Shen and Q. Niu, *Phys. Rev. Lett.* **101**, 246807 (2008).

[58] J-J. Zhu, D-X. Yao, S-C. Zhang, K. Chang, *Phys. Rev. Lett.* **106**, 097201, (2011).

[59] D-X. Qu, Y. S. Hor, J. Xiong,R. J. Cava and N. P. Ong, *Science* **329**, 821, (2010).

[60] N. P. Butch, K. Kirshenbaum, P. Syers, A. B. Sushkov, G. S. Jenkins, H. D. Drew, and J. Paglione, *Phys. Rev B* **81**, 241301(R), (2010).

[61] C. Shekhar, S. Ouardi, A. K. Nayak, G. H. Fecher, W. Schnelle and C. Felser, *Phys. Rev. B* **86**, 155314, (2012).

[62] G. Tkachov, C. Thienel, V. Pinneker, B. Büttner, C. Brüne, H. Buhmann, L.W. Molenkamp, and E. M. Hankiewicz, *Phys. Rev. Lett.* **106**, 076802, (2011).

[63] B. J. van Wees, H. van Houten, C. W. J. Beenakker, J. G. Williamson, L. P. Kouwenhoven, D. van der Marel and C. T. Foxon, *Phys. Rev. Lett.* **60**, 848, (1988).

[64] D. A. Wharam, T. J. Thornton, R. Newbury, M. Pepper, H. Ahmed, J. E. F. Frost, D. G. Hasko, D. C. Peacock, D. A. Ritchie and G. A. C. Jones, *J. Phys. C: Solid State Phys.* **21**, L209, (1988).

[65] T. J. Thornton, M. Pepper, H. Ahmed, D. Andrews and G. J. Davies, *Phys. Rev. Lett* **56**, 1198, (1986).

[66] M. Büttiker, *Phys. Rev. B* **41**, 7906, (1990).

[67] R. Landauer, *Zeitschrift für Physik B Condensed Matter* **Vol. 68**, Issue 2-3, 217, (1987).

[68] L. I. Glazman, G. B. Lesovik, D. E. Khmel'nitskii and R. I. Shekhter, *JETP Lett.* **48**, No.4, (1988).

[69] L. I. Glazman and A. V. Khaetskii, *JETP Lett.* **48**, No.10, (1988).

[70] L. I. Glazman and M. Jonson, *Phys. Rev. Lett.* **64**, 1186, (1990).

[71] D. S. Fisher and P. A. Lee, *Phys. Rev. B* **23**, 6851, (1981).

[72] A. Yacoby and Y. Imry, *Phys. Rev. B* **41**, 5341, (1990).

[73] C. W. J. Beenakker and H. van Houten, *Solid State Physics* **44**, 1, (1991).

[74] S. Datta, *Electronic Transport in Mesoscopic Systems*, Cambridge University Press, (1995).

[75] A. Szafer and A. D. Stone, *Phys. Rev. Lett.* **62**, 300, (1989).

[76] G. Timp, R. E. Behringer, S. Sampere, J. E. Cunningham, and R. Howard, *Proc. Int. Symp. on Nanostructure Physics and Fabrication* (W. P. Kirk and M. Reed, eds.), p. 331, (1989).

[77] C. W. J. Beenakker and H. van Houten, *Phys. Rev. B* **39**, 10445, (1989).

[78] M. A. Reed and W. P. Kirk, *Nanostructure Physics and Fabrication*, (1989).

[79] G. Timp, *Semiconductors and Semimetals* **Vol. 35**, 113, (1992).

[80] H. U. Baranger and A. D. Stone, *Phys. Rev. Lett.* **63**, 414, (1989).

[81] L. W. Molenkamp, A. A. M. Staring, C. W. J. Beenakker, R. Eppenga, C. E. Timmering, J. G. Williamson, C. J. P. M. Harmans and C. T. Foxon, *Phys. Rev. B* **41**, 1274, (1990).

[82] D. A. Wharam, M. Pepper, H. Ahmed, J. E. F. Frost, D. G. Hasko, D. C. Peacock, D. A. Ritchie, and G. A. C. Jones, *J. Phys. C* **21**, L887, (1988).

[83] J. A. Nixon, J. H. Davies and H. U. Baranger, *Phys. Rev. B* **43**, 12638, (1991).

[84] M. A. Topinka, B. J. LeRoy, S. E. J. Shaw, E. J. Heller, R. M. Westervelt, K. D. Maranowski, and A. C. Gossard, *Science* **289**, (2000).

[85] M. Koenig, M. Baenninger, A. G. F. Garcia, N. Harjee, B. L. Pruitt, C. Ames, P. Leubner, C. Bruene, H. Buhmann, L. W. Molenkamp and D. Goldhaber-Gordon, *Phys. Rev. X* **3**, 021003 (2013).

[86] G. Timp, H. U. Baranger, P. deVegvar, J. E. Cunningham, R. E. Howard, R. Behringer, and P. M. Mankiewich, *Phys. Rev. Lett* **60**, 2081, (1988).

[87] V. Daumer, I. Golombek, M. Gbordzoe, E. G. Novik, V. Hock, C. R. Becker,H. Buhmann and L. W. Molenkamp, *Apl. Phys. Lett.* **83**, 1376, (2003).

[88] A. S. D. Heindrichs, H. Buhmann, S. F. Godijin, L. W. Molenkamp, *Phys. Rev. B* **57**, 3961, (1998).

[89] M. Khodas, A. Shekhter, A. M. Finkel‘stein, *Phys. Rev. Lett.* **92**, 086602, (2004).

[90] G. Dresselhaus, *Phys. Rev.* **100**, 580, (1955).

[91] J. Luo, H. Munekata, F. F. Fang, and P. J. Stiles, *Phys. Rev. B* **41** ,7685, (1990).

[92] G. Lommer, F. Malcher, and U. Rossler, *Phys. Rev. Lett.* **60**, 728, (1988).

[93] S. A. Wolf, D. D. Awschalom, R. A. Buhrman, J. M. Daughton, S. von Molnar, M. L. Roukes, A. Y. Chtchelkanova and D. M. Treger, *Science* **294**, 1488, (2001).

[94] D. Dragoman and M. Dragoman, *Quantum Classical Analogies*, Springer-Verlag Berlin Heidelberg, (2004).

[95] U. Sivan, M. Heiblum, C. P. Umbach and H. Shtrikman, *Phys. Rev. B* **41**, 7937, (1990).

[96] J. Spector, H. L. Stormer, K. W. Baldwin, L. N. Pfeiffer and K. W. West, *Appl. Phys. Lett.* **56**, 2433, (1990).

[97] D. G. Rothe and E. M. Hankiewicz, *Phys. Rev B* **89**, 035418, (2014).

[98] S. M. Sze, K. K. Ng, *Physics of Semiconductor Devices*, 3rd Edition, (2007).

[99] V. L. Rideout, *Solid-State Electronics* **Vol. 18**, 541, (1975).

[100] P. W. Leech, *J. Appl. Phys.* **68**, 907, (1990).

[101] C. K. Saw , W. J. Siekhaus, *Scripta Materialia* **53**, 1153, (2005).

[102] H. W. Leidecker, M. J. Sampson, *GSFC NASA ADVISORY* **NA-GSFC-2004-01**, (2003).

[103] J. E. Jellison, *Gold-Indium Intermetallic Compounds: Properties and Growth Rates*, Materials Control and Applications Branch, (1979).

[104] E. Janik, R. Triboulet, *J. Phys. D: Appl. Phys.* **16**, 2333, (1983).

[105] C. R. Becker, C. Brüne, M. Schäfer, A. Roth, H. Buhmann, and L. W. Molenkamp, *Phys. Stat. Sol. (c)* **4**, No. 9, 3382, (2007).

[106] H. Okamoto and T. B. Massalski, *Bulletin of Alloy Phase Diagrams* **Vol. 5**, No. 6, 601, (1984).

[107] S. K. Ghandhi, N. R. Taskar, K. K. Parat and I. B. Bhat, *Appl. Phys. Lett.* **57**, 252, (1990).

[108] A. L. Fahrenbruch, *Solar Cells* **21**, 399, (1987).

[109] R. E. Braithwaite, C. G. Scott and J. B. Mullin, *Solid-State Electron.* **23**, 1091, (1980).

[110] R. Hill and F. Williams, *Appl. Phys. Lett.* **11**, 296, (1967).

[111] R. Hill, D. Richardson and S. Wilson, *J. Phys. D: Appl. Phys.* **5**, 185, (1972).

[112] R. J. Westerhout, R. H. Sewell, J. M. Dell, L. Faraone and C. A. Musca, *Structure and Electrical Characteristics of Metal/MCT Interfaces*, in *Mercury Cadmium Telluride* (eds P. Capper and J. Garland), John Wiley and Sons, Ltd, Chichester, UK (2010).

[113] A. Onshage, *Mercury Cadmium Telluride Imagers: A Patent-oriented survey*, **Vol. 5**, (1997).

[114] E. J. Koop, M. J. Iqbal, F. Limbach, M. Boute, B. J. van Wees, D. Reuter, A. D. Wieck, B. J. Kooi and C. H. van der Wal, *Semicond. Sci. Technol.* **28**, 025006, (2013).

[115] H. Murrmann and D. Widmann, *IEEE Trans. Electron. Dev.* ED-16, 1022, (1969).

[116] W. A. Beck, G. D. Davis, and A. C. Goldberg, *J. Appl. Phys.* **67**, 6340, (1990).

[117] C. Mack, *Fundamental Principles of Optical Lithography: The Science of Microfabrication*, John Wiley & Sons Ltd., (2007).

[118] B. W. Smith, K. Suzuki, *CRC Press*, *Microlithography: Science and Technology*, Second Edition, (2007).

[119] S. Van Nguyen, D. Dobuzinski, S.R. Stiffler, G. Chrisman, *J. Electrochem. Soc.* **138**, 1112, (1991).

[120] M. J. Madou, *Fundamentals of Microfabrication: The Science of Miniaturization*, Second Edition, CRC Press LLC., (2002).

[121] K. Babich, A. P. Mahorowala, D. R. Medeiros, D. Pfeiffer, K. E. Petrillo, M. Angelopoulos, A. Grill, V. Patel, S. Halle, T. A. Brunner, R. Conti, S. D. Allen and R. Wise, *Proceedings of the SPIE* **5039**, 152, (2003).

[122] K. L. Doan, J. M. Kim, D. Shimizu, *Boron-doped carbon-based hardmask etch processing*, US Patent US20140213059 A1, (2014).

[123] M. König, *Spin-related transport phenomena in HgTe-based quantum well structures*, Dissertation, (2007).

[124] V. Srivastav, R. Pal, B. L. Sharma, V. Mittal, V. Gopal and H. P. Vyas, *Journal of Electronic Materials* **Vol. 34**, Issue 3, 225, (2005).

[125] G. Bahir, R. Adar and R. Fastow, *J. Vac. Sci. Technol. B* **9**, 266, (1991).

[126] C. Bory, J-L. O. Buffet and G. Parat, *Process for the production of an electric contact on a HgCdTe substrate with a p-conductivity and application to the production of an n/p diode*, US Patent No. 4766084, (1988).

[127] E. Brydges, R. Prideaux and J. O. Millott, *J. Chem. Soc.* **0**, 2703, (1929).

[128] H. Appelman, J. Levy, M. Pion, D. Krebs, C. Harding and M. Zediker, *Journal of Lightwave Technology* **8 (1)**, 39, (1990).

[129] O. Powell, D. Sweatman and H.B. Harrison, *Smart Mater. Struct.* **15**, s81, (2006).

[130] Yu. A. Buslaev, V. A. Bochkareva, and N. S. Nikolaev, *Izvestiya Akademii Nauk SSSR, Otdelenie Khimicheskikh Nauk* **3**, 388, (1962).

[131] J. P. Rioult and R. Fabien, *Method for selective etching of titaniumdioxide relative to aluminum*, *US Patent No. 4322264*, (1988).

[132] J. D. Lin, Y. K. Su, S. J. Chang, M. Yokoyama, and F. Y. Juang, *J. Vac. Sci. Technol. A* **12**, 7, (1994).

[133] E. H. P. Cordfunke, W. Ouweltjes, G. Prins, *The Journal of Chemical Thermodynamics* **19**(4), 369, (1987).

[134] J. A. Wilson and V. A. Cotton, *J. Appl. Phys.* **57**, 2030, (1985).

[135] B. K. Janousek, R. C. Carscallen and P. A. Bertrand, *J. Vac. Sci. Technol. A* **1**, 1723, (1983).

[136] M. He and T-M. Lu, *Metal-Dielectric Interfaces in Gigascale Electronics*, Springer-Verlag New York, (2012).

[137] S. M. George, *Chem. Rev.* **110**, 111, (2010).

[138] Y. Xuan, Y. Q. Wu, T. Shen, M. Qi, M. A. Capano, J. A. Cooper, P. D. Ye, *Appl. Phys. Lett.* **92**, 013101, (2008).

[139] J. Oh, J. Myoung, J. S. Bae, and S. Lim, *J. Electrochem. Soc.* **158**(4), D217, (2011).

[140] E. Yue Ma, M. R. Calvo, J. Wang, B. Lian, M. Mühlbauer, C. Brüne, Y. Cui, K. Lai, W. Kundhikanjana, Y. Yang, M. Baenninger, M. König, C. Ames, H. Buhmann, P. Leubner, L. W. Molenkamp, S-C Zhang, D. Goldhaber-Gordon, M. K. Kelly and Z-X Shen, *Nature Communications* **6**, 7252, (2015).

[141] O. Gelhausen H. N. Klein, M. R. Phillips, E. M. Goldys, *Physica Status Solidi (b)* **239(2)**, 310, (2003).

[142] J. Kempf, M. Nonnenmacher, H. H. Wagner, *Appl. Phys. A* **56**, 385, (1993).

[143] S. J. Randolph, J. D. Fowlkes and P. D. Rack, *J. Appl. Phys.* **97**, 124312, (2005).

[144] R. F. Egerton, P. Li and M. Malac, *Micron* **35**, 399, (2004).

[145] T. Fink, D. D. Smith, W. D. Braddock, *IEEE Transactions Electron Devices* **37**, 1422, (1990).

[146] N. Tanaka, H. Kawanishi, T. Ishikawa, *Jpn. J. Appl. Phys.* **32**, 540, (1993).

[147] N. Tanaka, T. Ishikawa, *Journal of Electronic Materials* **23**, 341, (1994).

[148] R. Castaing, *University of Paris Application des sondes électroniques à une méthode d'analyse ponctuelle chimique et cristallographique*, PhD Thesis, (1951).

[149] S. B. J. Reed, *Electron Microprobe Analysis and Scanning Electron Microscopy in Geology*, Second Edition, *Cambridge University Press* (2005).

[150] P. Capper, *Properties of Narrow Gap Cadmiumbased Compounds*, Emis Data Reviews Series **Vol. 10**, (1994).

[151] D. Chu, W-K. Wong, K. E. Goodson, R. Fabian, W. Pease, *J. Vac. Sci. Technol. B* **21(6)**, 2985, (2003).

[152] D. Drouin, A. R. Couture, D. Joly, X. Tastet, V. Aimez, R. Gauvin, *Scanning* **29**, 92, (2007).

[153] B. Houli, V. Umansky and M. Heiblum, *Semicond. Sci. Technol.* **8**, 1490, 29, (1993).

[154] M. Mühlbauer, A. Budewitz, B. Büttner, G. Tkachov, E. M. Hankiewicz, C. Brüne, H. Buhmann and L. W. Molenkamp, *Phys. Rev. Lett.* **112**, 146803, (2014).

[155] L. Maier, J. B. Oostinga, D. Knott, C. Bruene, P. Virtanen, G. Tkachov, E. M. Hankiewicz, C. Gould, H. Buhmann, L. W. Molenkamp, *Phys. Rev. Lett.* **109**, 186806, (2012).

[156] M. E. Sherwin, J. A. Simmons, T. E. Eiles, N. E. Harff, and J. F. Klem, *Appl. Phys. Lett.* **65** (18), 2326, (1994).

[157] R. V. Gorbachev, A. S. Mayorov, A. K. Savchenko, D. W. Horsell, and F. Guinea, *Nano Lett.* **8 (7)**, 1995, (2008).

[158] M. A . Gritz, M. Metzler, J. Moser, D. Spencer and G. D. Boreman, *J. Vac. Sci. Technol. B* **21(1)**, 332, (2003).

[159] E. Girgis, J. Liu and M. L. Benkhedar, *Appl. Phys. Lett.* **88**, 202103, (2006).

[160] A. Khalid, C. Li, J. Grant, S. Saha, S. Ferguson, D. R. S. Cumming, *Microelectron. Eng.* **98**, 262, (2012).

[161] T. Borzenko, F. Lehmann, G. Schmidt and L. W. Molenkamp, *Microelectron. Eng.* **67-68**, 720, (2003).

[162] T. Borzenko, C. Gould, G. Schmidt and L. W. Molenkamp, *Microelectron. Eng.* **75(2)**, 210, (2004).

[163] C. J. Grebenkemper and J. P. Hagen, *Phys. Rev.* **80**, 89, (1950).

[164] A. I. Kingon, J.-P. Maria and S. K. Streiffer, *Nature* **406**, 1032, (2000).

[165] N. Szydlo and R. Poirier, *J. Appl. Phys.* **51**, 3310, (1980).

[166] M. Wolfke and W. H. Keesom, *Proceedings Royal Acad. Amsterdam*, **Vol. XXXI**, 6, (1927).

[167] A. Rogalski, *Rep. Prog. Phys.*, **68**, 2267, (2005).

[168] G. M. Rebeiz, John Wiley & Sons, Inc., *RF MEMS: Theory, Design, and Technology*, (2003).

[169] S. Majumder, N. E. McGruer, G. G. Adams, P. M. Zavracky, R. H. Morrison, J. Krim, *Sensors and Actuators A*, **93**, 19, (2001).

[170] G. Bergmann, *Sol. State Commun.* **42**, 815, (1982).

[171] P. D. Dresselhaus, C. M. A. Papavassiliou, R. G. Wheeler, and R. N. Sacks, *Phys. Rev. Lett.* **68**, 106, (1992).

[172] H. Suzuura and T. Ando, *Phys. Rev. Lett.* **89**, 266603, (2002).

[173] K. S. Novoselov, A. K. Geim, S. V. Morozov, D. Jiang, M. I. Katsnelson, I. V. Grigorieva, S. V. Dubonos, and A. A. Firsov, *Nature* **438**, 197 (2005); Y. Zhang, J. W. Tan, H. L. Stormer and P. Kim, Nature **438**, 201, (2005).

[174] S. V. Morozov, K. S. Novoselov, M. I. Katsnelson, F. Schedin, L. A. Ponomarenko, D. Jiang, and A. K. Geim, *Phys. Rev. Lett.* **97**, 016801, (2006).

[175] F. V. Tikhonenko, A. A. Kozikov, A. K. Savchenko, R. V. Gorbachev, *Phys. Rev. Lett.* **103**, 226801, (2009).

[176] E. McCann, K. Kechedzhi, V. I. Fal'ko, H. Suzuura, T. Ando, and B. L. Altshuler, *Phys. Rev. Lett.* **97**, 146805, (2006).

[177] S. Minke, J. Bundesmann, D. Weiss, and J. Eroms, *Phys. Rev. B* **86**, 155403, (2012).

[178] F. Ortmann, A. Cresti, G. Montambaux, and S. Roche, *Europhys. Lett.* **94**, 47006, (2011).

[179] G. Tkachov, C. Thienel, V. Pinneker, B. Büttner, C. Brüne, H. Buhmann, L. W. Molenkamp, and E. M. Hankiewicz, *Phys. Rev. Lett.* **106**, 076802, (2011).

[180] J. N. Hancock, J. L. M. van Mechelen, A. B. Kuzmenko, D. van der Marel, C. Brüne, E. G. Novik, G. V. Astakhov, H. Buhmann, and L. W. Molenkamp, *Phys. Rev. Lett.* **107**, 136803, (2011).

[181] A. M. Shuvaev, G. V. Astakhov, G. Tkachov, C. Brüne, H. Buhmann, L. W. Molenkamp, and A. Pimenov, *Phys. Rev. B* **87**, 121104(R), (2013).

[182] E. B. Olshanetsky, Z. D. Kvon, G. M. Gusev, N. N. Mikhailov, S. A. Dvoretsky, and J. C. Portal, *JETP Lett.* **91**, 347, (2010).

[183] G. M. Minkov, A. V. Germanenko, O. E. Rut, A. A. Sherstobitov, S. A. Dvoretski, and N. N. Mikhailov, *Phys. Rev. B* **85**, 235312, (2012).

[184] G. Tkachov and E.M. Hankiewicz, *Phys. Rev. B* **84**, 035444, (2011).

[185] F. Pierre, A. B. Gougam, A. Anthore, H. Pothier, D. Esteve, and N. O. Birge, *Phys. Rev. B* **68**, 085413, (2003).

[186] B. L. Altshuler and A. G. Aronov, Pis'ma Zh. Eksp. Teor. Fiz. **33**, 515 (1981) *JETP Lett.* **33**, 499, (1981).

[187] Th. Schäpers, V. A. Guzenko, M. G. Pala, U. Zülicke, M. Governale, J. Knobbe, and H. Hardtdegen, *Phys. Rev. B* **74**, 081301(R), (2006).

[188] V. Krueckl and K. Richter, *Semicond. Sci. Technol.* **27**, 124006, (2012).

[189] D. G. Rothe, R. W. Reinthaler, C.-X. Liu, L. W. Molenkamp, S.-C. Zhang and E. M. Hankiewicz, *New J. Phys.* **12**, 065012, (2010).

[190] P. M. Ostrovsky, I. V. Gornyi, and A. D. Mirlin, *Phys. Rev. B* **86**, 125323, (2012).

[191] A. E. Hansen, M. T. Björk, C. Fasth, C. Thelander, and L. Samuelson, *Phys. Rev. B* **71**, 205328, (2005).

[192] S. Hikami, A. I. Larkin, and N. Nagaoka, *Prog. Theor. Phys.* **63**, 707, (1980).

[193] V. K. Dugaev and D. E. Khmel'nitskii, Zh. Eksp. Teor. Fiz. **86**, 1784 (1984) *JETP* **59**, 1038, (1984).

Acknowledgments

There are many colleagues and friends that all contributed in their own way to this work.
Particularly I would like to thank:

- **Laurens W. Molenkamp**, for the opportunity to be part of this fascinating research and for the possibility to gain expertise in various fields.
- **Hartmut Buhmann**, for guiding me through my PhD, for his encouragement and giving me the possibility to pursue own ideas and for supporting me in any possible way.
- **Christoph Brüne**, for mentoring me during my time in EP3, our fruitful discussions and his cordial friendship.
- **Luis Maier**, who always shared the fascination and curiosity for the development of new lithography concepts and who was an extraordinary companion not only in the cleanroom but also in private.
- **Kalle Bendias**, for his continuous help and his ambition to realize even most complex samples and the great times we had.
- **Andreas Budewitz**, who was working like a machine to keep the lab running, his tireless effort he put into the WAL paper and for keeping up the good spirits.
- **Bastian Büttner**, for his spadework on WAL in HgTe and sharing his experience.
- **Holger Thierschmann**, for his assistance with QPC related questions and the countless inspiring cafeteria discussions.
- **Cornelius Thienel** for his help with band structure calculations and for playing a vital role in our Cadmium Substrate meetings.

- **Volkmar Hock**, for keeping the cleanroom running, no matter how hard we tried to break stuff.
- **Tanja Borzenko**, for showing me the finer skills of electron beam lithography.
- **Ewelina M. Hankiewicz**, **Gregory Tkachov** and **Dietrich G. Rothe** for their support in all theoretical questions and for developing the model explaining our WAL observations.
- **David Goldhaber-Gordon, Reyes Calvo** and my colleagues at Stanford University for giving me the opportunity for additional process analysis and to further refine the lithography.
- **Pavel. M. Ostrovsky, Igor. V. Gornyi, Alexander. D. Mirlin, and Klaus Richter** for fruitful discussions.
- **Roland Ebert**, for his expertise on cryostats and the never ending supply of liquid Helium.
- My other fellow PhD pursuing colleagues, particularly **Felicitas Gerhard**, **Philipp Leubner** and **Christopher Ames**, my Master and Bachelor students especially **Matthias Däuber**, **Farida Veliev**, **Timo Wagner**, **Thomas Khouri** and **Florian Wallaschkowski** for their outstanding commitment and all members of EP3 for creating this unique environment that made our department such a comfortable place to work. I will miss our Cadmium Substrate meetings. Thank you!

I especially thank my girlfriend **Helene Hoffmann**, for sharing all highs and lows on my way and for supporting and motivating me like no other.

This work was supported by the German Research Foundation DFG (SPP 1285 and 1666, and DFG-JST joint research project ‘Topological Electronics’) and the EU ERC-AG program (Project 3-TOP).